

Copyright  
by  
Shawn Stephen Coffee  
2007

**The Dissertation Committee for Shawn Stephen Coffee Certifies that this is the  
approved version of the following dissertation:**

**Selective Silicon and Germanium Nanoparticle Deposition on  
Amorphous Surfaces**

**Committee:**

---

John G. Ekerdt, Supervisor

---

Brian A. Korgel

---

Gyeong S. Hwang

---

Charles B. Mullins

---

Sanjay K. Banerjee

**Selective Silicon and Germanium Nanoparticle Deposition on  
Amorphous Surfaces**

**by**

**Shawn Stephen Coffee, B.S.; M.S.**

**Dissertation**

Presented to the Faculty of the Graduate School of

The University of Texas at Austin

in Partial Fulfillment

of the Requirements

for the Degree of

**Doctor of Philosophy**

**The University of Texas at Austin**

**August 2007**

## **Dedication**

To my parents, Paul and Ann Coffee

## **Acknowledgements**

Those individuals who deserve acknowledgements are those who helped me through the many rough waters encountered during my five year stay within the Chemical Engineering graduate program. Fellow graduate students who gave counsel and support while obtaining the Ph D degree. I also want to thank staff members, Jim Smitherman, Butch Cunningham, Eddie Ibarra, Kevin Haynes, and Kay Costales-Swift who were always there to help in times of trouble. Finally, for my advisor Dr. Ekerdt who supported me even when the graduate school boat appeared to be sinking.

# **Selective Silicon and Germanium Nanoparticle Deposition on Amorphous Surfaces**

Publication No. \_\_\_\_\_

Shawn Stephen Coffee, Ph.D.

The University of Texas at Austin, 2007

Supervisor: John G. Ekerdt

This dissertation describes the development of a process for the precise positioning of semiconductor nanoparticles grown by hot wire chemical vapor deposition and thermal chemical vapor deposition on amorphous dielectrics, and it presents two studies that demonstrate the process. The studies entailed growth and characterization using surface science techniques and scanning electron microscopy. The two systems, Ge nanoparticles on  $\text{HfO}_2$  and Si nanoparticles on  $\text{Si}_3\text{N}_4$ , are of interest because their electronic properties show potential in flash memory devices. The positioning technique resulted in nanoparticles deposited within 20 nm diameter feature arrays having a  $6 \times 10^{10} \text{ cm}^{-2}$  feature density. Self-assembling diblock copolymer poly(styrene-*b*-methyl methacrylate) thin films served as the patterning soft mask. The diblock copolymer features were transferred using a  $\text{CHF}_3/\text{O}_2$  reactive ion etch chemistry into a thin film  $\text{SiO}_2$  hard mask to expose the desired  $\text{HfO}_2$  or  $\text{Si}_3\text{N}_4$  deposition surface underneath.

Selective deposition upon exposed pore bottoms was performed at conditions where adatom accumulation occurred on the  $\text{HfO}_2$  or  $\text{Si}_3\text{N}_4$  surfaces and not upon the  $\text{SiO}_2$  mask template. The selective deposition temperatures for the  $\text{Ge}/\text{HfO}_2$  and  $\text{Si}/\text{Si}_3\text{N}_4$  systems were 700 to 800 K and 900 to 1025 K, respectively. Germanium nucleation on  $\text{HfO}_2$  is limited from hot wire chemical vapor deposition by depositing nanoparticles within 67% of the available features. Unity filling of features with Ge nanoparticles was achieved using room temperature adatom seeding before deposition. Nanoparticle shape and size are regulated through the Ge interactions with the  $\text{SiO}_2$  feature sidewalls with the adatom removal rate from the features being a function of temperature. The  $\text{SiO}_2$  mask limited Ge nanoparticle growth laterally to within  $\sim 5$  nm of the hard mask at 800 K. Silicon deposition on patterned  $\text{Si}_3\text{N}_4$  has multiple nanoparticles, up to four, within individual 20 nm features resulting from the highly reactive  $\text{Si}_3\text{N}_4$  deposition surface. Silicon nucleation and continued nanoparticle growth is a linear function of deposition flux and an inverse function of sample temperature.

Diblock copolymer organization can be directed into continuous crystalline domains having ordered minority phases in a process known as graphoepitaxy. In graphoepitaxy forced alignment within microscopic features occurs provided certain dimensional constraints are satisfied. Graphoepitaxy was attempted to precisely locate 20 nm diameter features for selective Ge or Si deposition and initial studies are presented.

In addition to precise nanoparticle positioning studies, kinetic studies were performed using the  $\text{Ge}/\text{HfO}_2$  material system. Germanium hot wire chemical vapor deposition on unpatterned  $\text{HfO}_2$  surfaces was interpreted within the mathematical framework of mean-field nucleation theory. A critical cluster size of zero and critical

cluster activation energy of 0.4 to 0.6 eV were estimated. Restricting  $\text{HfO}_2$  deposition area to a 200 nm to 100  $\mu\text{m}$  feature-width range using  $\text{SiO}_2$  decreases nanoparticle density compared to unpatterned surfaces. The studies reveal the activation energies for surface diffusion, nucleation, and Ge etching of  $\text{SiO}_2$  are similar in magnitude. Comparable activation energies for Ge desorption, surface diffusion and cluster formation obscure the change with temperature an individual process rate has on nanoparticle growth characteristics as the feature size changes.

## Table of Contents

List of Figures .....	xi
Chapter 1 – Introduction to Selective Semiconductor Nanocrystal Deposition on Amorphous Dielectric Surfaces.....	1
1.1 – Nanocrystals – Controlled Deposition Motivation .....	1
1.2 – Thermal Chemical Vapor Deposition .....	4
1.3 – Hot Wire Chemical Vapor Deposition.....	8
1.4 – Thermal Stability of Adatoms on Insulator Surfaces.....	10
1.5 – Diblock Copolymers .....	13
1.6 – Confined Area Nanoparticle Deposition.....	17
1.7 – Dissertation Overview.....	19
References .....	20
Chapter 2 – Experimental Methods.....	27
2.1 Chemical Vapor Deposition .....	27
2.2 Electron Beam Lithography .....	28
2.3 Diblock Copolymer Patterning.....	30
2.4 Graphoepitaxy .....	31
References .....	32
Chapter 3 – Investigation of Volmer-Weber growth mode kinetics for germanium nanoparticles on hafnia .....	34
3.1 Introduction .....	34
3.2 Experimental Procedure and Methods.....	36
3.3 Results.....	38
3.4 Discussion .....	48
3.5 Summary .....	51
References .....	52
Chapter 4 – Ge Nanoparticles in Organized Nanometer Scale HfO <sub>2</sub> Confined Area .....	55
4.1 Introduction .....	55

4.2 Experimental Procedures and Methods.....	57
4.3 Results.....	59
4.4 Discussion .....	68
4.5 Summary .....	71
References.....	71
Chapter 5 - Selective silicon nanoparticle growth on high density arrays of silicon nitride.....	76
5.1 Introduction .....	76
5.2 Experimental Procedure.....	79
5.3 Results.....	82
5.4 Discussion .....	95
5.5 Summary .....	97
References.....	98
Chapter 6 – Graphoepitaxy Development .....	102
6.1 Introduction .....	102
6.2 – Experimental Methods .....	106
6.3 – Results and Discussion.....	112
References.....	119
Chapter 7 – Summary and Future Work.....	121
7.1 Continued Kinetics Study.....	123
7.2 Continued Confined Deposition Study .....	124
7.3 Graphoepitaxy .....	127
References.....	128
Appendix.....	129
Academic History/Pedigree .....	129
Bibliography.....	130
Vita .....	137

## List of Figures

Figure 1.1: Silicon nanocrystal based FET flash memory transistor .....	2
Figure 1.2: SEM images of Ge nanoparticles on HfO <sub>2</sub> surface using thermal CVD, 850 K, 480,000 Langmuir GeH <sub>4</sub> , diameter range = 5-25 nm, density = $2 \times 10^{10} \text{ cm}^{-2}$ ....	4
Figure 1.3 Diagram showing various types of nucleation sites found on a silicon dioxide surface: a) silicon dangling bond b) siloxane bridge c) silanol group.....	6
Figure 1.4 Three potential fates of adatoms (black circles): a) combination with other adatom(s) and nucleation b) addition to an existing island c) desorption from the surface and return to vapor phase. ....	7
Figure 1.5: Setup found in hot wire CVD process depositing from the precursor disilane. The $\geq 1500^\circ\text{C}$ tungsten filament is 3-7 cm from the deposition surface. The radical flux is designated by the silicon radical species (*) and the arrow shows the flux direction.....	9
Figure 1.6 TPD spectra for SiO <sub>2</sub> and Si <sub>3</sub> N <sub>4</sub> samples after (i) annealing at 1100 K for 15 min, (ii) exposure to 240 L disilane, (iii) cracking induced deposition of 1ML silicon, (iv) cracking induced deposition of 9 ML, and (v) exposure of agglomerated nanoparticle covered surfaces to 240 L disilane.....	11
Figure 1.7 TPD data for 1.0 ML Ge on HfO <sub>2</sub> and 0.7 ML Ge on SiO <sub>2</sub> for a) the signal for $m/e$ of 74, indicating Ge species desorption, and b) the signal for $m/e$ of 90, indicating volatile GeO desorption.....	12
Figure 1.8 Three morphologies created after self-assembly with varying relative polymer species composition using diblock copolymers .....	14

Figure 1.9 Left: cross section diagram of spherical one monolayer on a deposited onto a lateral plane Right: cross section diagram of a cylindrical phase thin film on a lateral plane having the cylinders oriented perpendicular with the substrate. ....	15
Figure 1.10 SEM image of self-assembled poly(styrene-b-methyl methacrylate) diblock copolymer thin film (30 % methyl methacrylate, 70 % styrene, $M_n = 67,000$ ) after the cylinders were selectively removed using glacial acetic acid .....	16
Figure 1.11 Cross section diagram of a substrate having vertical topography and spherical morphology diblock copolymer thin film being confined by the topography after self-assembly.....	17
Figure 1.12 The left diagram is a cross section of the insulator stack before patterning. The right diagram is the insulator cross section after a soft mask was used for controlled removal of the pattern layer being ready for CVD. ....	18
Figure 2.1 Diagram of EBL equipment set up within a vacuum chamber. ....	29
Figure 2.2 a) Graphoepitaxy using poly(styrene-b-methyl methacrylate) thin films within ~60 nm deep square box patterned within plasma enhanced CVD deposited silica on a Si(100) substrate. The 250 nm wide box was patterned using EBL. The dark spots are where the cylinders were removed from. b) Similar graphoepitaxy as Part a) except the features are ~250 nm wide parallelograms.....	32
Figure 3.1 a.) Ge 2p <sub>3/2</sub> XPS peak following the evolution of GeO <sub>x</sub> (1220 eV) and Ge <sup>0</sup> (1217 eV) after Ge deposition on extended hafnia surfaces at 0.6 ML/min and 750 K. The top trace is the baseline signal. b) SEM image of HWCVD Ge nanoparticles at 775 K, 0.6 ML/min flux, and 10 ML exposure. The nanoparticles are the bright spots and range from 5-20 nm in diameter. The particle density is $1 \times 10^{11} \text{ cm}^{-2}$ .....	39

Figure 3.2 a) Particle density versus HWCVD Ge exposure on extended HfO <sub>2</sub> surfaces, 750 K, 0.6 (▲) and 2.1 (■) ML/min fluxes. b) Average Ge particle density versus temperature on extended HfO <sub>2</sub> surfaces. The data points are averages of the 2.1, and 4.2 ML/min fluxes for 8 ML exposure.....	41
Figure 3.3 a) Saturation Ge particle density versus deposition flux at 750 (▲) and 775 (■) K on extended HfO <sub>2</sub> surfaces for 8 ML exposure. b) Saturation Ge particle density (8 ML) versus deposition flux at 700 (▲) and 725 (■) K on extended HfO <sub>2</sub> surfaces for 8 ML exposure.....	42
Figure 3.4 a) Optical microscope image of Ebeam lithography patterned PMMA mask on the silicon dioxide top layer before RIE. Feature sizes 600 nm to 100 μm are displayed. b) SEM image of 200 nm wide hafnia box feature confined with the brighter silicon dioxide layer. The three circles surround the largest of the 11 Ge nanoparticles deposited at 775 K, 0.1 ML/min, 8 ML exposure.....	43
Figure 3.5 a) Ge particle density versus hafnia box size from 8 ML exposure with various combinations of the extremes for temperature (K)/flux (ML/min) conditions: 700/0.1 (▲), 700/4.2 (■), 775/0.1 (●), and 775/4.2 (✱) units are K*ML/min. b) Ge particle density versus HfO <sub>2</sub> feature size, 775 K, 8 ML exposure and fluxes: 0.1 (▲), 0.6 (■), 2.1 (●), and 4.2 (✱) units are ML/min. c) Average particle density for 1-10 μm HfO <sub>2</sub> features (▲) and extended surfaces (■) versus flux rate, 775 K, 8 ML exposure. ....	45
Figure 3.6 a) Ge particle density versus HfO <sub>2</sub> feature size, 0.1 ML/min, 8 ML exposure and temperatures: 700 (▲), 725 (■), 750 (●), and 775 K (✱). b) Average particle density for 1-10 μm HfO <sub>2</sub> features (▲) and extended surfaces (■) versus temperature, 0.1 ML/min, 8 ML exposure.....	47

- Figure 4.1 a) SEM image of 9.4 ML, 800 K selective Ge deposition upon 3 s HF etched SiO<sub>2</sub> patterned HfO<sub>2</sub> pores. Inset are representative, higher resolution SEM images from the same sample that have been digitally enhanced to increase the contrast showing (i) an empty pore, (ii) a singlet and (iii) a doublet. b) Ge 2p<sub>3/2</sub> XPS peak data confirming selective deposition: (1) baseline on unpatterned SiO<sub>2</sub> (2) after 9.4 ML deposition on unpatterned SiO<sub>2</sub> (3) 9.4 ML Ge deposited on patterned surface with 3 s HF etch (4) 7.5 ML Ge exposure upon unpatterned HfO<sub>2</sub> surface. c) SEM image of selective Ge deposition upon 3 s HF etched patterned sample after 0.8 ML room temperature seeding followed with an 8.6 ML exposure at 800 K. .... 60
- Figure 4.2. a) Plot of Ge nanoparticle density versus Ge exposure for 1 s (●) and 3 s (▲) HF etched patterned samples, and unpatterned HfO<sub>2</sub> (\*). The horizontal line indicates the patterned pore density of  $6 \times 10^{10} \text{ cm}^{-2}$ . b) SEM image of 15 ML, 800 K Ge deposition on an unpatterned HfO<sub>2</sub> surface. .... 62
- Figure 4.3 Comparison of (a) large (15 nm), (b) medium (10 nm), and (c) small (5 nm) sized nanoparticles as a function of Ge exposure for the 3 s HF etched SiO<sub>2</sub> pores at 800 K. .... 65
- Figure 4.4. a) SEM images demonstrating relative nanoparticle placement in a given pore on a 3 s HF etched patterned sample grown at 800 K. Left image is edge placement, center image is center placement, and right image is two particles in one pore (doublet). b) Plot of nanoparticle placement represented as the ratio of edge/center vs. Ge exposure for 1 s and 3 s HF etched patterned pores counting only pores with one nanoparticle present (singlet). .... 67
- Figure 4.5: a) Plot of the pore fraction with continuous Ge films vs. surface temperature upon 20 nm pore samples seeded with 0.4 ML Ge and later exposed to 5.2 ML Ge

exposure during HWCVD. b) Plot of pores with nanoparticles as particle fraction vs. surface temperature for the seeded 20 nm pore samples exposed to 5.6 ML total Ge exposure. ....	68
Figure 5.1 XPS showing Si 2p signals for thermal CVD at 900 and 975 K. The $2.0 \times 10^{-8}$ Torr $\text{Si}_2\text{H}_6$ partial pressure is equivalent to the background pressure used during the 0.3 ML/min HWCVD flux depositions. CVD exposure lasted 50 min or the equivalent amount of time required for a 15 ML HWCVD exposure originating at the tungsten filament generating radicals.....	83
Figure 5.2 SEM images of 4 min thermal CVD on extended $\text{Si}_3\text{N}_4$ at 975 K and a disilane pressure of $1 \times 10^{-4}$ Torr. a) The $\text{SiO}_2$ hard mask was removed using HF and the underlying $\text{Si}_3\text{N}_4$ had a 20 s exposure to the 200 W $\text{CHF}_3/\text{O}_2$ RIE chemistry used in processing patterned samples. The particle density is $1 \times 10^{11} \text{ cm}^{-2}$ and particles range in diameter from 5-25 nm. b) The negative image of Part a. c) The $\text{SiO}_2$ hard mask was removed using HF without any further steps and given the same thermal CVD as Part a. The particle density is $2 \times 10^{10} \text{ cm}^{-2}$ and particles range in diameter from 5-10 nm. d) The negative image of Part c.....	86
Figure 5.3 a) Fraction of pores that contain Si films versus temperature after 3 min (18,000 L) thermal CVD. Note all pores contained Si in the form of nanoparticles or a continuous film. b) Average particle diameter that considers a film to be a 17 nm particle.....	88
Figure 5.4 Curves showing the effects of changing exposure during HWCVD at 975 K for a flux of 0.3 ML/min; a) Si nanoparticle particle density, b) fraction of filled pores containing ensembles consisting of a single Si particle ( $\blacktriangle$ ), two Si particles ( $\blacksquare$ ), three Si particles ( $\bullet$ ), four Si particles ( $*$ ), and c) fraction of all available pores showing any type of particle ensemble.....	90

Figure 5.5 a) SEM image of a patterned $\text{Si}_3\text{N}_4$ HWCVD sample grown at 975 K, 0.4 ML/min flux, and 6 ML total exposure. The dark circles are the bottoms of the $\text{Si}_3\text{N}_4$ pores and the irregular, faint white objects in the circles are the Si nanoparticles. The continuous bright white surface surrounding the $\text{Si}_3\text{N}_4$ pores is the $\text{SiO}_2$ hard mask. b) The image was digitally enhanced with light blue representing the nanoparticles on the dark $\text{Si}_3\text{N}_4$ .....	92
Figure 5.6 Curves showing the effects of changing the flux during HWCVD at 975 K for a constant exposure of 6 ML; a) fraction of all pores showing any particle ensemble combination, b) overall Si nanoparticle density, and c) average nanoparticle diameter.....	93
Figure 5.7 Curves showing the effects of changing the temperature during HWCVD at a fixed flux of 0.3 ML/min and total exposure of 6 ML; a) fraction of all pores showing any particle ensemble combination, b) overall Si nanoparticle density, and c) average nanoparticle diameter. ....	94
Figure 6.1 Left: cross section diagram of a cylindrical phase thin film on a lateral plane having the cylinders oriented perpendicular with the substrate. Right: SEM image of self-assembled poly(styrene-b-methyl methacrylate) diblock copolymer thin film (30 % methyl methacrylate, 70 % styrene, $M_n = 67,000$ ) after the cylinders were selectively removed using glacial acetic acid .....	102
Figure 6.2 SEM image of self-assembled poly(styrene-b-methyl methacrylate) diblock copolymer thin film (30 % methyl methacrylate, 70 % styrene, $M_n = 67,000$ ) after the cylinders were selectively removed using glacial acetic acid. ....	104
Figure 6.3 Cross section diagram of a patterned trench and cylindrical morphology diblock copolymer thin film being confined by the topography after self-assembly .....	105

Figure 6.4 SEM image of seven cylinder rows in a ~250 nm wide trench after graphoepitaxy using the poly(styrene-b-methyl methacrylate) diblock copolymer .....	106
Figure 6.5 Diagram showing the position of EBL patterns on a 4 inch wafer done by Aaron Gin, CINT-SNL. Each square on the wafer represents one full pattern with squares, lines, and parallelograms of all four sizes. ....	108
Figure 6.6 Computer aided draft image showing how individual EBL patterns showing how the lines, square, and parallelograms are oriented with respect to each other within one patterning die.....	109
Figure 6.7 Computer aided draft image showing how 175 nm features are presented in EBL patterns. The lines, square, and parallelograms are closely oriented with respect to each other. a) The initial pattern. b) The second revised pattern taking in consideration the movement of polymer.....	110
Figure 6.8 Computer aided draft image showing how 175 nm line features are presented in EBL patterns. Lines that are arranged in clusters parallel with each other have various widths. a) The initial pattern. b) The second revised pattern taking in consideration the movement of polymer.....	111
Figure 6.9 SEM image of two ~800 nm wide trenches filled with poly(styrene-b-methyl methacrylate). The center of the image is the elevated topography, while the left and right portions filled with dark shapes are two separate trench bottoms. ....	113
Figure 6.10 SEM features of etched silica features ~60 nm deep using the second, more successful patterning process. a) Etched square ~300 nm in width. b) Etched parallelogram with side lengths of ~300 nm.....	114
Figure 6.11 Graphoepitaxy of cylindrical poly(styrene-b-methyl methacrylate) within a ~350 nm wide line the step height is ~60 nm. Dark circles represent the voids left	

after the PMMA cylinders were removed. The hexagonal closed pack order is achieved using the smooth sidewalls obtained from the new patterning process.	115
Figure 6.12 SEM image of three 350 nm wide line features having a 60 nm step height. Poly(styrene-b-methyl methacrylate) has varying percentage of proper order where cylinders are separated and perpendicular with the substrate within the observed field of view: a) 30 % good order b) 60 % good order c) 75 % good order	116
Figure 6.13 Process diagram of the process incorporating graphoepitaxy into the precise nanoparticle placement scheme using the Ge/HfO <sub>2</sub> material system. The scheme would accomplish dual-level patterning of HWCVD nanoparticles.	118
Figure 7.1 SEM image of thin film polystyrene template obtained from poly(styrene-b-methyl methacrylate) [80% styrene, 20% methyl methacrylate, $M_n = 78,000$ ] deposited on SiO <sub>2</sub> surface. The monolayer was partially formed allowing access to the minority spherical methyl methacrylate with acetic acid removing the spheres selectively. The dark spots are pores having ~13 nm diameters and a $1.2 \times 10^{11} \text{ cm}^{-2}$ density.	126

# **Chapter 1 – Introduction to Selective Semiconductor Nanocrystal Deposition on Amorphous Dielectric Surfaces**

## **1.1 NANOCRYSTALS – CONTROLLED DEPOSITION MOTIVATION**

Properties of materials begin to change as physical dimensions decrease since the ratio of atomic surface area to volume increases. The resultant properties change with size accordingly between those found in the bulk and the properties associated with individual atoms. Semiconductor clusters with less than 10,000 atoms have a size dependent band gap where interactions between neighboring atoms fill the band gap through band edges from the band center as more atoms are added to a cluster [1]. Material properties dependent on the band gap such as optical emission, conductance, and Coulomb blockade are dominated by band edge effects in nanoscale materials [2]. The property of interest for memory devices is the Coulomb blockade effect [3]. The quantizing of electron charges within individual nanocrystals enables the electron storage to be precise even when the electron transportation process fluctuates. The floating gate field-effect transistor (FET) memory devices described in the following paragraphs take advantage of Coulomb blockade charge storage quantization.

Since the microelectronics industry was started in the 1960's, feature dimensions have been shrinking at a continuous rate, enabling each successive generation to process data at a faster rate than the previous generation. The faster operation is based on increasing the transistor density upon the chips, increasing the simultaneous calculations per device and a smaller transistor size that means electrons travel less distance during each transistor operation.

The ever shrinking component dimensions are approaching the physical limits at which the standard complimentary metal on semiconductor (CMOS) materials operate, making the smaller device operation impossible using traditional silicon based technology [4]. The technology used in flash memory FET devices is similar to CMOS while following the same scaling trend in the past few decades. Flash memory FET devices are estimated to have 45 nm gate lengths by the year 2010 [5]. One new approach decreasing power consumption and potentially achieving devices with these future dimensions, uses a floating gate FET incorporating nanoparticles [6-10]. The new memory devices replace the traditional floating gate poly-Si retention layer with a layer of semiconductor or metal nanocrystals. The device schematic based on Si nanoparticles is seen below [3] in Figure 1.1. Operation of the transistor is dependent on using

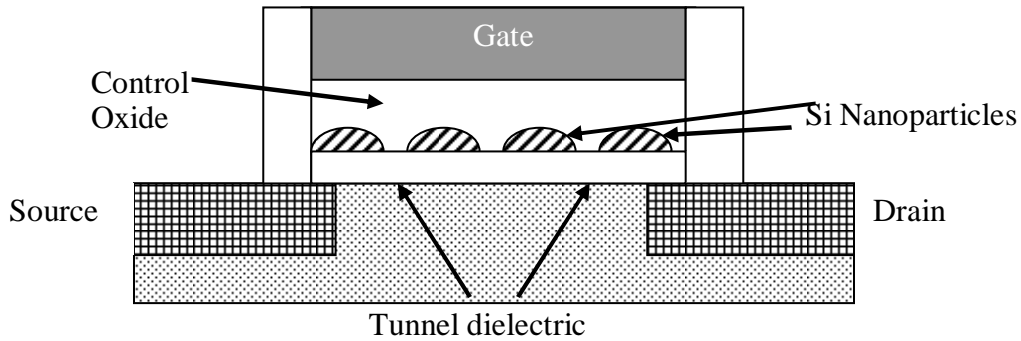


Figure 1.1 Silicon nanocrystal based FET flash memory transistor [3]

the nanoparticle layer as an electron storage region [11]. The device without any charge present in the nanoparticle layer is in computer logic state “0”. Inducing a high positive voltage on the gate and drain encourages hot carrier effects wherein electrons tunnel through the tunnel dielectric into the nanoparticle layer from the substrate below. The transistor is now in computer logic state “1”. Reversing the electron flow and erasing the device occurs by placing a high positive voltage on the source; electrons leave the

nanoparticle layer in a process known as Fowler-Nordheim tunneling, bringing the transistor into state “0” again. The overall band gap is altered by electrons charging the particles, thus, changing the device threshold voltage. Reading the band gap change is done by placing a small voltage on the drain and current will flow between the source and drain if the device is in state 0. Accordingly, negligible current flows between source and drain if the device is in state 1.

Optimal operation of the nanocrystal based FET depends on nanocrystal size and lateral particle placement. The nanocrystalline based device is advantageous over the continuous Si film devices since electron flow in and out of the Si nanoparticle layer is discrete [12]. The nonvolatile operation has electrons remaining indefinitely trapped in the nanoparticles from Coulomb blockade compared to a continuous film gradually increasing charge over time. Optimal nanocrystal device operation has proper sized particles for the maximum band gap change when charge is injected. Nanoparticles that are too large do not give the device a large, distinct band gap step change for easy voltage reading between the on and off states [12,13]. Nanoparticles that are too small degrade device performance by having undesired quantum confinement effects [1]. For example, Si particle based devices have best operation when the particle layer is 5 nm particles placed laterally 5 nm apart resulting in a particle density of approximately  $10^{12} \text{ cm}^{-2}$  [3]. If nanoparticles are spaced too close together laterally, electrons tunnel through the encapsulation oxide into neighboring particles as the device is being erased preventing the nanoparticle layer from completely discharging electrons and returning to a true “0” state.

## 1.2 – THERMAL CHEMICAL VAPOR DEPOSITION

Chemical vapor deposition (CVD) synthesis of semiconductor nanoparticles has advantages over other synthesis routes. First, CVD is a standard technique within the microelectronics industry used in depositing semiconductors, especially silicon. Second, the process tends to be cleaner than most synthesis routes using solutions or high pressure vapors. Finally, the CVD process is compatible with vacuum systems where it is easy to analyze the deposited material *in situ* with analytical equipment. Silicon, germanium, or silicon/germanium alloyed nanoparticles have been deposited upon insulators using CVD. These structures were later fabricated into working nanocrystal flash memory devices [3,14-17]. Figure 1.2 presents a scanning electron microscopy (SEM) image showing germanium nanoparticle CVD on a hafnia surface.

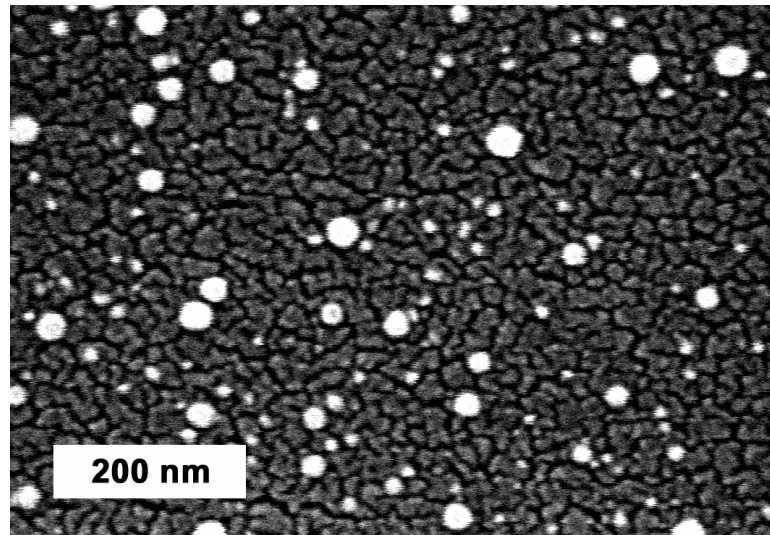


Figure 1.2 SEM images of Ge nanoparticles on HfO<sub>2</sub> surface using thermal CVD, 850 K, 480,000 Langmuir GeH<sub>4</sub>, diameter range = 5-25 nm, density =  $2 \times 10^{10} \text{ cm}^{-2}$ .

In thermal CVD, a precursor decomposes directly on the substrate surface. This occurs at high enough temperatures to break bonds (starting the decomposition) and facilitate removal of secondary ligand species not incorporated within the film. The typical hydride precursors used in silicon deposition are silane ( $\text{SiH}_4$ ) and disilane ( $\text{Si}_2\text{H}_6$ ) and the equivalent for germanium is germane ( $\text{GeH}_4$ ). Silicon nanoparticle deposition typically uses disilane since it is more reactive with silicon dioxide, with 1/4 the incubation time of silane before initial nucleation [18]. The quicker adsorption results in denser nanoparticles by increasing the adatom concentration. For example, disilane follows the mass action found in Rxn. 1.1 with available active surface sites ( $S^*$ ) on an insulator.



The first step is adsorption of the  $\text{SiH}_3$  radical [19] with the active surface site. Second, the bonds between the adsorbed silicon atom and the hydrogen atoms are cleaved resulting in the hydrogen reacting and leaving in diatomic form. Each adsorbed monomer on the surface is referred to as adatom.

Nucleation and the addition of adatoms to insulator surfaces are influenced by surface defects. Nucleation is not favored for heterogeneous systems unless an energy reducing intermediate favors the process [20]. Several types of defects are found on insulator surfaces, some serve as nucleation sites while others increase surface activity. Greater quantities of defects typically result in a higher deposited nanoparticle density. For example, silicon dioxide is a typical amorphous insulator having three active intermediate surface sites: silanols or hydroxyl groups ( $\text{Si-OH}$ ), siloxane bridges ( $\text{Si-O-Si}$ ), and silicon dangling bonds ( $\text{Si-}$ ) [21] as seen in Figure 1.3. The active siloxane

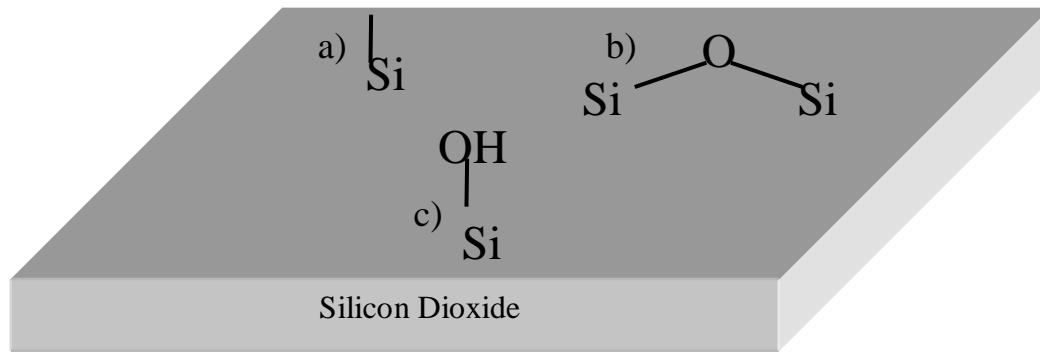


Figure 1.3 Diagram showing various types of nucleation sites found on a silicon dioxide surface: a) silicon dangling bond b) siloxane bridge c) silanol group [21].

bridges are a fixed quantity on an insulator surface and have been demonstrated as nucleation sites if physically strained [22]. The dangling bonds are known nucleation sites and their concentration can be increased through physically damaging surface bonds with an electron beam, but the resultant oxide is often too poor for devices [23,24]. In a more desirable manner, silanol groups may be added through exposing the silicon dioxide surface to a dilute hydrofluoric acid (HF) bath without diminishing the insulator electrical integrity [22,25]. It is assumed that the silanol groups are not nucleation sites, but the defects increase the surface reactivity to hydride gases leading to a greater adatom concentration.

Adatoms have three potential fates after being added to the surface as shown in the diagram in Figure 1.4. Adatoms may either nucleate, join an existing island, or desorb from the deposition surface returning to the vapor phase. Critical cluster formation is a concept from various epitaxy theories including mean-field nucleation theory [26-28] and corresponds to the number of adatoms required for the formation of a critical cluster,  $i^*$ . Nucleation occurs when an additional adatom is added to a critical

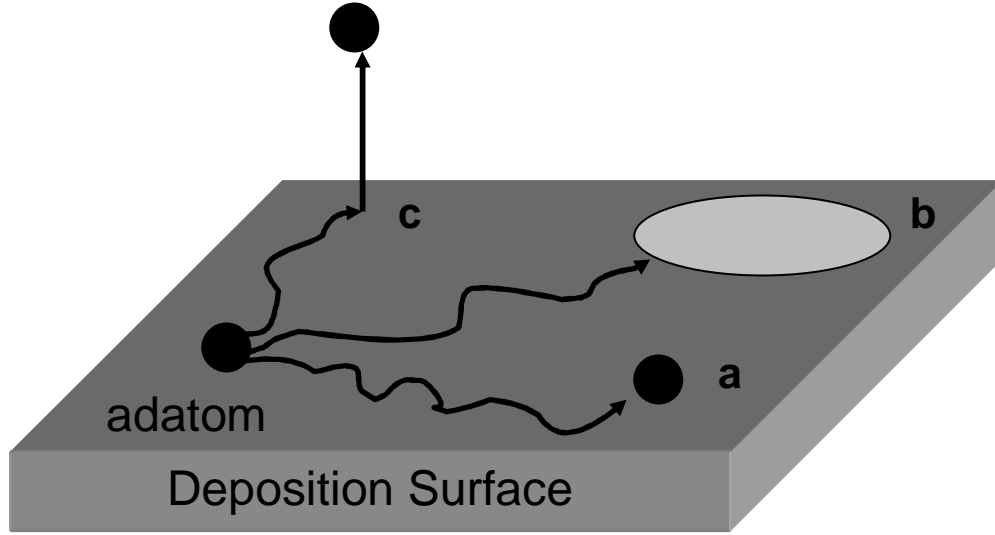


Figure 1.4 Three potential fates of adatoms (black circles): a) combination with other adatom(s) and nucleation b) addition to an existing island c) desorption from the surface and return to vapor phase.

cluster producing a particle of size  $i^*+1$ , which is assumed to be stable against decomposition. Continued nanoparticle growth occurs when adatoms are added to existing stable clusters or larger existing particles. When adatoms desorb from the surface, nanoparticle deposition is reduced by lowering the adatom concentration preventing nucleation or continued particle growth. The three adatom processes occur randomly on the deposition surface.

Mean-field nucleation theory relates the density of stable islands/nanoparticles,  $N_{SAT}$ , to the incident flux,  $F$ , and temperature [29-31]. Nucleation depends on the ability to form stable adatom grouping upon a nucleation site. Knowledge of the material system dependent critical cluster size,  $i^*$ , is vital to control the resultant nanoparticle density, since the rate of stable nuclei formation is dependent upon the average surface adatom concentration,  $\bar{n}$ , to the  $i^*+1$  power, i.e.  $\text{rate} \propto \bar{n}^{i^*+1}$  [27]. Critical cluster

formation through adatom diffusion requires the intersection of enough diffusing adatoms to form  $i^*$ -sized clusters and adatoms need enough energy to overcome the critical cluster formation energetic barrier,  $E^*$  [27]. The majority of deposition kinetic studies have been performed using molecular beam epitaxy (MBE) and have followed Stranski-Krastanov growth mode systems in which a wetting layer forms first on a crystalline substrate followed by island growth [26,29,30,32]. Stranski-Krastanov systems typically have  $i^*$  values consisting of several adatoms, for example, Ge/Si(111) is 5 [32] and Si/Si(111) is 5-7 [26]. Volmer-Weber growth mode in which islands form on the substrate typically occurs with heterogeneous systems where the deposition material does not wet the surface, resulting in islands. The  $i^*$  value reported for Volmer-Weber mode systems are zero for Ge/SiO<sub>2</sub> [33] and were estimated as 1 for Si/SiO<sub>2</sub> [30]. Nothing to date has been reported on  $E^*$  or  $i^*$  for the Ge/HfO<sub>2</sub> system and forms the basis for Chapter 3.

### 1.3 – HOT WIRE CHEMICAL VAPOR DEPOSITION

The technique known as hot wire CVD (HWCVD) decomposes the precursor against a heated tungsten filament (~1500 °C) or cracking filament generating hydride radicals sent to the insulator surface through line of sight. The radicals react with the surface and become adatoms [34]. The radicals do not have unintentional collisions with other precursors since the mean free path for a molecule at deposition pressures ( $< 10^{-5}$  Torr) is greater than an order of magnitude of the distance between the cracking filament and deposition surface. The insulator substrate is heated to greater than 750 K [35], and greater than 540 K [36] for Si and Ge based hydrides, respectively, to facilitate further decomposition of the hydride radicals, leading to the removal of hydrogen and the generation of adatoms on the substrate surface. Nucleation and particle growth processes

then occur. Figure 1.5 is a diagram showing the process. Silicon deposited on the surface has less than 0.1% tungsten from the catalytic reaction on the filament [37].

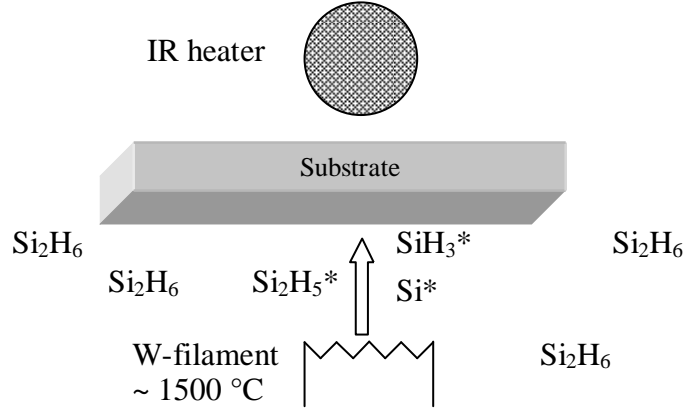


Figure 1.5 Experimental setup found in hot wire CVD process depositing from the precursor disilane. The  $\geq 1500$  °C tungsten filament is 3-7 cm from the deposition surface. The radical flux is designated by the silicon radical species (\*) and the arrow shows the flux direction.

HWCVD has two advantages for experimental purposes over the traditional thermal CVD. First, the deposition flux,  $F$ , is easily controlled through both pressure,  $P$ , scaling as  $F \sim P$  and the distance between the cracking filament and deposition surface, which scales as a single isotropic deposition source,  $F \sim 1/d^2$  [36]. Through varying the incident flux rate, we are able to investigate fundamental nucleation and growth kinetics using mathematical frameworks such as mean-field nucleation theory, which is not possible in thermal CVD [38]. Thermal CVD is limited by the adatom addition to the surface through precursor adsorption; this leaves the exact deposition flux as an unknown variable and theory is invalid. Second, HWCVD also generates a higher adatom concentration at ultra-high-vacuum (UHV) pressures creating higher particle densities if desired [39].

#### 1.4 – THERMAL STABILITY OF ADATOMS ON INSULATOR SURFACES

Nanoparticle deposition is dependent upon the ability to accumulate adatoms, therefore, adatom desorption must remain relatively low compared to nucleation and particle growth for successful adatom accumulation. Temperature programmed desorption (TPD) [35,36] is an *in situ* experimental procedure capable of determining the thermal stability of a deposited material on a given surface. The deposition material is physically placed on the substrate through physical vapor deposition (PVD) at room temperature. The sample surface is then placed in proximity of an *in situ* mass spectrometer and the sample temperature is increased at a constant rate. The mass spectrometer detects deposited material desorbing from the sample when the surface temperature reaches the point of thermal instability between the deposited material and the surface.

Silicon stability on SiO<sub>2</sub> is dependent upon on the surface temperature in vacuum conditions. Temperature programmed desorption data seen in Figure 1.6a represents several desorption peaks of various monolayer (1 monolayer = 1 ML =  $6.8 \times 10^{14}$  atoms/cm<sup>2</sup>) exposures of Si from the SiO<sub>2</sub> surface [35]. The mass spectrometer does not detect any desorbing Si in the form of volatile SiO beginning at 840 K having the

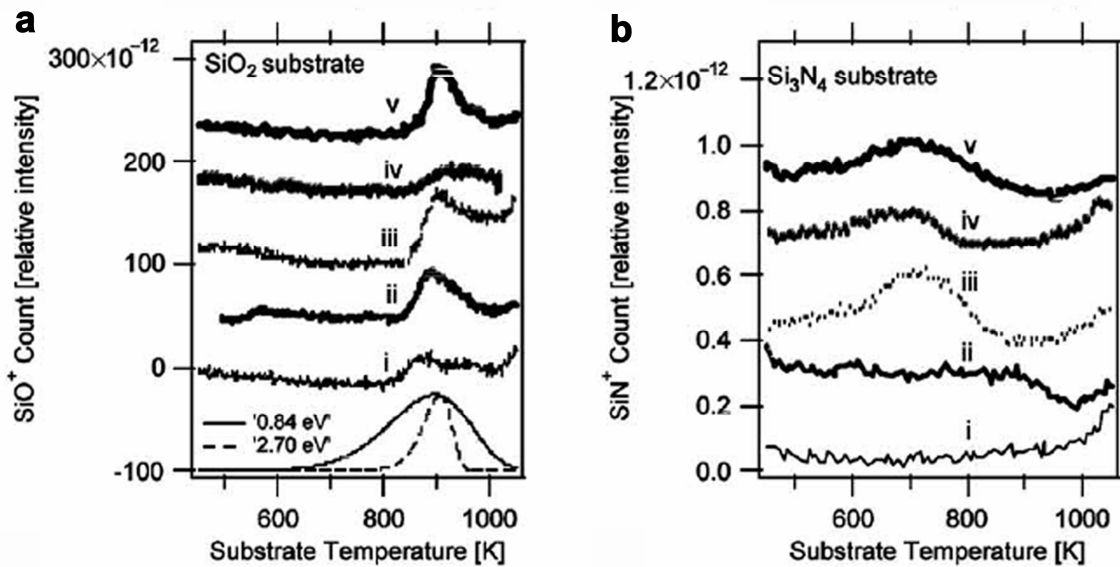


Figure 1.6 TPD spectra for SiO<sub>2</sub> and Si<sub>3</sub>N<sub>4</sub> samples after (i) annealing at 1100 K for 15 min, (ii) exposure to 240 L disilane, (iii) cracking induced deposition of 1 ML silicon, (iv) cracking induced deposition of 9 ML, and (v) exposure of agglomerated nanoparticle covered surfaces to 240 L disilane [35]. The activation energies listed in part a are best fit linear lines to experimental data. The 2.70 eV [35] value was obtained from the TPD data presented in this figure and 0.84 eV [40] was reported from experimental data using a Si effusion beam to etch silica.

desorption peak reach a maximum at 900 K. Using a best fit line, the process is assumed a first order rate kinetic reaction estimating the activation energy as 2.70 eV with a 10<sup>14</sup> prefactor. Reaction 1.2 is the mass action balance for the conversion of the available Si reacting with SiO<sub>2</sub> into volatile SiO during the sample heating. Streit and Allen report similar desorption results with the Si etching SiO<sub>2</sub>



beginning at 975 K using an evaporative Si beam, but they report a lower activation energy of 0.84 eV having a 7 × 10<sup>17</sup> prefactor [40]. The SiO<sub>2</sub> is actually stable at these thermal conditions without the presence of adsorbed Si. In comparison, Si is stable on

Si<sub>3</sub>N<sub>4</sub> surfaces up to 1000 K as seen in Figure 1.5b. It should be possible to selectively deposit Si on a Si<sub>3</sub>N<sub>4</sub> surface and not on SiO<sub>2</sub> at temperatures greater than 900 K.

Germanium stability on SiO<sub>2</sub> is also dependent upon surface temperature. Temperature programmed desorption data seen in Figure 1.7a represents desorption of 1.0 monolayer (1 ML = 6.3×10<sup>14</sup> atoms/cm<sup>2</sup>) of Ge from SiO<sub>2</sub> [36]. The mass spectrometer does not detect any desorbing Ge from the SiO<sub>2</sub> in the form of GeO until 500 K. The desorbing Ge<sup>0</sup> peak begins at 750 K. The exact removal mechanism of Ge

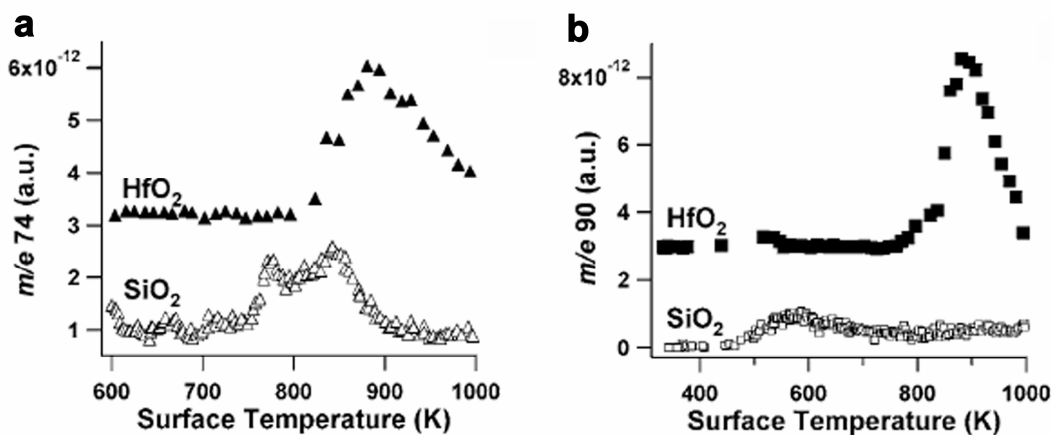
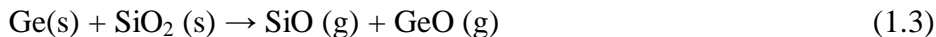


Figure 1.7 TPD data for 1.0 ML Ge on HfO<sub>2</sub> and 0.7 ML Ge on SiO<sub>2</sub> for a) the signal for  $m/e$  of 74, indicating Ge species desorption, and b) the signal for  $m/e$  of 90, indicating volatile GeO desorption [36].

from the SiO<sub>2</sub> surface is not known at the time of this publication. It is suggested that the appearance of Ge as volatile GeO has the Ge reacting with the SiO<sub>2</sub> according to the mass action balance seen in Rxn. 1.3 [41]. The second reported mechanism [33] has Ge



desorbing from the surface without any chemical interaction with the SiO<sub>2</sub> surface having an activation energy of 0.42 eV. Li *et al.* argues the volatile GeO forms in a reaction of Ge with both Si and SiO<sub>2</sub> [33]. In comparing Ge stability, Figure 1.7b has the Ge being stable on HfO<sub>2</sub> surfaces up to 800 K before the first major desorption feature begins. The

approximate selective deposition thermal range of depositing Ge on HfO<sub>2</sub> and not on SiO<sub>2</sub> is 700 - 800 K.

## 1.5 – DIBLOCK COPOLYMERS

Diblock copolymers are polymer systems synthesized with sections or blocks of one monomer species grafted onto a section of another species of polymer. Assume “M” is species 1 and “S” is species 2, individual polymer chains containing equivalent amounts of each monomer would appear as the diagram: M-M-M-M-M-S-S-S-S-S. The self-assembling systems have immiscible blocks and separate from opposite species when chains are mobile. Chain mobility is induced several ways through imbibing the polymer with solvent [42,43], evaporation of a common solvent allowing phase interface formation [44], or raising the temperature above the glass transition temperature for both polymers [45,46]. Greater polymer order is obtained through the interactions of electrical fields while the polymers are self-assembling [47]. Practical applications require complete polymer segregation into homogenous phases. Diblock systems are capable of complete separation if  $\chi N > 10.5$  [48] where  $\chi$  is the Flory-Huggins interaction chi-parameter and  $N$  is the degree of polymerization. The  $\chi$  value is typically used for polymer-solvent solubility and is relevant to our copolymer system since we are above the glass transition temperature making chains mobile, thus, behaving as an extremely viscous liquid. Second,  $\chi$  is dependent upon many factors such as the nature of the solvent, temperature, and polymer molecular weight [49]. This makes it impossible to know the actual value of  $\chi$  for a diblock polymer system during self-assembly since the solubility parameter is measured experimentally using extremely dilute solutions [49]. As solubility decreases between two species in a diblock copolymer,  $\chi$  increases to a larger value and smaller self-assembled features are possible.

Diblock copolymer phase morphology after self-assembly (Figure 1.8) is dependent upon the relative amounts of monomer species present. The monomer species

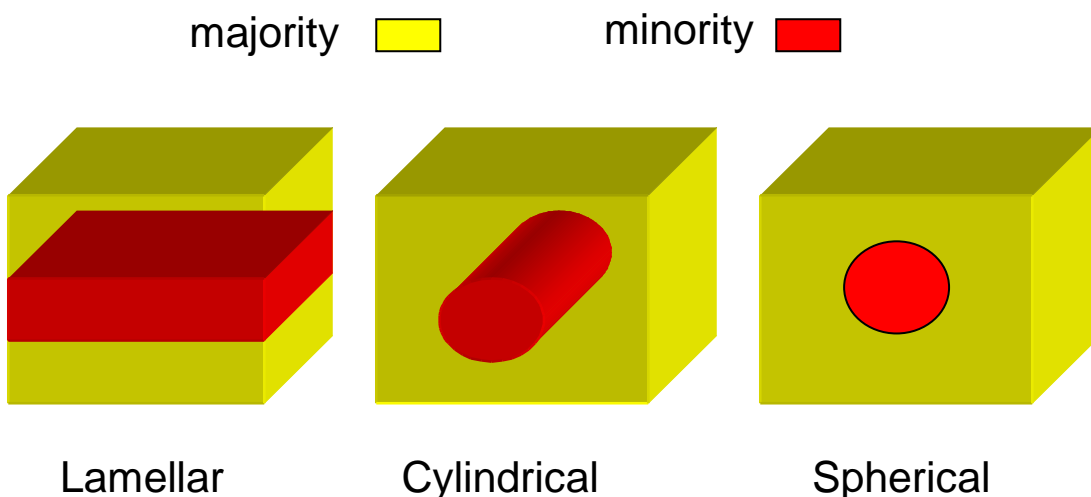


Figure 1.8 Three morphologies created after self-assembly with varying relative polymer species composition using diblock copolymers. Yellow represents the majority component while red represents the minority component.

are typically categorized into majority and minority components. If monomer composition is equivalent at 50% each, lamellar morphology forms. The cylindrical morphology is named because the 30 % minority phase forms cylinders enclosed by the 70 % majority component. The minority component forms spheres when the composition is 80% and 20%, majority and minority components, respectively.

Incorporating diblock copolymers into useful patterning masks requires control over both phase morphology and the phase orientation with respect to the substrate. Depositing thin films onto substrates is a method for utilizing diblock copolymers in patterning flat 2-D lateral surfaces. Removing one phase selectively, typically the minority phase leaves the continuous majority phase as a soft mask. For the practical purpose of patterning nanometer scale features for nanoparticles, individually isolated features are most easily achieved from cylindrical and spherical morphologies. Spherical

morphology diblock copolymer thin films deposited at the correct thickness deposits a monolayer (one layer) of spheres encased within the majority phase onto the surface as seen in Figure 1.9. The spherical monolayer has been used to transfer features as small

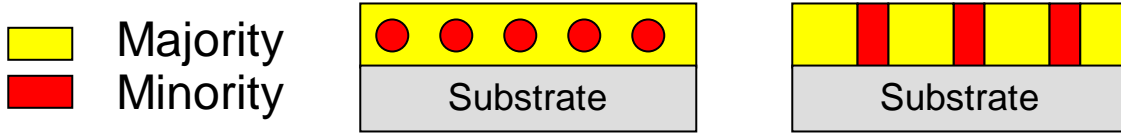


Figure 1.9 Left: cross section diagram of spherical one monolayer on a deposited onto a lateral plane Right: cross section diagram of a cylindrical phase thin film on a lateral plane having the cylinders oriented perpendicular with the substrate.

as 10 nm and densities on the order of  $8 \times 10^{11} \text{ cm}^{-2}$  [50]. Pattern transfer using encapsulated spheres requires an advanced  $\text{O}_2$  reactive ion etch [51] accessing the substrate before pattern transfer into the substrate is possible. The poly(styrene-*b*-methyl methacrylate) [30 % methyl methacrylate, 70 % styrene,  $M_n = 67,000$ ] cylindrical phase thin films [52,53] having the cylindrical phase oriented perpendicular with the substrate is a simpler way to pattern substrates. Cylinders are oriented in a perpendicular fashion using a combination of surface energy neutrality [54] and vertical confinement [45,55]. The surface energy neutrality is achieved using a random copolymer (40 % methyl methacrylate, 60 % styrene) monolayer chemically attached to the surface. Vertical confinement is achieved by depositing thin films at a  $37 \pm 4$  nm thickness. The methyl methacrylate cylinders are selectively removed using glacial acetic acid giving direct access to the substrate through the remaining polystyrene template with 20 nm pores at  $6 \times 10^{10} \text{ cm}^{-2}$  pore density. The degree of polymerization,  $N$ , is  $\sim 690$  and it is estimated that this molecular weight polymer has a  $\chi N$  factor of  $\sim 11.0$  [55], therefore, the 20 nm

features are approaching the minimum domain size limit the cylindrical poly(styrene-b-methyl methacrylate) can achieve.

Diblock copolymer thin films are polycrystalline. Figure 1.10 is a SEM image of the polycrystalline order found with the poly(styrene-b-methyl methacrylate) cylindrical morphology described in the previous paragraph. Within each polymer crystal,

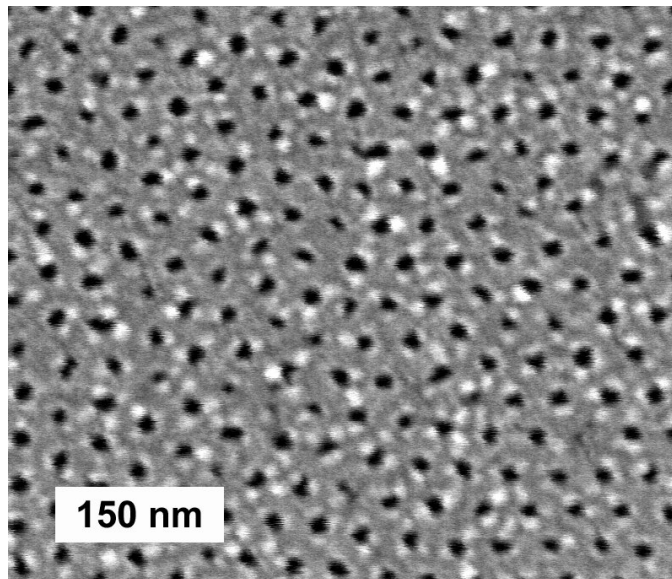


Figure 1.10 SEM image of self-assembled poly(styrene-b-methyl methacrylate) diblock copolymer thin film (30 % methyl methacrylate, 70 % styrene,  $M_n = 67,000$ ) after the cylinders were selectively removed using glacial acetic acid and the voids are seen as dark circles. The majority of the surface has hexagonal closed pack void order interrupted by crystal grain boundaries.

the minority phases also have crystal like order. For example, each minority phase is a point forming an overall hexagonal closed pack structure. Physically confining a single polymer crystal in a horizontal orientation is known as graphoepitaxy [56,57]. Spherical morphology diblock copolymer thin films having continuous single crystals up to 5  $\mu\text{m}$  are reported [57]. Figure 1.11 is a diagram of a spherical morphology diblock copolymer thin film being confined in two manners; the vertical substrate wall limits the crystal and

the mesa area also restricts how far a polymer thin film grows confined by the topography edge. Graphoepitaxy occurs with both types of physical confinement.

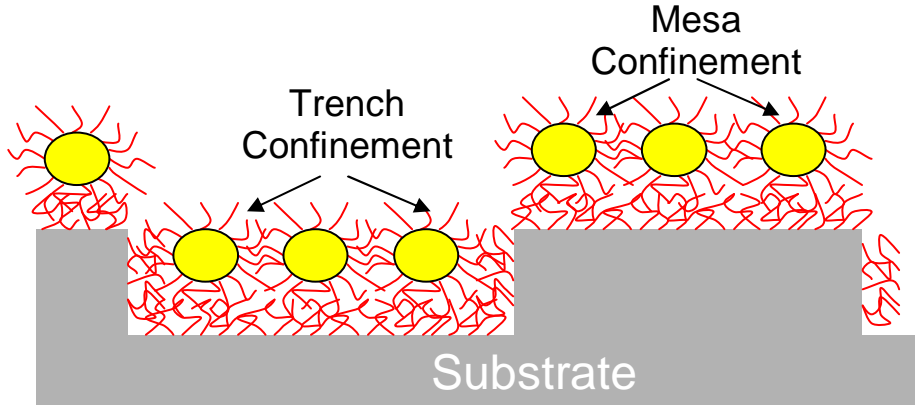


Figure 1.11 Cross section diagram of a substrate having vertical topography and spherical morphology diblock copolymer thin film being confined by the topography after self-assembly [58]. The yellow represents the minority phase spheres and the red lines represent the majority phase.

In a more practical graphoepitaxy procedure, the cylindrical phase poly(styrene-*b*-methyl methacrylate) is directly deposited onto a patterned substrate forming hexagonal closed packed order with cylinders in the bottom of patterned trenches [59].

## 1.6 – CONFINED AREA NANOPARTICLE DEPOSITION

Silicon and Ge selective nanoparticle deposition on crystalline material systems that have been developed for Si/Si(100) [60], Si/Si(111) [61], Ge/Si(100) [62-64], Ge/Si(110) [65], and  $\text{Si}_{1-x}\text{Ge}_x/\text{Si}(100)$  [66]. Typically, the crystalline Si is patterned with a  $\text{SiO}_2$  hard mask where precursor accumulation occurs on the exposed Si and not on the mask. The crystalline deposition surfaces are not suitable for the majority of nanotechnology purposes, since desirable properties such as photoluminescence or Coulomb blockade requires isolating the nanoscale material electrically which is not done

with Si. Secondly, the majority of patterning methods used pattern irregular sized and shaped features. Finally, the etching chemicals or dry etch used are selective to avoid etching the Si(100) or Si(111) surface which has no practical application when dealing with insulators.

Selective deposition between two different amorphous surfaces did not exist previous to the technology developed within the Ekerdt research group [36]. Selectivity depends upon the precursor desorbing from the patterning mask while accumulating on the desired deposition surface. As illustrated in Figures 1.6 and 1.7, SiO<sub>2</sub> is a suitable pattern mask layer for Ge and Si deposition. The configuration that easily enables this selective deposition is creating thin film insulator stacks on a Si(100) substrate with the bottom layer being the deposition surface; and the top layer is the pattern layer or layer which desorbs adatoms into vapor phase as outlined in Figure 1.12. The pattern layer is

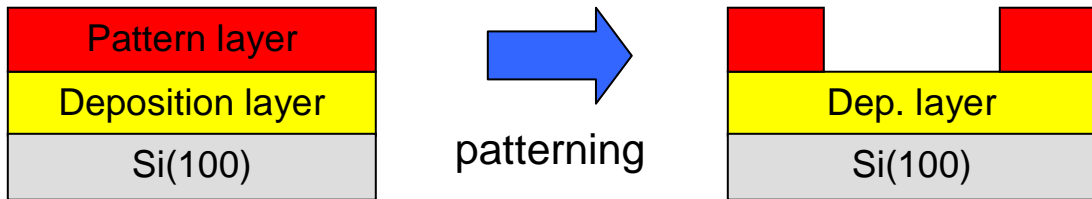


Figure 1.12 The left diagram is a cross section of the insulator stack before patterning. The right diagram is the insulator cross section after a soft mask was used for controlled removal of the pattern layer being ready for CVD.

selectively patterned using a soft mask transferring a pattern with either a wet or dry etch exposing the deposition layer below. Advantages of this system compared to most selective deposition systems is potential nanotechnology integration since insulators isolate electrons while potential feature size and shape is limited exclusively by the soft mask dimensions.

## 1.7 – DISSERTATION OVERVIEW

This dissertation proceeds in a progression from large, unpatterned deposition surfaces or extended surfaces to smaller pattern surfaces, until nanometer scaled features are achieved. The effect of available deposition area and the area scale on nanoparticle deposition are analyzed. Chapter 2 discusses the patterning and nanoparticle deposition apparatus used in this dissertation. Chapter 3 begins with an investigation into the Ge/HfO<sub>2</sub> material system deposition kinetics using extended surfaces. Chapter 3 finishes with the deposition area being reduced having square features with widths ranging 200 nm - 100  $\mu$ m and how various factors as flux and temperature change Ge nanoparticle deposition on confined HfO<sub>2</sub>. Even smaller 20 nm features are investigated in Chapter 4 for the Ge/HfO<sub>2</sub> material system using the diblock copolymer patterning scheme. The technique versatility is demonstrated in Chapter 5 as the selective diblock copolymer patterning is utilized with the Si/Si<sub>3</sub>N<sub>4</sub> material system. Chapter 6 describes the graphoepitaxy process development. Finally, Chapter 7 will discuss continuing projects from this body of work and future research.

The majority of the work presented in this dissertation is already published or soon to be published. Chapter 3 was submitted as an article to a journal in July, 2007. Chapter 4 was divided up into portions and published in both the *Journal of Vacuum Science and Technology B* and in the conference publication *Materials Research Society Symposium Proceedings*. Finally, Chapter 5 is under journal peer review at the time of this dissertation completion.

## REFERENCES

- [1] A. P. Alivisatos, *Science* **271**, 933 (1996).
- [2] H. I. Hanafi, S. Tiwari, and I. Khan, *IEEE Trans. Electron Dev.* **43**, 1553 (1996).
- [3] S. Tiwari, F. Rana, H. Hanafi, A. Hartstein, E. F. Crabbe, and K. Chan, *Appl. Phys. Lett.* **68**, 1377 (1996).
- [4] P. M. Solomon, *Annual Rev. Mater. Sci.* **30**, 681 (2000).
- [5] International Technology Roadmap for Semiconductors; <http://www.itrs.net/>, 2005.
- [6] Y. Q. Wang, J. H. Chen, W. J. Yoo, Y. C. Yeo, S. J. Kim, R. Gupta, Z. Y. L. Tan, D. L. Kwong, A. Y. Du, and N. Balasubramanian, *Appl. Phys. Lett.* **84**, 5407 (2004).
- [7] H. G. Yang, Y. Shi, L. Pu, R. Zhang, B. Shen, P. Han, S. L. Gu, and Y. D. Zheng, *Appl. Surf. Sci.* **224**, 394 (2004).
- [8] M. Vulpio, C. Gerardi, S. Lombardo, G. Ammendola, I. Crupi, T. Rossetti, N. Nastasi, G. Mantarro, and G. Nicotra, in *Gettering and Defect Engineering in Semiconductor Technology* (2002), Vol. 82-84, pp. 663.
- [9] S. Tiwari, J. A. Wahl, H. Silva, F. Rana, and J. J. Welser, *Appl. Phys. A-Mater. Sci. Processing* **71**, 403 (2000).

- [10] I. Crupi, D. Corso, S. Lombardo, C. Gerardi, G. Ammendola, G. Nicotra, C. Spinella, E. Rimini, and M. Melanotte, *Mater. Sci. Eng. C* **23**, 33 (2003).
- [11] B.G. Streetman and S.K. Banerjee, in *Solid State Electronic Devices* (Prentice Hall, Upper Saddle River, NJ, 2000).
- [12] S. Tiwari, F. Rana, K. Chan, L. Shi, and H. Hanafi, *Appl. Phys. Lett.* **69**, 1232 (1996).
- [13] L. Perniola, B. D. Salvo, G. Ghibaudo, A. F. Para, G. Pananakakis, T. Baron, and S. Lombardo, *Solid-State Electron.* **47**, 1637 (2003).
- [14] D. W. Kim, T. Kim, and S. K. Banerjee, *IEEE Trans. Electron Dev.* **50**, 1823 (2003).
- [15] G. Ammendola, M. Vulpio, M. Bileci, N. Nastasi, C. Gerardi, G. Renna, I. Crupi, G. Nicotra, and S. Lombardo, *J. Vac. Sci. Tech. B* **20**, 2075 (2002).
- [16] S. Lombardo, B. De Salvo, C. Gerardi, and T. Baron, *Microelec. Eng.* **72**, 388 (2004).
- [17] T. H. Ng, V. Ho, L. W. Teo, M. S. Tay, B. H. Koh, W. K. Chim, W. K. Choi, A. Y. Du, and C. H. Tung, *Thin Solid Films* **462-63**, 46 (2004).
- [18] Y. Z. Hu, D. J. Diehl, C. Y. Zhao, C. L. Wang, Q. Liu, E. A. Irene, K. N. Christensen, D. Venable, and D. M. Maher, *J. Vac. Sci. Tech. B* **14**, 744 (1996).
- [19] B. Gong, S. Jo, G. Hess, P. Parkinson, and J. G. Ekerdt, *J. Vac. Sci. Tech. A* **16**, 1473 (1998).

- [20] J.N. Israelachvili, *Intermolecular and Surface Forces*. (Academic Press, San Diego, CA, 1992).
- [21] P. Van Der Voort E.F. Vansant, K.C. Vrancken, *Characterization and Chemical Modification of the Silica Surface*. (Elsevier, Amsterdam, 1995).
- [22] T. Baron, F. Mazen, C. Busseret, A. Souifi, P. Mur, F. Fournel, M. N. Semeria, H. Moriceau, B. Aspard, and P. Gentile, *Microelectron. Eng.* **61-2**, 511 (2002).
- [23] C. Basa, Y. Z. Hu, M. Tinani, and E. A. Irene, *J. Vac. Sci. Technol. A-Vac. Surf. Films* **16**, 3223 (1998).
- [24] F. Mazen, L. Mollard, T. Baron, S. Decossas, and J. M. Hartmann, *Microelec. Eng.* **73-74**, 632 (2004).
- [25] S. Miyazaki, Y. Hamamoto, E. Yoshida, M. Ikeda, and M. Hirose, *Thin Solid Films* **369**, 55 (2000).
- [26] L. Andersohn, T. Berke, U. Kohler, and B. Voigtlander, *J. Vac. Sci. Technol. A-Vac. Surf. Films* **14**, 312 (1996).
- [27] D. Kandel, *Phys. Rev. Lett.* **78**, 499 (1997).
- [28] J.A. Venables, *Phil. Mag.* **17**, 697 (1973).
- [29] H. Brune, *Surf. Sci. Rep.* **31**, 121 (1998).

- [30] J. A. Venables, Surf. Sci. **300**, 798 (1994).
- [31] J. A. Venables, G. D. T. Spiller, and M. Hanbucken, Rep. Prog. Phys. **47**, 399 (1984).
- [32] H. Rauscher, J. Braun, and R. J. Behm, Phys. Rev. Lett. **96**, 116101 (2006).
- [33] Q. M. Li, J.L. Krauss, S. Hersee, and S. M. Han, J. Phys. Chem. C **111**, 779 (2006).
- [34] J. H. Zhu, W. T. Leach, S. K. Stanley, J. G. Ekerdt, and X. M. Yan, J. Appl. Phys. **92**, 4695 (2002).
- [35] W. T. Leach, J. H. Zhu, and J. G. Ekerdt, J. Cryst. Growth **243**, 30 (2002).
- [36] S.K. Stanley, S.V. Joshi, S.K. Banerjee, and J.G. Ekerdt, J. Vac. Sci. Tech. A **24**, 78 (2006).
- [37] H. Matsumura, Jpn. J. Appl. Phys. pt. 1 **37**, 3175 (1998).
- [38] M. S. Mason, J. K. Holt, and H. A. Atwater, Thin Solid Films **458**, 67 (2004).
- [39] W. T. Leach, J. H. Zhu, and J. G. Ekerdt, J. Cryst. Growth **240**, 415 (2002).
- [40] D. C. Streit and F. G. Allen, J. Appl. Phys. **61**, 2894 (1987).

- [41] S.K. Stanley, S.S. Coffee, and J.G. Ekerdt, App. Surf. Sci. **252**, 878 (2005).
- [42] Y. Lin, A. Boker, J. B. He, K. Sill, H. Q. Xiang, C. Abetz, X. F. Li, J. Wang, T. Emrick, S. Long, Q. Wang, A. Balazs, and T. P. Russell, Nature **434**, 55 (2005).
- [43] J. Peng, Y. Xuan, H. F. Wang, Y. M. Yang, B. Y. Li, and Y. C. Han, J. Chem. Phys. **120**, 11163 (2004).
- [44] G. Kastle, H. G. Boyen, F. Weigl, G. Lengl, T. Herzog, P. Ziemann, S. Riethmuller, O. Mayer, C. Hartmann, J. P. Spatz, M. Moller, M. Ozawa, F. Banhart, M. G. Garnier, and P. Oelhafen, Adv. Funct. Mater. **13**, 853 (2003).
- [45] P. Mansky, C. K. Harrison, P. M. Chaikin, R. A. Register, and N. Yao, Appl. Phys. Lett. **68**, 2586 (1996).
- [46] C. Harrison, M. Park, P. M. Chaikin, R. A. Register, and D. H. Adamson, J. Vac. Sci. Tech. B **16**, 544 (1998).
- [47] C. L. Zhang, T. Xu, D. Butterfield, M. J. Misner, D. Y. Ryu, T. Emrick, and T. P. Russell, Nano Letters **5**, 357 (2005).
- [48] I.W. Harnley, *The Physics of Block Copolymers*. (Oxford University Press, Oxford, UK, 1998).
- [49] F.M.A Barton, *CRC handbook of Polymer-Liquid Interaction Parameters and Solubility Parameters*. (CRC Press, Boca Raton, FL, 1990).

- [50] M. Park, C. Harrison, P. M. Chaikin, R. A. Register, and D. H. Adamson, *Science* **276**, 1401 (1997).
- [51] K. Asakawa and T. Hiraoka, *Jpn. J. Appl. Phys. pt 1* **41**, 6112 (2002).
- [52] K. W. Guarini, C. T. Black, Y. Zhang, H. Kim, E. M. Sikorski, and I. V. Babich, *J. Vac. Sci. Tech. B* **20**, 2788 (2002).
- [53] C. T. Black, K. W. Guarini, K. R. Milkove, S. M. Baker, T. P. Russell, and M. T. Tuominen, *Appl. Phys. Lett.* **79**, 409 (2001).
- [54] P. Mansky, Y. Liu, E. Huang, T. P. Russell, and C. Hawker, *Science* **275**, 1458 (1997).
- [55] K. W. Guarini, C. T. Black, and S. H. I. Yeuing, *Adv. Mater.* **14**, 1290 (2002).
- [56] J. Y. Cheng, C. A. Ross, E. L. Thomas, H. I. Smith, and G. J. Vancso, *Appl. Phys. Lett.* **81**, 3657 (2002).
- [57] R. A. Segalman, A. Hexemer, R. C. Hayward, and E. J. Kramer, *Macromolecules* **36**, 3272 (2003).
- [58] R. A. Segalman, K. E. Schaefer, G. H. Fredrickson, E. J. Kramer, and S. Magonov, *Macromolecules* **36**, 4498 (2003).
- [59] C.T. Black and O. Bezencenet, *IEEE Trans. Nanotech.* **3**, 412 (2004).

- [60] M. Shibata, Y. Nitta, K. Fujita, and M. Ichikawa, **61**, 7499 (2000).
- [61] M. Shibata, Y. Nitta, K. Fujita, and M. Ichikawa, Appl. Phys. Lett. **73**, 2179 (1998).
- [62] Y. Nitta, M. Shibata, K. Fujita, and M. Ichikawa, Surf. Sci. **496**, L7 (2002).
- [63] Y. Nitta, M. Shibata, K. Fujita, and M. Ichikawa, Surf. Sci. **462**, L587 (2000).
- [64] J. R. Heath, R. S. Williams, J. J. Shiang, S. J. Wind, J. Chu, C. Demic, W. Chen, C. L. Stanis, and J. J. Bucchignano, **100**, 3144 (1996).
- [65] J. D. Weil, X. Deng, and M. Krishnamurthy, J. Appl. Phys. **83**, 212 (1998).
- [66] D. Cha, M. Ogawa, C. Chen, S. Kim, J. Lee, K. L. Wang, J. Y. Wang, and T. P. Russell, J. Cryst. Growth **301**, 833 (2007).

## Chapter 2 – Experimental Methods

### 2.1 CHEMICAL VAPOR DEPOSITION

The main deposition apparatus in this dissertation is a multi chamber ultra-high-vacuum CVD (UHVCVD) arrangement previously described [1,2]. The system handles wafer samples  $1.6 \times 1.6$  cm in size by mounting wafer pieces onto hollow, round molybdenum pucks. The samples are admitted to the apparatus via a load lock after 10 min at low vacuum ( $\sim 10^{-3}$  Torr) in the load lock; other chambers are accessed through use of a central transfer chamber held constantly at  $\sim 10^{-7}$  Torr. Puck movement occurs when the transfer arm in the transfer chamber extends, grabbing a puck with a hook. The transfer arm then moves the puck in a radial direction within the transfer chamber accessing other attached chambers.

The deposition chamber held at  $\sim 10^{-10}$  Torr is reserved for nanoparticle CVD and HWCVD. Available hydride gases in the deposition chamber for Si deposition are silane ( $\text{SiH}_4$ ) and disilane ( $\text{Si}_2\text{H}_6$ ). The equivalent Ge source is germane ( $\text{GeH}_4$ ). Infrared sample heating is performed on the wafer backside using a 300 W incandescent light bulb with a portion of the glass housing removed. The sample temperature can be heated from room temperature up to 1025 K. In line-of-sight of the sample is a second incandescent light bulb with a portion of the glass removed exposing the tungsten filament for the purpose of radical generation used in room temperature physical vapor deposition and higher temperature HWCVD.

The second main chamber attached to the apparatus, the analytical chamber, held at  $\sim 10^{-10}$  Torr, has several *in situ* analytical tools. A ThermoVG CLAM2 X-ray photoelectron spectroscopy (XPS) system generates Al and Mg  $K_\alpha$  X-rays (Al is used for

all of the XPS data in this dissertation) and collects the photoelectron signals with a hemispherical analyzer. Ion scattering spectroscopy (ISS) uses a  $\text{He}^+$  ion source while utilizing the same analyzer as the XPS system. Finally, the analytical chamber has a Thermo Electron VG Smart IQ<sup>+</sup> series quadrupole mass spectrometer allowing background gas analysis and temperature programmed desorption. One more chamber, a quartz tube furnace, held at  $\sim 10^{-7}$  Torr is attached to the transfer chamber enabling sample annealing in vacuum up to 1275 K.

## 2.2 ELECTRON BEAM LITHOGRAPHY

The patterning technique known as electron beam lithography (EBL) uses an electron beam to physically alter a polymer thin film. EBL occurs within a vacuum chamber with a specially equipped scanning electron microscope (SEM) having the electron gun and detector. The SEM serves as an *in situ* sample alignment device, while the electron gun also serves as the patterning electron beam. Figure 2.1 is a diagram of an EBL patterning equipment set up. The electron beam exposes the polymer thin film mask as the sample stage moves via computer control. The internal SEM acts as a sample alignment mechanism. Pattern dimensions are programmed into a computer that moves the stage underneath the sample. The specified distances are moved by the stage as a highly focused electron beam moves across the sample surface and transfers the pattern into the polymer. The EBL used in our experiments is a Raith 50 located in the Center for Nano Molecular Science and Technology on campus having a minimal resolvable feature size of  $\sim 80$  nm.

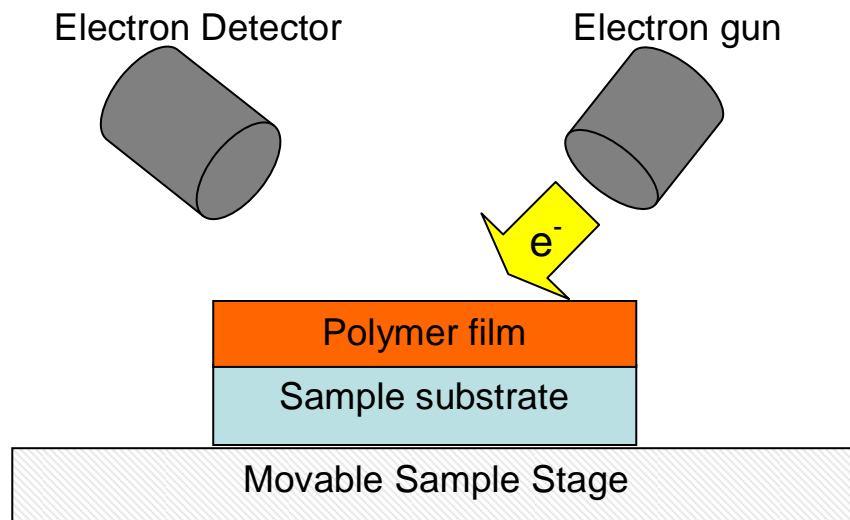


Figure 2.1 Diagram of EBL equipment set up within a vacuum chamber.

The positive EBL resist has electron beam-exposed portions of the film eventually removed leaving a positive image of the desired pattern. Poly(methyl methacrylate) [PMMA] is a typical positive resist and the number molecular weight used in our experiments was  $M_n = 960,000$ . The resist was made within our laboratory by diluting 3% PMMA by weight within anisole. The resist was then spin-coated onto a hexamethyldisilazane (HMDS) treated sample and then baked at 150 °C for minimum 1 h. The 75 nm thick deposited PMMA film is sufficient for the reactive ion etch to etch 12.5 nm of SiO<sub>2</sub> without removing the resist in our amorphous substrate patterning technique. A 220  $\mu\text{C}/\text{cm}^2$  electron beam exposure was used and this was sufficient to degrade the PMMA; degraded portions are later selectively removed using a 1:3 methyl isobutyl ketone/isopropyl alcohol developer. This method was used to pattern features 200 nm to 100  $\mu\text{m}$  in size.

### 2.3 DIBLOCK COPOLYMER PATTERNING

Nanoscale patterning using a thin film poly(styrene-*b*-methyl methacrylate) diblock copolymer film is a well-characterized process in literature [3,4]. We adapted the process directly from the published literature using equipment located in the Willson research group at the University of Texas at Austin and the general user facility located on campus at the Center for Nano and Molecular Science and Technology (CNT). The Willson group has spin coaters and an ellipsometer, while the CNT has a vacuum oven where the actual self-assembly process occurred. The polymers were purchased from Polymer Source, Inc. based in Dorval (Montreal), Quebec, Canada.

The diblock copolymer mask patterning works for our purposes only if the cylinders are oriented perpendicular with the substrate and this is accomplished through proper copolymer interaction with the surface and vertical confinement. Energetic neutrality between the copolymer styrene and methyl methacrylate species with the silica surface is accomplished by forming a monolayer of chemically attached random copolymer (60% styrene and 40% methyl methacrylate,  $M_n = 8,900$ ) [5,6]. Random copolymer is spin coated from a 1% dilute solution in toluene onto the silica surface at a thickness of ~60 nm. The polymer film is annealed under vacuum at ~160 °C for a minimum 48 h allowing the polymer strands to diffuse. The random copolymer used in these experiments have a functionalized hydroxyl group (-OH) at one end of each polymer chain and the diffusion causes the hydroxyl groups to physically contact the silica surface. The hydroxyl groups then chemically interact with the silica surface in a condensation reaction forming an attached random copolymer monolayer. After the anneal, a gentle toluene rinse removes unattached polymer chains leaving the attached random copolymer monolayer behind. Next, the poly(styrene-*b*-methyl methacrylate) diblock copolymer (70 % styrene, 30 % methyl methacrylate,  $M_n = 67,100$ ) is spin coated

from a 1.1% dilute anisole solution to a thickness of  $37 \pm 4$  nm. The thickness is monitored post deposition using a J.A. Woollam M-2000 ellipsometer and proper self-assembly requires the thickness tolerance near 37 nm is achieved. The samples are then further annealed at 180 °C for another 4 h where self-assembly occurs. Poly(methyl methacrylate) cylinders are accessible for selective removal from the film using a 15 min glacial acetic acid bath leaving a polystyrene template with 20 nm pores having direct access to the silica below.

## **2.4 GRAPHOEPI TAXY**

Work was started on dual-level patterning using our selective deposition nanoparticle process utilizing the diblock copolymer process in graphoeptaxy. The poly(styrene-*b*-methyl methacrylate) thin film system forms crystalline domains up to 600 nm in width [7]. Physically confining portions of the copolymer thin films within physical barriers allows compete crystallization of the portion. The minority poly(methyl methacrylate) cylinders then form hexagonal closed packed organization. Processing the diblock copolymer films is same as described in the previous section except the diblock copolymer film is slightly thinner at ~34 nm thick. Figure 2.2 is an SEM image of graphoeptaxy within a 250 nm box and 250 nm wide parallelograms. The step height of the patterning plasma enhanced CVD silica on a Si(100) wafer is ~60 nm. The features were patterned using EBL performed at Sandia National Laboratories in the Center for Integrated Nanotechnologies by collaboration with Aaron Gin. The graphoeptaxy

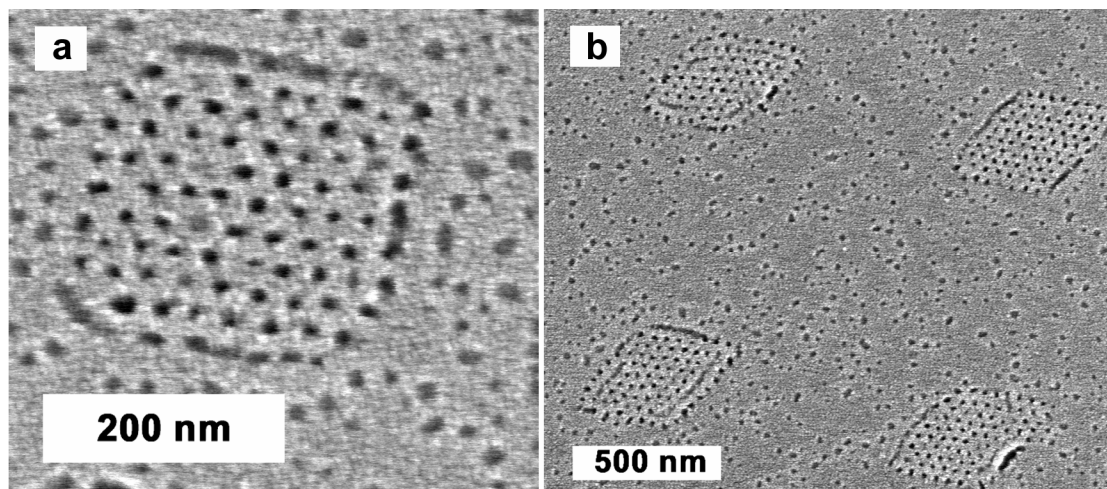


Figure 2.2 a) Graphoepitaxy using poly(styrene-*b*-methyl methacrylate) thin films within ~60 nm deep square box patterned within plasma enhanced CVD deposited silica on a Si(100) substrate. The 250 nm wide box was patterned using EBL. The dark spots are where the cylinders were removed from. b) Similar graphoepitaxy as Part a) except the features are ~250 nm wide parallelograms. Note: perfect order is not achieved in all of the features.

process was not used in dual-level patterning of nanoparticles because time ran out for proper process development incorporation into the selective deposition process.

## REFERENCES

- [1] W. T. Leach, J. H. Zhu, and J. G. Ekerdt, *J. Cryst. Growth* **243**, 30 (2002).
- [2] W. T. Leach, J. H. Zhu, and J. G. Ekerdt, *J. Cryst. Growth* **240**, 415 (2002).
- [3] K. W. Guarini, C. T. Black, Y. Zhang, H. Kim, E. M. Sikorski, and I. V. Babich, *J. Vac. Sci. Tech. B* **20**, 2788 (2002).

- [4] K. W. Guarini, C. T. Black, and S. H. I. Yeung, *Adv. Mater.* **14**, 1290 (2002).
- [5] P. Mansky, Y. Liu, E. Huang, T. P. Russell, and C. Hawker, *Science* **275**, 1458 (1997).
- [6] P. Mansky, T. P. Russell, C. J. Hawker, M. Pitsikalis, and J. Mays, *Macromolecules* **30**, 6810 (1997).
- [7] C.T. Black and O. Bezencenet, *IEEE Trans. Nanotech.* **3**, 412 (2004).

## Chapter 3 – Investigation of Volmer-Weber growth mode kinetics for germanium nanoparticles on hafnia

### 3.1 INTRODUCTION

Germanium nanocrystal-based flash memory [1-4] has been successfully fabricated and tested as a potential low power memory device. Chemical vapor deposition (CVD) is a desired nanoparticle fabrication method for flash memory devices due to the process being well characterized within the integrated chip industry [5]. CVD on the amorphous insulator substrates does not deposit nanoparticles with uniform size and uniform lateral placement enabling optimal flash memory device operation [6]. Memory cell dimensions decrease with the gate length, which is projected to be 45 nm in 2010 [7]. The discrete nanoparticle charge storage units are deposited on these gates, meaning the number of particles per device will also be decreasing with gate size. Nanoparticle placement and tight control on the number of nanoparticles within the confined areas becomes even of greater importance since fewer nanoparticles will be used per device.

Mean-field nucleation theory relates the density of stable islands/nanoparticles,  $N_{SAT}$ , to the incident flux,  $F$ , and temperature [8-10]. Nucleation depends on the ability to form stable adatom groupings upon a nucleation site. The critical cluster size corresponds to the number of adatoms,  $i^*$ , required for the formation of a stable cluster. Nucleation occurs when an additional adatom is added to a critical cluster producing a particle of size  $i^*+1$ , which is assumed to be stable against decomposition. Knowledge of the material system dependent critical cluster size is vital to control the resultant nanoparticle density, since the rate of stable nuclei formation is dependent upon the average surface adatom concentration,  $\bar{n}$ , to the  $i^*+1$  power, i.e. rate  $\propto \bar{n}^{(i^*+1)}$  [11].

Critical cluster formation through adatom diffusion requires the intersection of enough diffusing adatoms to form  $i^*$ -sized clusters and adatoms need enough energy to overcome the critical cluster formation energetic barrier,  $E^*$  [11].

The majority of deposition kinetic studies have been performed using molecular beam epitaxy (MBE) and have followed Stranski-Krastanov growth mode systems in which a wetting layer forms first on a crystalline substrate followed by island growth [8,9,12,13]. Stranski-Krastanov systems typically have  $i^*$  values consisting of several adatoms, for example, Ge/Si(111) [12] is 5 and Si/Si(111) [13] is 5-7. Volmer-Weber growth mode typically occurs with heterogeneous systems where the deposition material does not wet the surface resulting directly in islands. Nucleation sites, such as found on silica, are randomly placed defects [14] on the surface leading to a higher degree of random nucleation compared with Stranski-Krastanov growth. The  $i^*$  value reported for Volmer-Weber mode systems are zero for Ge/SiO<sub>2</sub> [15] and was estimated as 1 for Si/SiO<sub>2</sub> [9]. Nothing to date has been reported concerning  $E^*$  or  $i^*$  for the Ge/HfO<sub>2</sub> system.

This chapter investigates kinetics of the Ge/HfO<sub>2</sub> material system utilizing hot wire chemical vapor deposition (HWCVD) [16,17]. Hot wire CVD allows greater control of the incident deposition flux to the surface, overcoming the limitations of precursor adsorption limited thermal CVD. The critical cluster size is reported along with the critical cluster activation energy of formation upon extended (unpatterned) HfO<sub>2</sub> surfaces. Finally, the nanoparticle nucleation and growth behavior is examined as the HfO<sub>2</sub> deposition surface dimensions are confined within features ranging from 200 nm to 100  $\mu$ m.

### 3.2 EXPERIMENTAL PROCEDURE AND METHODS

Sematech Inc. provided the 12.5 nm CVD SiO<sub>2</sub>/10 nm atomic layer deposition HfO<sub>2</sub> grown stack structures on 8-in p-doped Si(100) wafers. After dicing into 1.6 × 1.6 cm sized portions, samples were cleaned with an acetone/ethanol/deionized (DI) water rinse, then dried with compressed nitrogen. The extended surface samples were further cleaned for 5 min in a 6:2:1 sulfuric acid/DI water/hydrogen peroxide pihrana solution followed with a quick DI water rinse. The top SiO<sub>2</sub> layer was then removed using a 30 s 2% HF etch and a quick DI water rinse removing the HF. Another 5 min pihrana bath cleaning and DI water rinse was then performed to the samples.

The 1.6 × 1.6 cm sized samples began the patterning process with an acetone/ethanol rinse followed with a 5 min sonication in an ethanol bath. After a compressed nitrogen drying, hexamethyldisilazane as an adhesion layer was spin coated onto the silica surface and annealed on a hot plate 3 min at 90° C. Poly(methyl methacrylate) ( $M_n=960,000$ ) diluted 3% in anisole was then spin coated onto the treated silica surface under conditions that produce a ~75 nm thick film. Samples were annealed at 150°C for 1 h to assure the smoothness of the polymer film and adhesion to the silica. Individual samples were loaded into a Raith 50 Electron Beam Lithography (EBL) system where the pattern was transferred into the polymer film with an electron beam exposure of 220  $\mu\text{C}/\text{cm}^2$ . The degraded, exposed film was then selectively removed using a 1 min bath in 1:3 methyl isobutyl keytone/isopropyl alcohol developer. Reactive ion etch (RIE) using a CHF<sub>3</sub>/O<sub>2</sub> chemistry at 200 W and 15 mTorr transferred the pattern into and through the silica layer. The RIE pattern did not transfer into the HfO<sub>2</sub> layer due to the formation of nonvolatile HfF<sub>x</sub>, Hf<sub>x</sub>O<sub>y</sub>, and C<sub>x</sub>F<sub>y</sub> byproducts [18], which behave as an etch stop. Removing the soft polymer mask was performed using a 5 min O<sub>2</sub> ash at 40

W. The patterned samples were further cleaned for 5 min in the piranha solution followed with a quick DI water rinse. To realize complete removal of SiO<sub>2</sub> in the etched areas, the samples were then subjected to a 2 s 1% HF etch followed with a quick DI water rinse. Another 5 min piranha bath cleaning and DI water rinse gave the exposed HfO<sub>2</sub> surface similar treatment as the extended samples.

The etched sample squares were then loaded into the ultra-high-vacuum (UHV) CVD system described in Chapter 2 [19] and annealed for 15 min at 750 K to degas the surface. The temperature was adjusted to the range of 700-775 K before GeH<sub>4</sub> (diluted 4% in He, from Voltaix Inc.) with a partial pressure in the range of  $2.0 \times 10^{-8}$  to  $8 \times 10^{-7}$  Torr was admitted to the deposition chamber. The sample was placed ~3 cm from a tungsten cracking filament supplied with 4 amps current (>1500°C) resulting in a flux range of 0.06 to 4.2 monolayer/min (1 ML =  $6.3 \times 10^{14}$  atoms/cm<sup>2</sup>). HWCVD occurs when GeH<sub>4</sub> molecules decompose on the hot filament with GeH<sub>x</sub> radicals desorbing and depositing on the heated sample surface. Fluxes were calibrated on thermally grown SiO<sub>2</sub> at room temperature, a condition that leads to amorphous Ge film deposition [20]; X-ray photoelectron spectroscopy (XPS) peak attenuation for the Si 2p oxide at 103.5 eV was used to establish the Ge film thickness. The Ge flux is a linear function of GeH<sub>4</sub> partial pressure.

Upon removal from the system, the samples were coated with ~10 nm of Pd/Au to prevent surface charging under analysis in a Hitachi S-4500 field emission scanning electron microscope (SEM). Sputter coating onto blanket wafers was confirmed not to create features that could be interpreted as nanoparticles. Particle densities are determined by counting particles after digitally enhancing the SEM images. Nanoparticles less than ~5 nm in diameter are difficult to resolve.

### 3.3 RESULTS

Background thermal CVD during HWCVD [16] potentially adds adatoms into the system increasing the actual flux to an unknown value. To test for possible thermal CVD, HfO<sub>2</sub> samples were exposed to  $1.2 \times 10^{-7}$  Torr GeH<sub>4</sub> for 23.3 min at 700 and 775 K to simulate GeH<sub>4</sub> exposure that a sample would experience during 14 ML HWCVD. No Ge species were detected after the exposure using the Ge 2p<sub>3/2</sub> peak indicating thermal CVD would not occur from background GeH<sub>4</sub> during HWCVD if the filament were turned off. We conclude Ge addition to the HfO<sub>2</sub> surface during HWCVD is from the tungsten cracking filament.

Nucleation increases have been associated with ion damage from RIE processing [21,22]. Hafnia samples were exposed to the same RIE treatments used to process patterned samples, and then subjected to  $2 \times 10^{-4}$  Torr GeH<sub>4</sub> partial pressure (480,000 Langmuir) at 850 K for 40 min. These CVD conditions have been shown to produce  $2 \times 10^{10}$  cm<sup>-2</sup>, 5-20 nm diameter Ge particles on HfO<sub>2</sub> [23]. As a control sample, the SiO<sub>2</sub> mask was removed with a 2 % HF bath for 30 s, rinsed with DI water, given a 10 min piranha bath, and finally received a DI water rinse. The second HfO<sub>2</sub> sample had the silica film removed through the RIE process and exposed to the O<sub>2</sub> ash. After the RIE, the second sample was given a 10 min piranha bath and a DI water rinse. CVD resulted in a particle density of  $2 \times 10^{10}$  cm<sup>-2</sup> on both samples illustrating RIE exposure and chemical rinsing did not leave noticeable residual ion damage.

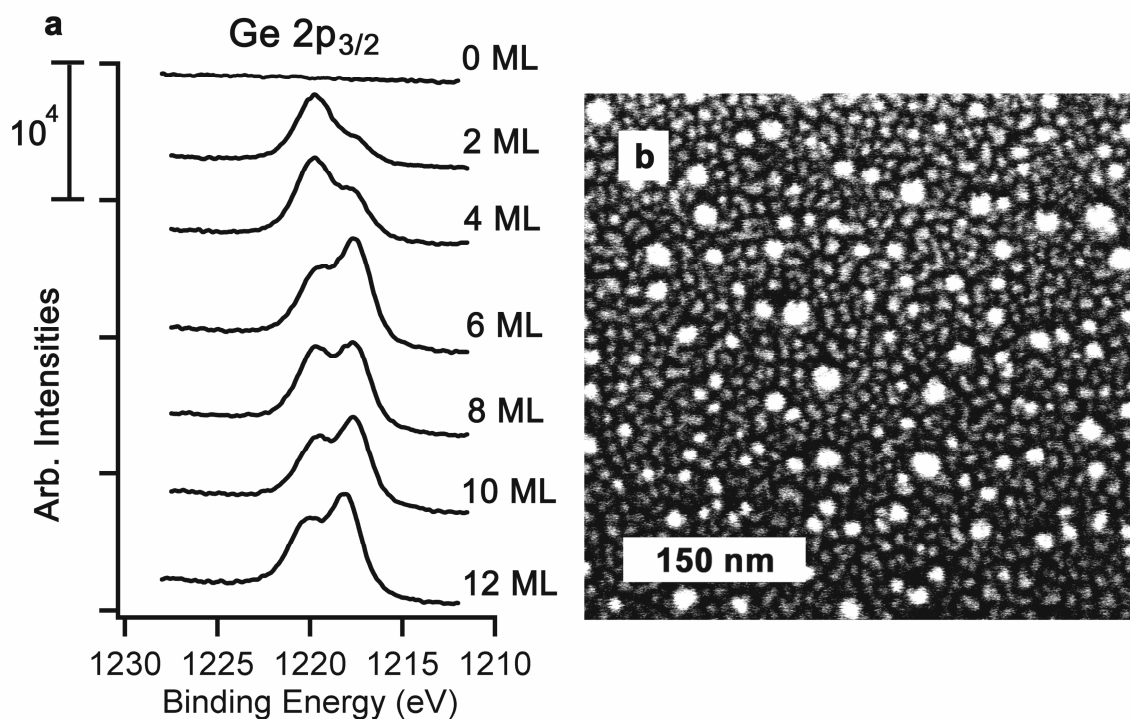


Figure 3.1 a.) Ge 2p<sub>3/2</sub> XPS peak following the evolution of GeO<sub>x</sub> (1220 eV) and Ge<sup>0</sup> (1217 eV) after Ge deposition on extended hafnia surfaces at 0.6 ML/min and 750 K. The top trace is the baseline signal. b) SEM image of HWCVD Ge nanoparticles at 775 K, 0.6 ML/min flux, and 10 ML exposure. The nanoparticles are the bright spots and range from 5-20 nm in diameter. The particle density is  $1 \times 10^{11} \text{ cm}^{-2}$ .

The XPS Ge 2p<sub>3/2</sub> peak data shown in Figure 3.1a follow HWCVD Ge deposition on extended HfO<sub>2</sub> surfaces at a flux of 0.6 ML/min and 750 K as the exposure is increased by 2 ML increments up to 12 ML. Initially, the GeO<sub>x</sub> signal (1220 eV) dominates with some metallic Ge<sup>0</sup> (1217 eV) formed at 2 ML. The relative percentage of metallic Ge<sup>0</sup> increased for longer exposures. The peak area for GeO<sub>x</sub> remained relatively constant. Figure 3.1b is a representative SEM image of HWCVD Ge nanoparticles at 775 K, 0.6 ML/min, and 10 ML total exposure. Figure 3.2a plots nanoparticle density versus exposure at 0.6 and 2.1 ML/min deposition fluxes while the temperature is held at 750 K.

The saturation density or maximum density is achieved above 6 ML exposure. Saturation density is a function surface coverage [11,13]. Particle densities deposited with exposures above 6 ML do not decrease, indicating coalescence is minimal. Furthermore, the flux does not influence density, thus we conclude an 8 ML exposure is sufficient to deposit the saturation density at all deposition fluxes and temperatures. We believe the lower density deposited for 0.6 ML/min compared with 2.1 ML/min, when the exposure is less than 6 ML, is a result of the metallic Ge<sup>0</sup> desorption from the HfO<sub>2</sub> surface and is discussed later.

Figure 3.3a plots the HWCVD nanoparticle saturation density versus deposition flux at 750 and 775 K after 8 ML exposure. The particle density is constant at  $2 \times 10^{11} \text{ cm}^{-2}$  for 0.6, 2.1 and 4.2 ML/min fluxes. At 775 K, upon decreasing the flux to 0.1 ML/min, a 50% density reduction occurs to  $6 \times 10^{10} \text{ cm}^{-2}$ . The 775 K density is even lower at  $2 \times 10^{10} \text{ cm}^{-2}$  when the flux is reduced further to 0.06 ML/min. The 750 K particle density has a similar decrease between 0.1 and 0.06 ML/min fluxes at  $2 \times 10^{11}$  and  $3 \times 10^{10} \text{ cm}^{-2}$ , respectively. Figure 3.3b plots particle saturation density versus deposition flux at 700 and 725 K after 8 ML exposure. Particle densities deposited at 2.1 and 4.2 ML/min fluxes were averaged to examine the weak temperature influence on particle density at 8 ML exposure in Figure 3.2b. Particle density decreases linearly as temperature increases on extended HfO<sub>2</sub> surfaces.

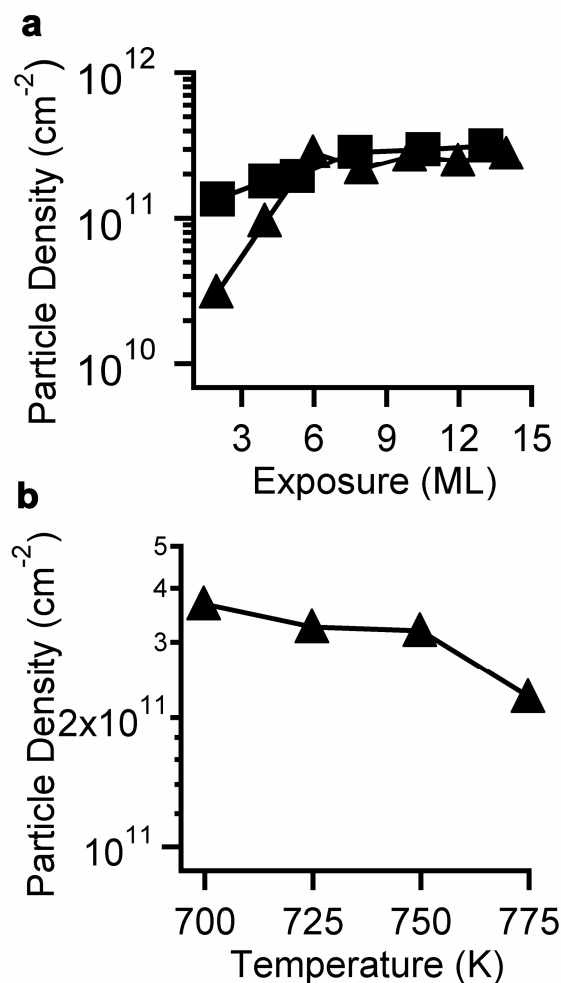


Figure 3.2 a) Particle density versus HWCVD Ge exposure on extended  $\text{HfO}_2$  surfaces, 750 K, 0.6 ( $\blacktriangle$ ) and 2.1 ( $\blacksquare$ ) ML/min fluxes. b) Average Ge particle density versus temperature on extended  $\text{HfO}_2$  surfaces. The data points are averages of the 2.1, and 4.2 ML/min fluxes for 8 ML exposure.

Depositions having long thermal exposure time experience Ge desorbing from the  $\text{HfO}_2$  surface during nanoparticle growth. To simulate the thermal exposure the samples receive over long time periods, a  $\text{HfO}_2$  sample was subjected to a 1 ML Ge exposure at 2.1 ML/min followed with a 10 min 775 K anneal repeating this exposure and anneal cycle eight times. The complete 79 min deposition resulted in a  $4 \times 10^{10} \text{ cm}^{-2}$  particle

density, which is closer to the  $6 \times 10^{10} \text{ cm}^{-2}$  density from a 0.1 ML/min, 775 K (80 min) deposition and not to the  $2 \times 10^{11} \text{ cm}^{-2}$  obtained from a 2.1 ML/min, 775 K deposition (4 min).

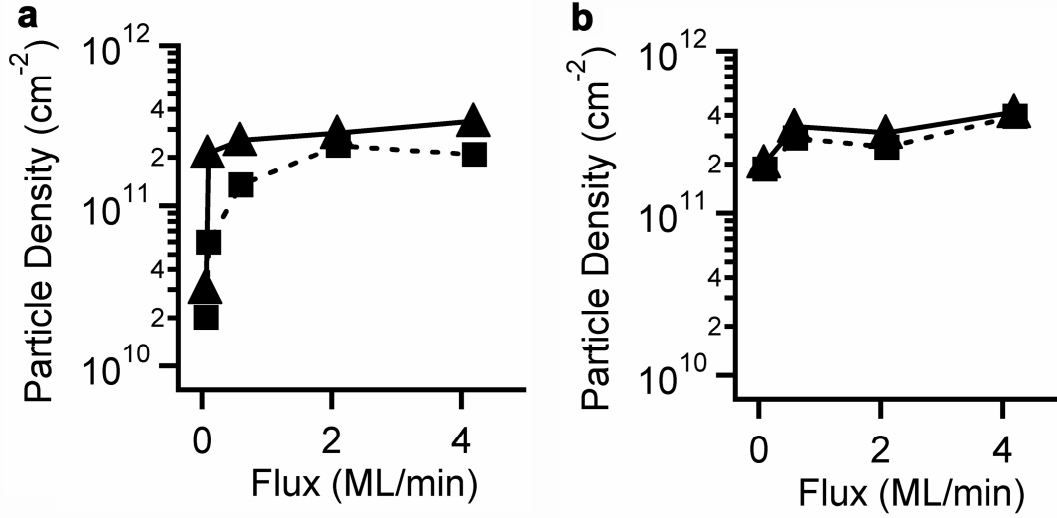


Figure 3.3 a) Saturation Ge particle density versus deposition flux at 750 (▲) and 775 (■) K on extended  $\text{HfO}_2$  surfaces for 8 ML exposure. b) Saturation Ge particle density (8 ML) versus deposition flux at 700 (▲) and 725 (■) K on extended  $\text{HfO}_2$  surfaces for 8 ML exposure.

The soft EBL polymer mask is seen in the optical microscope image presented in Figure 3.4a. Scanning electron microscopy HWCVD nanoparticle growth data were taken from square features with widths of 200 nm, 600 nm, 1  $\mu\text{m}$ , 3  $\mu\text{m}$ , 5  $\mu\text{m}$ , 10  $\mu\text{m}$ , and 100  $\mu\text{m}$ . Figure 3.4b is a SEM image of a 200 nm wide box after an 8 ML exposure at 0.1 ML/min flux and 775 K. Figure 3.5a shows particle density versus feature size for the four extreme flux and temperature combinations in our experimental grid, 0.1 and 4.2 ML/min combined with 700 and 775 K. Continuous Ge films grew over the  $\text{HfO}_2$  surface for the two smallest features (200 nm and 600 nm) on the 4.2 ML/min/700 K sample and are not displayed on the plot. At the extreme conditions in our grid, nanoparticle density is not influenced by the feature size with the exception of smallest

feature (200 nm) displaying a slight density decrease. The confined area is more sensitive at 775 K compared to lower temperatures. Nanoparticles grown at 700 K HWCVD have densities of  $2 \times 10^{11} \text{ cm}^{-2}$  and  $4 \times 10^{11} \text{ cm}^{-2}$  at 0.1 ML/min and 4.2 ML/min, respectively. Similar to the confined deposition at 700 K, 775 K particle densities decreased with the lower 0.1 ML/min flux compared to 4.2 ML/min except the difference is an order of magnitude,  $2 \times 10^{10} \text{ cm}^{-2}$  and  $2 \times 10^{11} \text{ cm}^{-2}$ , respectively. The remainder of this section examines two data sets for depositions on confined regions while: 1) holding the temperature at 775 K and varying the flux, and 2) holding the flux at 0.1 ML/min and varying the temperature.

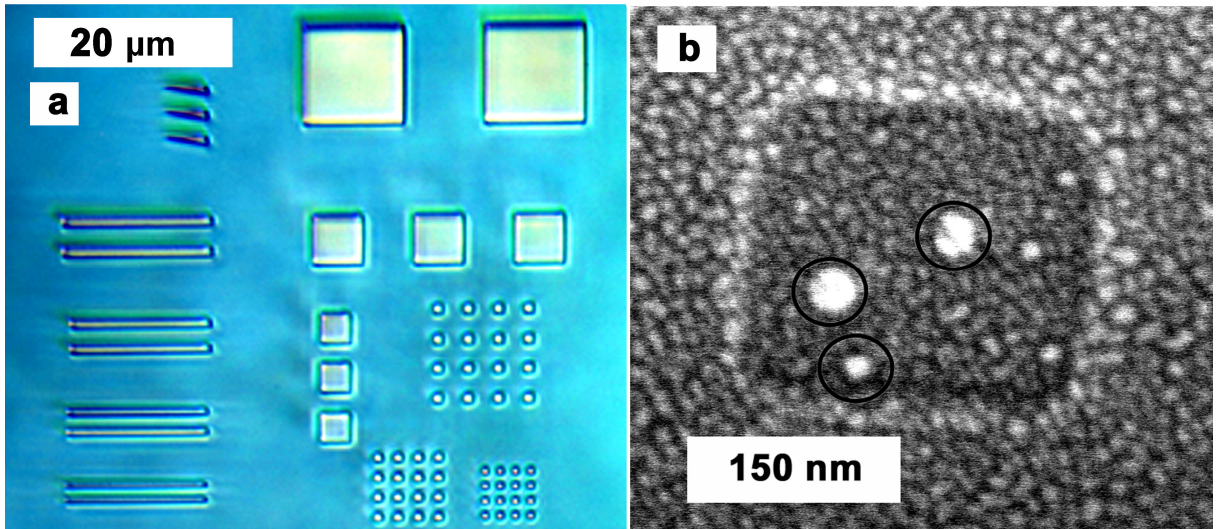


Figure 3.4 a) Optical microscope image of Ebeam lithography patterned PMMA mask on the silicon dioxide top layer before RIE. Feature sizes 600 nm to 100  $\mu\text{m}$  are displayed. b) SEM image of 200 nm wide hafnia box feature confined with the brighter silicon dioxide layer. The three circles surround the largest of the 11 Ge nanoparticles deposited at 775 K, 0.1 ML/min, 8 ML exposure.

Figure 3.5b plots particle density versus feature size at 775 K. Nanoparticle density is not significantly influenced by feature size within this experiment, but is

influenced by flux. The confined depositions at 2.1, 3.2, and 4.2 ML/min fluxes have similar particle densities. The particle densities from 1-10  $\mu\text{m}$  confined regions were averaged and are compared to data obtained from extended surfaces in Figure 3.5c. The particle densities within the confined regions are essentially same as those obtained from extended surfaces for the flux range of 0.6-4.2 ML/min, reaching an asymptotic value of  $\sim 1.7 \times 10^{11} \text{ cm}^{-2}$ . The particle density decreases significantly on extended surfaces and within the confined regions when the flux is decreased to 0.1 ML/min; the particle density on extended surfaces is  $6 \times 10^{10} \text{ cm}^{-2}$ , which is approximately 5 times greater than found for the confined area deposition that is averaged over the 1-10  $\mu\text{m}$  features.

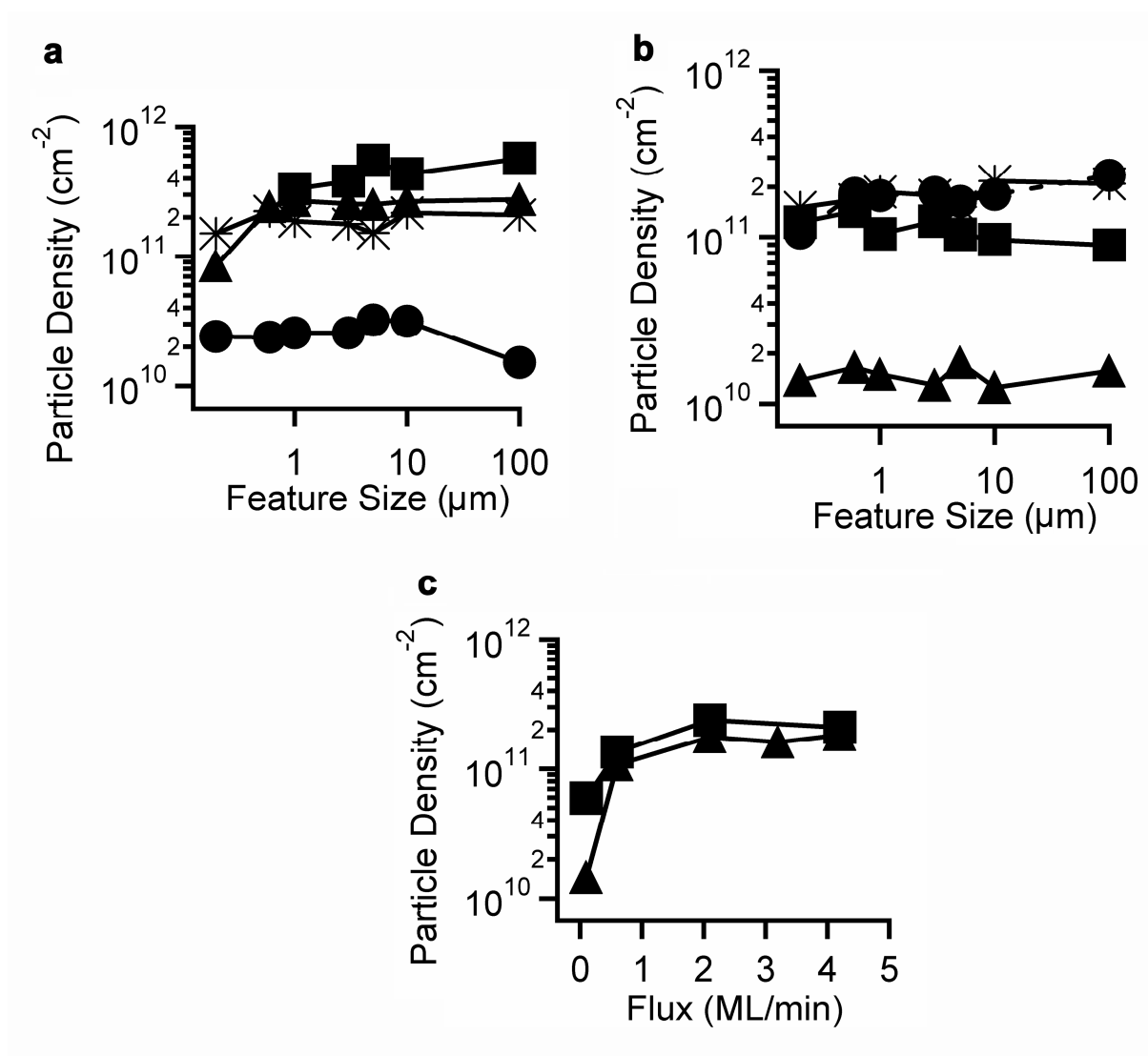


Figure 3.5 a) Ge particle density versus hafnia box size from 8 ML exposure with various combinations of the extremes for temperature (K)/flux (ML/min) conditions: 700/0.1 (▲), 700/4.2 (■), 775/0.1 (●), and 775/4.2 (\*) units are K\*ML/min. b) Ge particle density versus  $\text{HfO}_2$  feature size, 775 K, 8 ML exposure and fluxes: 0.1 (▲), 0.6 (■), 2.1 (●), and 4.2 (\*) units are ML/min. c) Average particle density for 1-10  $\mu\text{m}$   $\text{HfO}_2$  features (▲) and extended surfaces (■) versus flux rate, 775 K, 8 ML exposure.

Particle density data versus box size at 0.1 ML/min is presented in Figure 3.6a for different temperatures. Nanoparticle density is not significantly influenced by the feature

sizes examined; however, it appears to decrease slightly for the 200 and 600 nm features. Particle density does vary with temperature. Overall the particle density is an inverse function of temperature within the confined regions as seen in density data averaged from the 1-10  $\mu\text{m}$  features (Figure 3.6b).

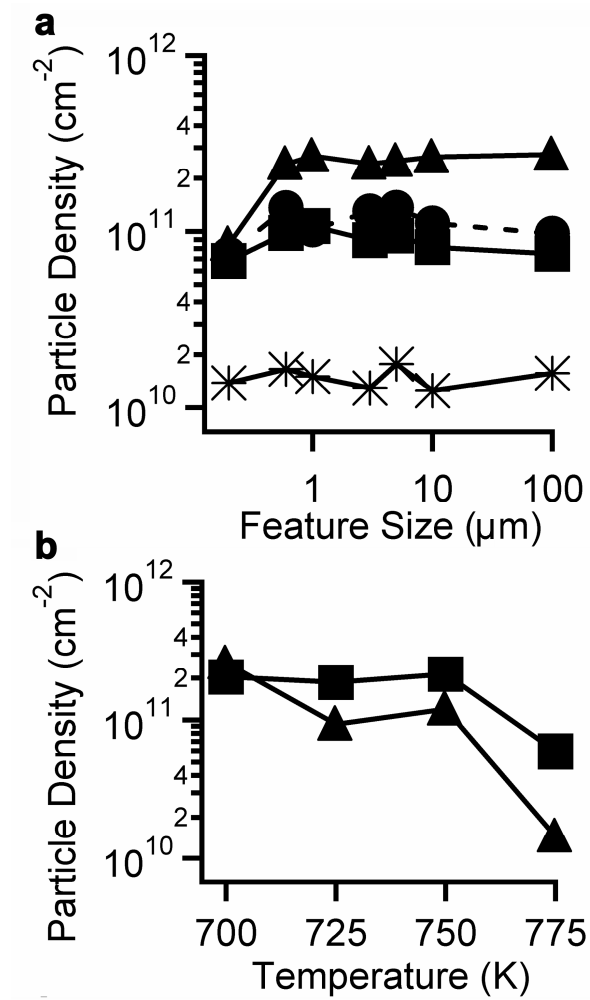


Figure 3.6 a) Ge particle density versus HfO<sub>2</sub> feature size, 0.1 ML/min, 8 ML exposure and temperatures: 700 ( $\blacktriangle$ ), 725 ( $\blacksquare$ ), 750 ( $\bullet$ ), and 775 K ( $\times$ ). b) Average particle density for 1-10  $\mu\text{m}$  HfO<sub>2</sub> features ( $\blacktriangle$ ) and extended surfaces ( $\blacksquare$ ) versus temperature, 0.1 ML/min, 8 ML exposure.

### 3.4 DISCUSSION

#### 3.4.1 Extended Surfaces

The Ge/HfO<sub>2</sub> system experiences formation of an interfacial GeO<sub>x</sub> before metallic Ge<sup>0</sup> accumulates (Figure 3.1a), and both GeO<sub>x</sub> and Ge<sup>0</sup> are stable up to 775 K as investigated using temperature programmed desorption (TPD) [23]. Temperature programmed desorption measures desorption reactions that are completed on the order of tens of seconds. The Ge HWCVD in this chapter occurred over longer time periods. The higher fluxes (2.1 and 4.2 ML/min) deposit 8 ML over time periods of a few minutes while 0.1 and 0.06 ML/min flux growth times are on the order of 1.3 and 2.2 h, respectively. At 775 K, the lower fluxes (less than 0.6 ML/min) have a greater volume of Ge<sup>0</sup> desorbing from the HfO<sub>2</sub> due to longer thermal exposure. Low flux results in lower particle densities when compared to higher fluxes as seen in Figure 3.3a. We believe the slow Ge<sup>0</sup> desorption rate does not influence particle deposition at fluxes greater than 0.6 ML/min (15 min) since density is not a function of flux at these conditions.

The critical cluster size,  $i^*$ , is unique to the material system and is measured by varying the incident deposition flux while maintaining constant temperature. Higher flux rates increase the adatom concentration, thus, increasing the probability of adatoms coalescing and forming a critical cluster and the subsequent nucleation with the addition of one more adatom. Using mean-field nucleation theory [11] Kandel derived Eqns. 3.1 and 3.2 relating the saturation density,  $N_{SAT}$ , to  $i^*$ , the incident deposition flux,  $F$ , temperature,  $T$ , and the activation energies associated with nucleation and growth,

$$N_{SAT} \approx e^{\beta(E^*+i^*E_d)/(i^*+2)} F^{i^*/(i^*+2)} = e^\alpha F^\chi \quad (\text{Limit I}) \quad (3.1)$$

$$N_{SAT} \approx e^{2\beta[E^*+i^*(E_d+E_b)]/(i^*+3)} F^{2i^*/(i^*+3)} = e^\alpha F^\chi \quad (\text{Limit II}) \quad (3.2)$$

where  $E_d$  is the adatom diffusion energy barrier,  $E_b$  is the activation energy required for adatoms joining an already formed island,  $E^*$  is the activation energy of critical cluster formation, and  $\beta = 1/k_bT$  with  $k_b$  as Boltzmann's constant. The value of  $E_b$  is important because the material system will take on energetic relationships leading to one of two physical limits at low surface coverage. Limit I occurs when  $E_b$  is extremely low ( $E_b \rightarrow 0$ ) and the system acts as if the islands are perfect adatom sinks with adatoms joining islands infinitely fast and the island growth is diffusion limited. For Limit II the energy barrier for the attachment of adatoms to islands is the limiting kinetic rate while diffusion is a much faster relative rate. The actual limit our Ge/HfO<sub>2</sub> system approaches is beyond the scope of this paper. The relationships in Equations 3.1 and 3.2 allow one to estimate  $i^*$  when plotting the natural log of the saturation density versus the natural log of deposition flux. The scaling factor,  $\chi$ , obtained from linear regression performed using Microsoft Office Excel<sup>®</sup> software is 0.17 and 0.16 for 700 and 725 K, respectively. We used 700 and 725 K deposition data in this calculation to reduce any potential Ge<sup>0</sup> desorption effects. The calculated  $i^*$  is 0.40 and 0.27 for Limits I and II, respectively. Since  $i^*$  is an integer value in mean-field theory and the values are less than 0.5, we conclude  $i^*$  is likely zero. It is similar to the  $i^* = 0$  value reported for the Ge on SiO<sub>2</sub> system [15]. In mean-field nucleation theory, nucleation occurs when the quantity of atoms in a cluster size equal  $i^*+1$  over a nucleation site; the Ge/HfO<sub>2</sub> system requires only one adatom to create a nuclei.

Several activation energies mentioned earlier influence adatom behavior during particle deposition. The most commonly investigated is the diffusion energy barrier,  $E_d$ . The activation energy required for adatoms joining an existing island,  $E_b$ , influences how quickly free adatoms coarsen particles [8]. We calculate  $E^*$  or the energy barrier required for the formation of a critical cluster, by assuming  $i^* \sim 0$  in Eqns. 3.1 and 3.2.

Plotting the natural log of  $N_{SAT}$  versus  $1/2k_bT$  and  $2/3k_bT$  for Limits I and II, respectively, leads to  $E^* = 0.6 \pm 0.3$  eV for Limit I and  $E^* = 0.4 \pm 0.2$  eV for Limit II. If one assumes the diffusion activation energy ( $E_d$ ) for Ge on  $HfO_2$  is similar in magnitude to the reported values for Ge/ $SiO_2$  [15] and Si/ $SiO_2$  [24] at 0.13 eV and 0.47 eV, respectively, the energy of Ge nucleation on  $HfO_2$  is approximately equivalent to the assumed Ge adatom diffusion energy. Since the Ge/ $HfO_2$  system requires one adatom for nucleation, adatom diffusion appears to regulate nucleation.

### 3.4.2 Confined Deposition

Our  $SiO_2$  hard mask isolates the exposed  $HfO_2$  surface limiting adatom concentrations within the feature dimensions since Ge adatoms cannot diffuse into this area from surrounding  $HfO_2$ . Germanium adatoms that form within the feature dimensions (on the exposed  $HfO_2$ ) can participate in particle nucleation or growth, or potentially interact with the confining  $SiO_2$  at the perimeter to produce volatile Ge having a desorption activation energy of 0.42 eV [15]. We assume the silica perimeter walls remove all Ge adatoms immediately upon contact since our growth temperatures ranged from 700-775 K. The incident  $GeH_x$  deposited directly on the silica is also assumed to desorb immediately. This additional Ge adatom removal channel from the  $HfO_2$  at the perimeter walls explains the lower nanoparticle density with the flux (Figure 3.5c) and temperature (Figure 3.6c) for confined growth when compared to the extended surface results.

Provided the incident flux exceeds the desorption rate, the adatom concentration on the confined surface should be lower by some constant and temperature dependent value. At 775 K and fluxes greater than 0.6 ML/min, the particle density is  $\sim 1.7 \times 10^{11}$   $cm^{-2}$  and is independent of flux (Figure 3.5c) and feature size (Figure 3.5b). Figure 3.5a reveals that the particle density is lower (and feature size independent) at 775 K versus

700 K for the 4.2ML/min flux. (Note that in both cases the feature size independence refers to sizes greater than 1  $\mu\text{m}$ .) Using mean-field nucleation theory, the independence of density on flux leads to a value of  $i^*=0$ , similar to what was found on the extended surface. The rate of nucleation is linearly dependent on the adatom density, i.e.,  $\bar{n}^{(i^*+1)}$  [11], which will be lower for the confined systems due to the Ge loss at the perimeter that leads to a lower density of particles.

The density curves in Figure 3.6a display a similar pattern in that the densities are smaller for the smallest two features (200 and 600 nm). We had hoped to see the smaller density manifested at different sizes with the temperature and from this extract insight into the relative activation energies for adatom diffusion, particle nucleation and adatom loss at the  $\text{SiO}_2$  perimeter. The insensitivity to feature size with temperature suggests that these three processes have similar activation energies of  $\sim 0.4\text{--}0.5$  eV, and all processes increase with temperature at comparable rates.

### 3.5 SUMMARY

We demonstrate the ability of Ge HWCVD onto  $\text{HfO}_2$  surfaces to investigate Volmer-Weber mode kinetics. Critical cluster size was calculated in the range of 0.3–0.4 and is estimated most likely to be zero. The critical cluster activation energy was estimated using mean field nucleation theory as  $0.6 \pm 0.3$  eV or  $0.4 \pm 0.2$  eV for energetic Limits I and II, respectively. Confined deposition decreases nanoparticle density when  $\text{Ge}^0$  desorption is significant by reducing adatom concentration in a similar manner as reducing the deposition flux on extended surfaces. Restricting the  $\text{HfO}_2$  deposition area in the 1 to 100  $\mu\text{m}$  feature dimension range has no effect on particle density with increasing flux when the flux is greater than or equal to 0.6 ML/min. Therefore, the nucleation kinetics are likely unchanged as the  $\text{HfO}_2$  is confined by  $\text{SiO}_2$ . The results on

both the extended and confined surfaces suggest the activation energies for nucleation, surface diffusion, and Ge loss from SiO<sub>2</sub> surfaces are close in value, and the value for Ge loss from SiO<sub>2</sub> has been reported as 0.42 eV.

## REFERENCES

- [1] T. H. Ng, V. Ho, L. W. Teo, M. S. Tay, B. H. Koh, W. K. Chim, W. K. Choi, A. Y. Du, and C. H. Tung, *Thin Solid Films* **462-63**, 46 (2004).
- [2] M. Kanoun, A. Souifi, T. Baron, and F. Mazen, *Appl. Phys. Lett.* **84**, 5079 (2004).
- [3] S. Y. Wang, W. L. Liu, Q. Wan, J. Y. Dai, P. F. Lee, L. Suhua, Q. W. Shen, M. Zhang, Z. T. Song, and C. L. Lin, *Appl. Phys. Lett.* **86**, 113105 (2005).
- [4] Y. Q. Wang, J. H. Chen, W. J. Yoo, Y. C. Yeo, S. J. Kim, R. Gupta, Z. Y. L. Tan, D. L. Kwong, A. Y. Du, and N. Balasubramanian, *Appl. Phys. Lett.* **84**, 5407 (2004).
- [5] J.D. Plummer, M.D. Deal, and P.B. Griffin, *Silicon VLSI Technology: Fundamentals, Practice, and Modeling*, 1 ed. (Prentice Hall, Upper Saddle River, NJ, 2000).
- [6] S. Tiwari, F. Rana, K. Chan, L. Shi, and H. Hanafi, *Appl. Phys. Lett.* **69**, 1232 (1996).
- [7] International Technology Roadmap for Semiconductors; <http://www.itrs.net/>, 2005.

- [8] H. Brune, Surf. Sci. Rep. **31**, 121 (1998).
- [9] J. A. Venables, Surf. Sci. **300**, 798 (1994).
- [10] J. A. Venables, G. D. T. Spiller, and M. Hanbucken, Rep. Prog. Phys. **47**, 399 (1984).
- [11] D. Kandel, Phys. Rev. Lett. **78**, 499 (1997).
- [12] H. Rauscher, J. Braun, and R. J. Behm, Phys. Rev. Lett. **96**, 116101 (2006).
- [13] L. Andersohn, T. Berke, U. Kohler, and B. Voigtlander, J. Vac. Sci. Technol. A **14**, 312 (1996).
- [14] E.F. Vansant, P. Van Der Voort, and K.C. Vrancken, *Characterization and Chemical Modification of the Silica Surface*. (Elsevier, Amsterdam, 1995).
- [15] Q. M. Li, J.L. Krauss, S. Hersee, and S. M. Han, J. Phys. Chem. C **111**, 779 (2006).
- [16] J. H. Zhu, W. T. Leach, S. K. Stanley, J. G. Ekerdt, and X. M. Yan, J. Appl. Phys. **92**, 4695 (2002).
- [17] N. Sugiyama, T. Tezuka, and A. Kurobe, J. Cryst. Growth **192**, 395 (1998).
- [18] J. Chen, W. J. Yoo, Z. Tan, Y. Wang, and D. S. H. Chan, J. Vac. Sci. Tech. A **22**, 1552 (2004).

- [19] W. T. Leach, J. H. Zhu, and J. G. Ekerdt, *J. Cryst. Growth* **243**, 30 (2002).
- [20] W. T. Leach, J. H. Zhu, and J. G. Ekerdt, *J. Cryst. Growth* **240**, 415 (2002).
- [21] C. Basa, Y. Z. Hu, M. Tinani, and E. A. Irene, *J. Vac. Sci. Technol. A* **16**, 3223 (1998).
- [22] F. Mazen, L. Mollard, T. Baron, S. Decossas, and J. M. Hartmann, *Microelec. Eng.* **73-74**, 632 (2004).
- [23] S.K. Stanley, S.V. Joshi, S.K. Banerjee, and J.G. Ekerdt, *J. Vac. Sci. Tech. A* **24**, 78 (2006).
- [24] M. S. Mason, J. K. Holt, and H. A. Atwater, *Thin Solid Films* **458**, 67 (2004).

## **Chapter 4 – Ge Nanoparticles in Organized Nanometer Scale $\text{HfO}_2$ Confined Area**

### **4.1 INTRODUCTION**

Growth of semiconducting nanoparticle arrays by chemical or physical deposition has been demonstrated on semiconductor and dielectric surfaces [1-3]. Chemical vapor deposition (CVD) is a well characterized process in the semiconductor industry and has been investigated for the growth of semiconductor nanoparticles. Size dispersity and random nanoparticle location present challenges in exploiting these growth methods as technological applications rely on the discreteness of size, such as quantum confinement effects, and addressability. Various patterning schemes have been advanced for heteroepitaxial growth on semiconductor substrates that manipulate the strain in the semiconductor substrate to direct nanoparticle positioning [4-8]. In contrast to Stransky-Krastanov growth observed on crystalline semiconductor substrates, Volmer-Weber three-dimensional island growth occurs on amorphous dielectrics producing random arrays of semiconducting nanoparticles [2,9,10]. Many authors have studied Si nanoparticle nucleation on amorphous oxides [2,9,11]. Germanium and SiGe alloy nanoparticle nucleation proceeds in a similar manner and has been studied on a variety of substrates as well [12-18]. Disordered nanoparticle arrays result from the random nature of adatom diffusion on the insulator surface before forming a critical cluster at randomly located nucleation sites [10,11]. These random processes can be somewhat suppressed by using a two-step approach [2] separating nucleation and growth; however, randomness in deposition location still persists. Despite the great number of potential technologies for semiconductor nanoparticles on amorphous insulator substrates, methods to controllably organize nanoparticles on amorphous substrates are lacking.

We report herein this chapter the assembly of Ge nanoparticles into ordered arrays directly on amorphous  $\text{HfO}_2$  to address the particle placement challenge on amorphous dielectric surfaces. Germanium is interesting due to its use in flash memories [18]. Hafnium dioxide is a potential replacement for  $\text{SiO}_2$  as the tunnel oxide in flash memory since its higher capacitance permits a physically thicker layer to be used compared to  $\text{SiO}_2$ , thereby reducing the leakage current in many field effect devices [19]. Further, Ge nanocrystals on hafnium dioxide have been shown to have promising electrical characteristics [19]. Thus, we demonstrate growth of ordered Ge nanoparticle arrays on the  $\text{HfO}_2$  surface during CVD at elevated temperatures. This is possible by patterning a  $\text{SiO}_2$  hard mask and opening up areas to underlying  $\text{HfO}_2$  domains. The patterned  $\text{SiO}_2$  serves as a sacrificial template during hot wire chemical vapor deposition (HWCVD) at 800 K. Because Ge etches  $\text{SiO}_2$  faster than  $\text{HfO}_2$  at this temperature, it is possible to accumulate Ge adatoms on  $\text{HfO}_2$  whereas the Ge adatom concentration on  $\text{SiO}_2$  is too low for nucleation and growth [16,20]. Adatom accumulation on  $\text{HfO}_2$  ultimately leads to nucleation of Ge nanoparticles only on the exposed  $\text{HfO}_2$  surfaces.

In this chapter, lateral order is introduced using the self assembly of a poly(styrene-*b*-methyl methacrylate) [P(S-*b*-MMA)] diblock copolymer on the  $\text{SiO}_2$  mask layer. Self-assembling block copolymer systems undergo phase separation into wide varieties of structures that depend on the polymer species, percent composition, and molecular weights [21,22] and various research groups have used diblock copolymer assembly to template nanoparticle and nanotube deposition using liquid and vapor methods [23-27]. Thin films of poly(styrene-*b*-methyl methacrylate), P(S-*b*-MMA), can organize into poly(methyl methacrylate) cylinders that are perpendicular with a silicon dioxide surface [28,29]. These polymer films afford ideal masks since order is achievable across the majority of a substrate and the minority phase cylinders are

selectively removed, leaving a polystyrene template robust enough to survive reactive ion etching (RIE) and wet etching [28,30,31]. We achieve long range ordered arrays of nanoparticles within 20 nm diameter cylinders with a 40 nm center-to-center spacing between cylinders.

## 4.2 EXPERIMENTAL PROCEDURES AND METHODS

Sematech Inc. provided the 12.5 nm CVD grown silicon dioxide / 10 nm atomic layer deposition (ALD) grown hafnium dioxide film stacks on 8 inch Si(100) wafers. 3.2 cm  $\times$  3.2 cm sized portions were cleaned with an acetone/ethanol/deionized (DI) water rinse then dried with compressed nitrogen. Patterning with a self-assembled diblock copolymer followed published schemes [28,32]. The exposed silica surface was initially pretreated with an  $\alpha$ -hydroxy functionalized random copolymer (60% styrene and 40% methyl methacrylate,  $M_n=8,900$  from Polymer Source Inc.) diluted 1% in toluene by spin coating at 1000 rpm, 30 s. The samples were annealed at 180°C for 48 h allowing the –OH terminated end group to react with the silica surface. Loose polymer strands were removed from the treated surface with a gentle toluene rinse followed by drying with compressed nitrogen. Poly(styrene-*b*-methyl methacrylate),  $M_n=46,100$  and 21,000 of styrene and methyl methacrylate species, respectively, (Polymer Source Inc.) was diluted 1.1% in anisole and was spin coated onto the treated surface under conditions that produce a  $37 \pm 4$  nm thick film that is critical for cylinder self-assembly normal to the substrate. This polymer formulation generates 20 nm diameter cylinders. Further annealing at 180°C for 4 h caused the immiscible polymers to self-assemble. The minority methyl methacrylate cylinder phase was then selectively removed using a 5 min glacial acetic acid bath and a DI water rinse.

Pattern transfer occurred using a  $\text{CHF}_3/\text{O}_2$  RIE chemistry [28] at 200 W and 15 mTorr at room temperature to open holes through the 12.5 nm  $\text{SiO}_2$  to the underlying  $\text{HfO}_2$ . Fluorine based RIE radicals react with  $\text{HfO}_2$  forming species such as  $\text{HfF}_x$ ,  $\text{Hf}_x\text{O}_y$ , and  $\text{C}_x\text{F}_y$  that are nonvolatile at these etching conditions [33]. The hafnium fluorides reveal when the  $\text{HfO}_2$  layer is reached and serve as an etch stop since the  $\text{SiO}_2$  etching byproduct  $\text{SiF}_4$  is volatile under the same conditions. The F 1s X-ray photoelectron spectroscopy (XPS) peak at 685 eV was used as an *ex situ* monitor of the formation of these surface fluorides and their subsequent removal by heating to 875 K. The polymer template was removed using a low power (60 W) RIE  $\text{O}_2$  ashing step. Silica removal from the pore bottom was completed with a brief ~1 or 3 s dip in 2% HF diluted in DI water. The post-etching HF step expanded the pores patterned through the  $\text{SiO}_2$ , resulting in average pore diameters of 20 nm for the 1 s dip and 24 nm for the 3 s dip. The standard deviation of the pore sizes was 3.5 and 4.4 nm for the 1 s and 3 s dip, respectively.

The etched samples were further diced into  $1.6 \times 1.6$  cm squares then loaded into an ultra-high-vacuum (UHV) CVD system described in Chapter 2 and annealed for 15 min at 875 K to degas the surface. The temperature was lowered to within the 700-800 K range before  $\text{GeH}_4$  (diluted 4% in He, from Voltaix Inc.) with a partial pressure of  $1.2 \times 10^{-7}$  Torr was admitted to the deposition chamber. The sample was placed ~3 cm from a tungsten filament supplied with 4 amps current. HWCVD occurs when  $\text{GeH}_4$  molecules decompose on the hot filament and radicals desorb and deposit on the heated sample surface [20,34]. Samples were subjected to 5.6-19 monolayer ( $1 \text{ ML} = 6.3 \times 10^{14}$  atoms/cm<sup>2</sup>) exposures. Ge deposition was confirmed by *in situ* XPS using Al  $K_\alpha$  radiation; the Ge 2p<sub>3/2</sub>, Hf 4f, and Si 2p XPS peaks were monitored before and after HWCVD.

Upon removal from the system, the samples were coated with ~10 nm of Pd/Au to prevent surface charging under analysis in a Hitachi S-4500 field emission scanning electron microscope (SEM). Sputter coating onto blanket wafers was confirmed not to create features that could be interpreted as nanoparticles. Particle size and particle densities are determined by counting particles although it is difficult to resolve nanoparticles less than ~5 nm in diameter.

### 4.3 RESULTS

Figure 4.1a presents a representative SEM image of a patterned sample after 9.4 ML HWCVD Ge exposure at 800 K illustrating the formation of ~10 nm Ge nanoparticles within the features. *In situ* XPS confirmed Ge deposition. Figure 4.1b, Spectrum 3 shows deposition upon the patterned sample with a  $\text{GeO}_x$  peak at ~1220 eV and a larger metallic Ge peak ~1217 eV. The  $\text{HfO}_2$  4f doublet, ~17 and 19 eV, (not shown) attenuated following deposition indicating Ge deposited on the  $\text{HfO}_2$  surface. Confirmation of Ge selective deposition on  $\text{HfO}_2$  and not on  $\text{SiO}_2$  used separate unpatterned  $\text{SiO}_2$  and  $\text{HfO}_2$  samples. Figure 4.1b, Spectrum 2 shows a trace amount of  $\text{GeO}_x$  and Ge formed on unpatterned  $\text{SiO}_2$  for 9.4 ML Ge exposure; the  $\text{SiO}_2$  peak at ~103 eV did not appreciably attenuate (not shown). By comparison a significant metallic Ge peak at 1217 eV with a smaller oxide shoulder at 1220 eV is found in Figure 4.1b, Spectrum 4 for an equivalent Ge exposure on unpatterned  $\text{HfO}_2$ . Less Ge is deposited on the patterned sample, even with greater Ge exposure, because of Ge loss from the  $\text{SiO}_2$  regions through etching or desorption reactions [20,35].

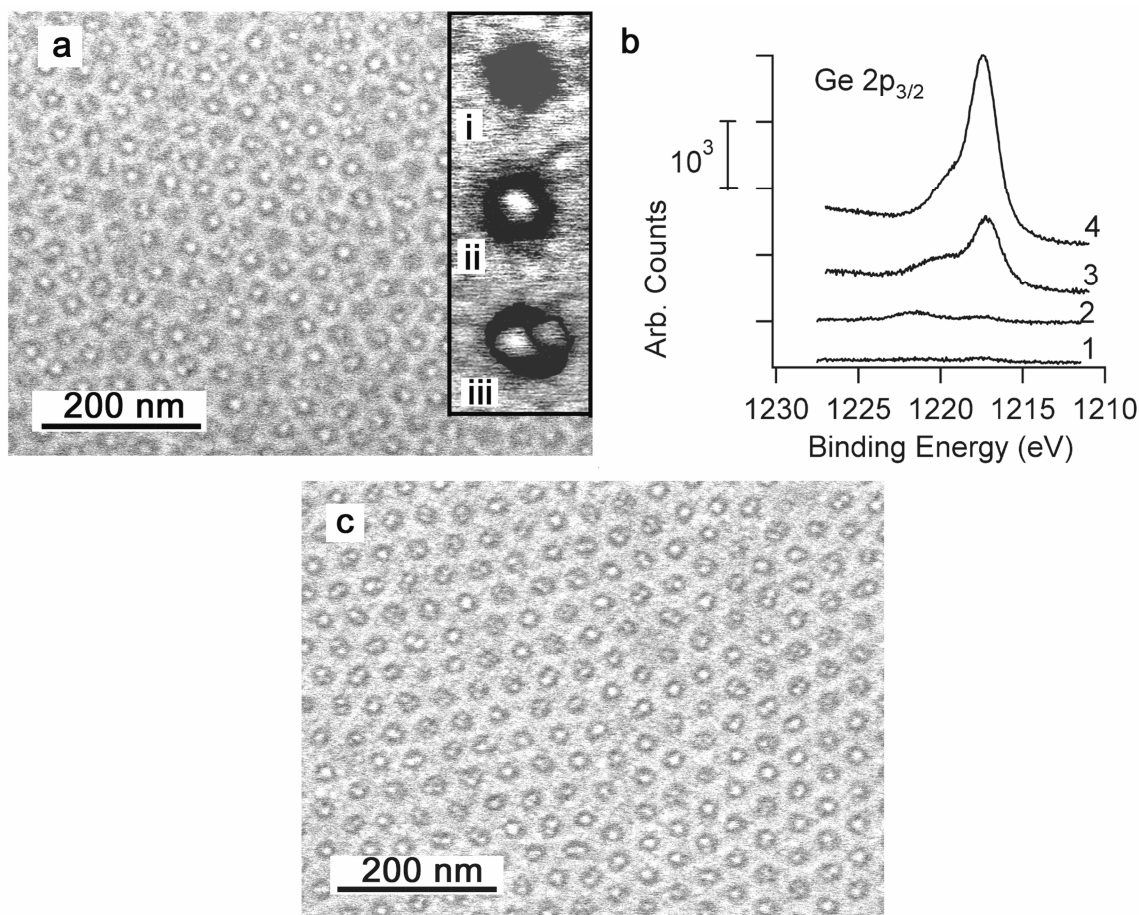


Figure 4.1 a) SEM image of 9.4 ML, 800 K selective Ge deposition upon 3 s HF etched  $\text{SiO}_2$  patterned  $\text{HfO}_2$  pores. Inset are representative, higher resolution SEM images from the same sample that have been digitally enhanced to increase the contrast showing (i) an empty pore, (ii) a singlet and (iii) a doublet. b) Ge  $2p_{3/2}$  XPS peak data confirming selective deposition: (1) baseline on unpatterned  $\text{SiO}_2$  (2) after 9.4 ML deposition on unpatterned  $\text{SiO}_2$  (3) 9.4 ML Ge deposited on patterned surface with 3 s HF etch (4) 7.5 ML Ge exposure upon unpatterned  $\text{HfO}_2$  surface. c) SEM image of selective Ge deposition upon 3 s HF etched patterned sample after 0.8 ML room temperature seeding followed with an 8.6 ML exposure at 800 K.

Close inspection of Figure 4.1a reveals a fraction of the pores are empty and a fraction contains multiple particles. In this particular case of HWCVD alone, about 67 % of the pores are filled with Ge nanoparticles. We note that with HWCVD, a certain

percentage of pores (30%) never grow a nanoparticle and remain empty as existing nanoparticles grow. Increasing the percentage of pores containing nanoparticles requires an additional process step; the surface is first seeded with 0.8 ML of Ge at room temperature and then heated to 800 K followed by HWCVD of an additional 8.6 ML of Ge. Figure 4.1c presents the SEM image of seeded growth on the larger pore samples (3 s HF etch) and 98 percent of the pores are filled.

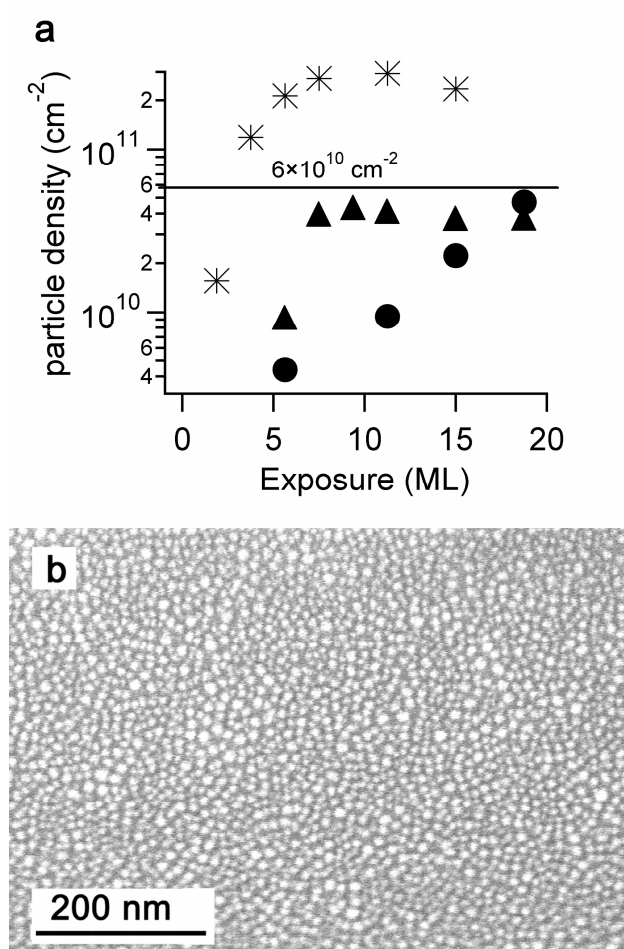


Figure 4.2 a) Plot of Ge nanoparticle density versus Ge exposure for 1 s (●) and 3 s (▲) HF etched patterned samples, and unpatterned HfO<sub>2</sub> (\*). The horizontal line indicates the patterned pore density of  $6 \times 10^{10} \text{ cm}^{-2}$ . b) SEM image of 15 ML, 800 K Ge deposition on an unpatterned HfO<sub>2</sub> surface.

Germanium nanoparticle density (total particles/cm<sup>2</sup>) associated with the smallest pores (1 s HF etch with ~20 nm average diameters), the largest pores (3 s HF etch with ~24 nm average diameters), and unpatterned HfO<sub>2</sub> are plotted in Figure 4.2a as a function of Ge exposure during HWCVD alone. The smallest observable 5 nm diameter nanoparticles appear in both the 20 and 24 nm sized pores after 5.6 ML exposure. 5 nm particles are found at 1.9 ML exposure at 800 K on the unpatterned HfO<sub>2</sub>. The particle

densities increase as a function of increasing exposure and asymptotically approach a density of  $\sim 4 \times 10^{10} \text{ cm}^{-2}$  for the patterned samples. The asymptotic limit is reached at 7.5 ML exposure for 24 nm pore samples and requires a longer 19 ML exposure with the 20 nm pore samples. We speculate the slower approach to the asymptotic limit with the smaller pore samples is due to reduced nucleation or growth rates in these smaller features compared with the slightly larger pores. Interestingly, the particle density for seeded growth, of  $7 \times 10^{10} \text{ cm}^{-2}$ , exceeds the pore density of  $6 \times 10^{10} \text{ cm}^{-2}$ ; some of the excess is related to the presence of doublets (two nanoparticles per pore) in 13 % of available pores and triplets (three nanoparticles per pore) in 1% of available pores (see below). In comparison with Ge deposition on patterned surfaces, a density of  $3 \times 10^{11} \text{ cm}^{-2}$  on the unpatterned  $\text{HfO}_2$  surface occurred with 7.5 ML HWCVD exposure at 800 K and produced particles with 10 nm average diameter. Increasing Ge exposure on the unpatterned  $\text{HfO}_2$  surfaces did not result in a significant density change; the average nanoparticle diameter increased above 20 nm with exposure as seen in Figure 4.2b for the 15 ML Ge exposure. Ion scattering spectroscopy confirms that a continuous film is not present.

The number of nanoparticles per pore and the relative position within a given pore were also examined. Doublets are most frequent in the 24 nm sized pore samples at 7.5 ML exposure with approximately 10 % of available pores having doublets. Interestingly, doublet formation is constant at  $\sim 2\%$  for all exposures in the 20 nm sized pore samples, which we believe is related to nucleation sites and etching as described below. No doublets appear in the 24 nm pores at 5.6 ML exposure, and the fraction of doublets decrease below 3% at 9.4 ML exposure and then 1% as the exposure is further increased. Since the nanoparticle size also increases for the higher exposures, we suggest the loss of doublets at higher exposures is caused by nanoparticle coalescence. Coalescence is

indicated with elongated, large, oval shaped nanoparticles that appear at the higher exposures. Triplets are also present at low (below 1%) amounts in unseeded samples. The seeded sample has a higher concentration of triplets (2%), which will be discussed below.

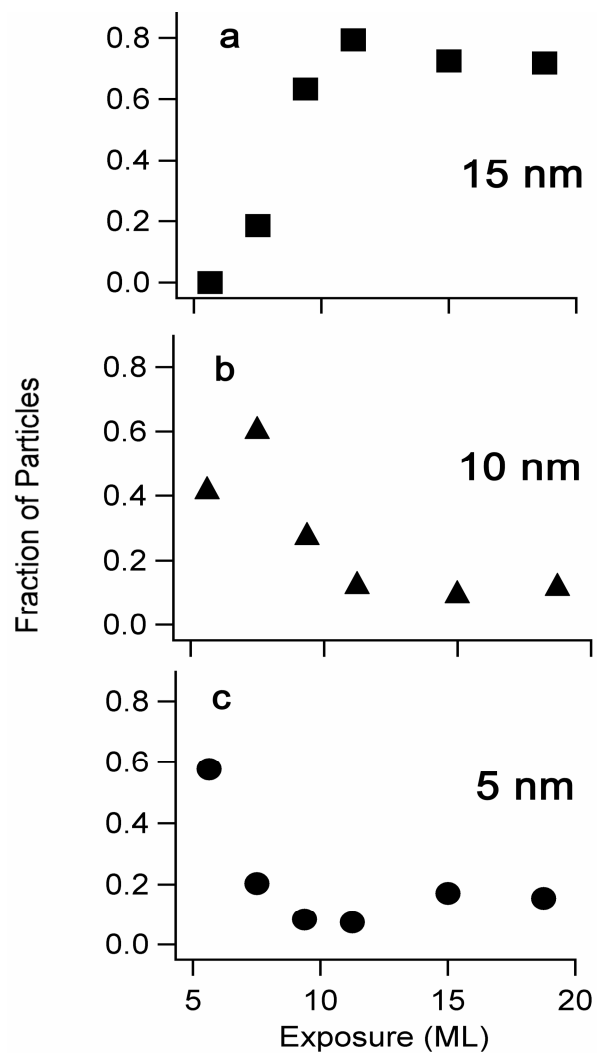


Figure 4.3 Comparison of (a) large (15 nm), (b) medium (10 nm), and (c) small (5 nm) sized nanoparticles as a function of Ge exposure for the 3 s HF etched  $\text{SiO}_2$  pores at 800 K.

The changes in the relative concentrations of 5, 10 and 15 nm nanoparticle with Ge exposure are presented in Figure 4.3 for the 3 s HF-etched pores (24 nm pores). Nanoparticles average less than 10 nm in diameter at 5.6 ML, 800 K exposure and

increase in size as a function of increasing exposure until greater than 75% of nanoparticles are at ~15 nm diameter with 11 ML exposures and higher. The trends in Figure 4.3 also support our assertion of doublet coalescence with increasing Ge exposure.

Relative nanoparticle position within a given pore is separated into two categories for singly-filled pores: 1) near the pore center and 2) near the pore perimeter. Placement examples are shown in Figure 4.4a. We only include singlets (one nanoparticle per pore) and exclude doublets, which are only 1% of all nanoparticles grown. Nanoparticle position with exposure is presented using the ratio of edge/center. The results are similar for both 20 and 24 nm pores in that the ratio is initially greater than 1 and decreases to a common value of ~0.3 as the asymptotic pore fill limit is reached, revealing that the nanoparticles are generally found at the center as particles grow through adatom addition and coalescence at higher exposures. The higher fraction of particles near the perimeter (edge) at the lowest exposures could imply the nucleation sites are randomly distributed on the  $\text{HfO}_2$  since more of the available  $\text{HfO}_2$  area is associated with the perimeter region versus the center region.

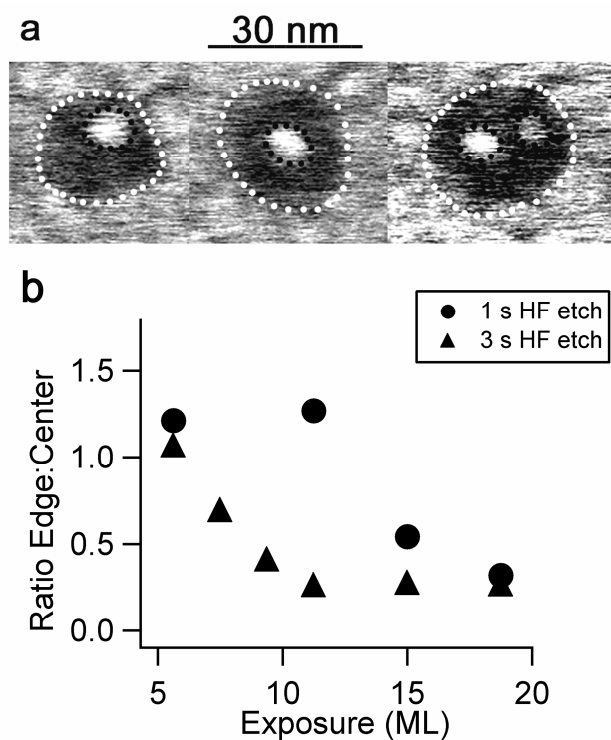


Figure 4.4 a) SEM images demonstrating relative nanoparticle placement in a given pore on a 3 s HF etched patterned sample grown at 800 K. Left image is edge placement, center image is center placement, and right image is two particles in one pore (doublet). b) Plot of nanoparticle placement represented as the ratio of edge/center vs. Ge exposure for 1 s and 3 s HF etched patterned pores counting only pores with one nanoparticle present (singlet).

At 775 K and below, Ge deposition grew into a continuous film covering the hafnia surface or into nanoparticles. Figure 4.5a plots the fraction of pores with continuous films versus surface temperature with 0.4 ML seeding followed with a 5.2 ML HWCVD. At 725 K, ~ 99% of the pores had continuous Ge films. Increasing the HWCVD temperature reduces the fraction of pores with continuous films until the films no longer appear at 800 K. Figure 4.5b plots the fraction of pores without continuous films (nanoparticles) versus surface temperature. With temperatures greater than 725 K,

the Ge films are less common and begin to form nanoparticles having up to three particles per pore. The particles are easily seen in SEM since the contrasting hafnia compared to germanium gives the particles defined outlines as seen in Figure 4.1a. At 800 K, almost all pores have nanoparticles present and continuous films are less than 1% of the total pores.

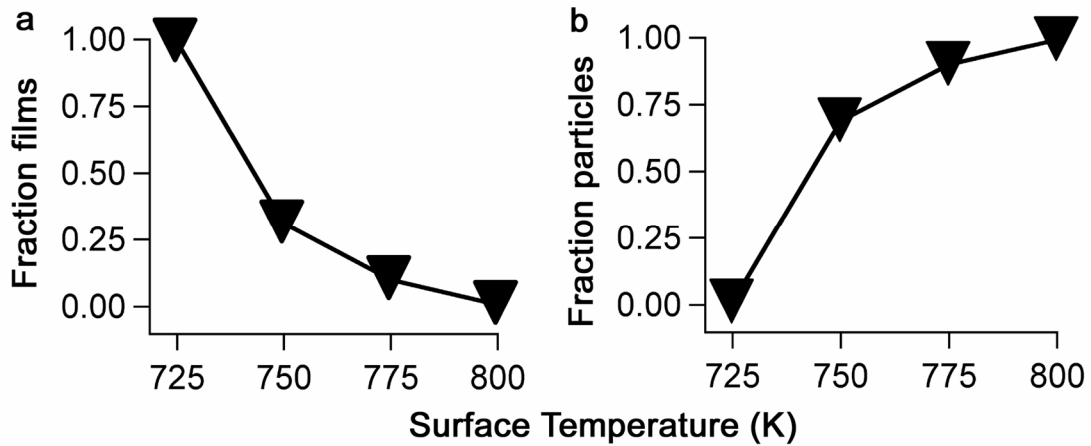


Figure 4.5 a) Plot of the pore fraction with continuous Ge films vs. surface temperature upon 20 nm pore samples seeded with 0.4 ML Ge and later exposed to 5.2 ML Ge exposure during HWCVD. b) Plot of pores with nanoparticles as particle fraction vs. surface temperature for the seeded 20 nm pore samples exposed to 5.6 ML total Ge exposure.

#### 4.4 DISCUSSION

The exact cause(s) for the apparent asymptotic limit corresponding to about 67% of the pores filled with at least one nanoparticle, the more gradual filling of the smaller pores with exposure, and the apparent migration of the nanoparticles to the pore center with increasing exposure remain the subject of further study. Much of the explanation is connected to the fate of an adatom on  $\text{HfO}_2$  and the time scales (or kinetics) for different key steps. During HWCVD at 800 K  $\text{GeH}_x$  fragments and  $\text{GeH}_4$  are incident on the surface and the H desorbs to produce Ge on the surface. Within features defined in the

SiO<sub>2</sub> mask, the adatoms diffuse on the HfO<sub>2</sub> and are lost: 1) through collisions with other adatoms by forming a critical-sized cluster that leads to a stable nucleus, or simply becoming critical (pinned) if the critical size is zero, 2) through collisions with a previously formed nanoparticle and become incorporated into the particle, 3) by desorption from HfO<sub>2</sub> which is insignificant [36] at 800 K, and 4) by reacting with the SiO<sub>2</sub> pore sidewall to produce GeO, which is volatile [20,35] at 800 K. Ge adatom loss processes 1, 2 and 3 are also expected on an unpatterned, extended HfO<sub>2</sub> surface. Loss process 4 controls the nucleation kinetics and particle growth in these small features.

It is the more facile etching of silicon dioxide than hafnium dioxide with Ge that enables the selective deposition of Ge nanoparticles reported herein. Possible etching processes in which Ge reacts with silicon dioxide or hafnium dioxide to form volatile GeO would not be considered feasible from a thermodynamic equilibrium perspective if the reactions are assumed to occur within the bulk. For example, exchange of Si with Ge to convert bulk SiO<sub>2</sub> into bulk GeO<sub>2</sub> is extremely unlikely given a Gibbs energy of formation of 334.9 kJ/mol at 298 K [37]. However, GeO is observed in temperature programmed desorption studies, [16,20] and Ge is demonstrated to strip oxygen from silicon dioxide surfaces [38,39]. The etching reactions occur at the surface and these surface species necessarily form the basis for thermodynamic calculations of equilibrium limits. One possibility is that Ge attacks/inserts into a strained surface Si-O-Si site to form the volatile GeO and create an oxygen surface vacancy. Alternatively, Ge is also reported to desorb from the SiO<sub>2</sub> surface without any chemical interactions with an activation energy of 0.42 eV [35]. The exact mechanism is still under investigation at time of this publication, yet Ge does not accumulate on the SiO<sub>2</sub> hard mask making the selective deposition possible. The precise details and energetics of the possible surface reactions between Ge and SiO<sub>2</sub> await further study.

There is an incubation period at the outset of CVD or HWCVD associated with the accumulation of adatoms to a concentration necessary for nucleation. In addition there is the time between nucleation and the formation of an observable ( $\sim 5$  nm) nanoparticle, [11,34] so the kinetics for nucleation are difficult to access experimentally. Nonetheless, the data in Figure 4.2 illustrate that, in general, as the feature size increases, a higher nanoparticle density results for a given exposure. Figure 4.2 further shows that an infinite-sized feature (unpatterned  $\text{HfO}_2$ ) produces observable nanoparticles at the lowest exposure studied. Clearly there are enough adatoms on the extended surface to enable a high nucleation density for 5.6 ML exposure, yet the density on patterned  $\text{HfO}_2$  is more than an order of magnitude lower for this exposure. We suggest the incubation period is longer in the patterned pores, because the competition between nucleation and  $\text{SiO}_2$  sidewall etching reduces the effective concentration of Ge adatoms. This is demonstrated through the result presented in Figure 4.1c that corresponds to seeding the patterned 24 nm features with 0.8 ML of Ge at room temperature, followed by HWCVD of 8.6 ML at 800 K. In the seeded case, there is a higher concentration of doublets within the pores at 13% and even 1% triplets, and the total particle density of  $7 \times 10^{10} \text{ cm}^{-2}$  exceeds the available patterned pore density of  $6 \times 10^{10} \text{ cm}^{-2}$ . Further, in the seeded case nucleation did not have to compete with etching since the temperature at which nucleation occurred was below the  $\text{GeO}_x$  desorption temperature, so more nuclei formed and were available for growth during the remaining 8.6 ML exposure at 800 K.

Ge adatom removal at the pore sidewalls may also explain the apparent migration of nanoparticles to the center of a pore with increasing exposure. Through depletion reactions we expect the perimeter of a pore to be depleted of Ge adatoms and the center of a pore to have a higher local concentration. If the majority of the adatom collisions

come from the center of the pore, it seems reasonable to conjecture the particles will grow in this direction, appearing to migrate with increasing exposure.

The overall germanium adatom population is reduced from the amount sourced through the incident flux by diffusion on the hafnia and subsequent etching after reacting with silica pore walls. The Ge reacting with  $\text{SiO}_2$  is a function of temperature having a desorption activation energy of approximately 0.42 eV [35]. If the incident flux source is significantly greater than adatom removal through etching, a continuous film forms. Rapid adatom removal prevents film formation resulting in nanoparticle growth. Therefore, selective deposition of nanoparticles in features as small as 20 nm can be managed by controlling the adatom population.

#### **4.5 SUMMARY**

In summary, we demonstrate a method for directing chemical vapor deposition of Ge nanoparticles into features as small as 20 nm in size. The growth is directly on an amorphous, dielectric surface that would find use as the tunnel oxide in advanced memory devices. Finally, by controlling the nucleation process and adatom removal rate, we show it is possible to realize nanoparticle growth in the majority of pores to produce an ordered array of nanoparticles on the amorphous surface.

#### **REFERENCES**

- [1] H. Brune, Surf. Sci. Rep. **31**, 121 (1998).
  
- [2] J. H. Zhu, W. T. Leach, S. K. Stanley, J. G. Ekerdt, and X. M. Yan, J. Appl. Phys. **92**, 4695 (2002).

- [3] T. Baron, A. Fernandes, J. F. Damlencourt, B. De Salvo, F. Martin, F. Mazen, and S. Haukka, *Appl. Phys. Lett.* **82**, 4151 (2003).
- [4] T. I. Kamins and R. S. Williams, *Appl. Phys. Lett.* **71**, 1201 (1997).
- [5] A. Olzierski, A. G. Nassiopoulou, I. Raptis, and T. Stoica, *Nanotechnology* **15**, 1695 (2004).
- [6] T. Stoica, L. Vescan, and E. Sutter, *J. Appl. Phys.* **95**, 7707 (2004).
- [7] T. Kitajima, B. Liu, and S. R. Leone, *Appl. Phys. Lett.* **80**, 497 (2002).
- [8] K. Shiralagi, R. Zhang, and R. Tsui, *J. Cryst. Growth* **202**, 1209 (1999).
- [9] T. Baron, F. Mazen, C. Busseret, A. Souifi, P. Mur, F. Fournel, M. N. Semeria, H. Moriceau, B. Aspard, and P. Gentile, *Microelectron. Eng.* **61-2**, 511 (2002).
- [10] J. Bloem, *J. Cryst. Growth* **50**, 581 (1980).
- [11] C. Basa, M. Tinani, and E. A. Irene, *J. Vac. Sci. Tech. A* **16**, 2466 (1998).
- [12] T. Baron, B. Pelissier, L. Perniola, F. Mazen, J. M. Hartmann, and G. Rolland, *Appl. Phys. Lett.* **83**, 1444 (2003).
- [13] V. L. Dalal, *Curr. Opin. Solid State Mat. Sci.* **6**, 455 (2002).

- [14] R. Gupta, W. J. Yoo, Y. Q. Wang, Z. Tan, G. Samudra, S. Lee, D. S. H. Chan, K. P. Loh, L. K. Bera, N. Balasubramanian, and D. L. Kwong, *Appl. Phys. Lett.* **84**, 4331 (2004).
- [15] D. W. Kim, S. B. Hwang, T. F. Edgar, and S. Banerjee, *J. Electrochem. Soc.* **150**, G240 (2003).
- [16] S.K. Stanley, S.V. Joshi, S.K. Banerjee, and J.G. Ekerdt, *J. Vac. Sci. Tech. A* **24**, 78 (2006).
- [17] Y.Q. Wang, J.H. Chen, W. J. Yoo, and Y. C. Yeo, *Mater. Res. Soc. Symp. Proc.* **830**, D6.3.1 (2005).
- [18] H. G. Yang, Y. Shi, L. Pu, R. Zhang, B. Shen, P. Han, S. L. Gu, and Y. D. Zheng, *Appl. Surf. Sci.* **224**, 394 (2004).
- [19] S. Y. Wang, W. L. Liu, Q. Wan, J. Y. Dai, P. F. Lee, L. Suhua, Q. W. Shen, M. Zhang, Z. T. Song, and C. L. Lin, *Appl. Phys. Lett.* **86**, 113105 (2005).
- [20] S.K. Stanley, S.S. Coffee, and J.G. Ekerdt, *App. Surf. Sci.* **252**, 878 (2005).
- [21] C. Park, J. Yoon, and E.L. Thomas, *Polymer* **44**, 6725 (2003).
- [22] R. A. Segalman, *Mater. Sci. Eng. R Rep.* **48**, 191 (2005).
- [23] G. Kastle, H. G. Boyen, F. Weigl, G. Lengl, T. Herzog, P. Ziemann, S. Riethmuller, O. Mayer, C. Hartmann, J. P. Spatz, M. Moller, M. Ozawa, F. Banhart, M. G. Garnier, and P. Oelhafen, *Adv. Funct. Mater.* **13**, 853 (2003).

- [24] S. Lastella, Y. J. Jung, H. C. Yang, R. Vajtai, P. M. Ajayan, C. Y. Ryu, D. A. Rider, and I. Manners, *J. Mater. Chem.* **14**, 1791 (2004).
- [25] C. Hinderling, Y. Keles, T. Stockli, H. E. Knapp, T. de los Arcos, P. Oelhafen, I. Korczagin, M. A. Hempenius, G. J. Vancso, R. L. Pugin, and H. Heinzelmann, *Adv. Mater.* **16**, 876 (2004).
- [26] Y. Lin, A. Boker, J. B. He, K. Sill, H. Q. Xiang, C. Abetz, X. F. Li, J. Wang, T. Emrick, S. Long, Q. Wang, A. Balazs, and T. P. Russell, *Nature* **434**, 55 (2005).
- [27] C. L. Zhang, T. Xu, D. Butterfield, M. J. Misner, D. Y. Ryu, T. Emrick, and T. P. Russell, *Nano Letters* **5**, 357 (2005).
- [28] K. W. Guarini, C. T. Black, Y. Zhang, H. Kim, E. M. Sikorski, and I. V. Babich, *J. Vac. Sci. Tech. B* **20**, 2788 (2002).
- [29] K. W. Guarini, C. T. Black, and S. H. I. Yeuing, *Adv. Mater.* **14**, 1290 (2002).
- [30] C. Harrison, M. Park, P. M. Chaikin, R. A. Register, and D. H. Adamson, *J. Vac. Sci. Tech. B* **16**, 544 (1998).
- [31] X. M. Yang, S. G. Xiao, C. Liu, K. Pelhos, and K. Minor, *J. Vac. Sci. Tech. B* **22**, 3331 (2004).
- [32] K. W. Guarini, C. T. Black, K. R. Milkove, and R. L. Sandstrom, *J. Vac. Sci. Technol. B* **19**, 2784 (2001).

- [33] J. Chen, W. J. Yoo, Z. Tan, Y. Wang, and D. S. H. Chan, J. Vac. Sci. Tech. A **22**, 1552 (2004).
- [34] W. T. Leach, J. H. Zhu, and J. G. Ekerdt, J. Cryst. Gr. **240**, 415 (2002).
- [35] Q. M. Li, J.L. Krauss, S. Hersee, and S. M. Han, J. Phys. Chem. C **111**, 779 (2006).
- [36] S.K. Stanley and J.G. Ekerdt, Mater. Res. Soc. Symp. Proc. **879E**, Z3.23 (2005).
- [37] various authors, in *"Standard Thermodynamic Properties of Chemical Substances" in CRC Handbook of Chemistry and Physics, Internet Version* (CRC Press, Boca Raton, FL, 2005), Vol. 85.
- [38] A. A. Shklyayev and M. Ichikawa, Surf. Sci. **514**, 19 (2002).
- [39] C. L. Wang, S. Unnikrishnan, B. Y. Kim, D. L. Kwong, and A. F. Tasch, J. Electrochem. Soc. **143**, 2387 (1996).

## **Chapter 5 - Selective silicon nanoparticle growth on high density arrays of silicon nitride**

### **5.1 INTRODUCTION**

Since the beginning of the integrated circuit industry in the 1960's, device performance has increased significantly as device dimensions decreased. With current devices being fabricated on the nanometer scale, final products magnify fabrication errors as the tolerance magnitudes decrease. Silicon nanocrystal-based flash memory has been successfully fabricated and tested as a proposed future generation device using nanocrystals grown via chemical vapor deposition (CVD) [1,2]. As the size of the memory cell decreases in the future [3], reliable device operation demands a low particle size distribution and ordered lateral placement. CVD nucleation on amorphous insulator surfaces is unorganized in nature due to randomly positioned nucleation sites [4–6], and spatially restricting the domain region over which nucleation occurs is one approach toward ordered lateral nanoparticle placement.

We have previously shown with Ge [7], that selective nanoparticle placement is possible during hot wire chemical vapor deposition (HWCVD) by employing a thin (12 nm) SiO<sub>2</sub> mask through which ~ 22 nm vias are etched to expose HfO<sub>2</sub>. The more facile etching by adsorbed Ge of SiO<sub>2</sub> versus HfO<sub>2</sub> [8], affords a kinetic window between 700 and 800 K in which the Ge adatoms can accumulate on HfO<sub>2</sub> and not on SiO<sub>2</sub>, and eventually nucleate and grow into nanoparticles selectively on the HfO<sub>2</sub> regions. The lower limit of this window is set by a temperature required to etch SiO<sub>2</sub> faster than the adsorption of Ge (or more correctly GeH<sub>x</sub> by thermally cracking GeH<sub>4</sub> over a filament). The upper temperature is set to minimize Ge loss from HfO<sub>2</sub> by etching reactions. The

kinetic window for Si etching of SiO<sub>2</sub> versus HfO<sub>2</sub> is more narrow (900-925 K), and as a consequence Si nanoparticle growth is not as selective as was found for Ge. Silicon nanoparticles deposited at 900 K were found on both SiO<sub>2</sub> and HfO<sub>2</sub>, however, with a considerably higher density on HfO<sub>2</sub> [9]. Silicon nitride is not etched by adsorbed Si [10] and is therefore ideally suited for the selective CVD growth of Si nanoparticles employing a SiO<sub>2</sub> sacrificial mask. With Si on Si<sub>3</sub>N<sub>4</sub> there is no upper etching limit, enabling one to work over a wider temperature range to observe the effects of adatom concentration on nucleation and growth.

The kinetics of Si and Ge island nucleation and nanoparticle growth have been reported on SiO<sub>2</sub> and Si<sub>3</sub>N<sub>4</sub> surfaces [10–13]. Modeling approaches that relate island (or particle) density to the growth rate and temperature permit one to establish the critical cluster size,  $i^*$ , and the diffusion barrier for adatoms on the surface [14–17]. When one more adatom attaches to a critical cluster, a stable island/particle forms and beyond this  $i^*+1$  condition the nucleated island/particle experiences growth. A critical cluster size of zero has been found for Ge on SiO<sub>2</sub> [11] and a value of 1 was assumed for Si on SiO<sub>2</sub> [13]. This implies that high adatom concentrations should not be required for nucleation on amorphous surfaces given that the density of unstable island/particles of size  $i$ , that can grow into a critical cluster is proportional to the total adatom density to the power  $i$ , and the nucleation rate is proportional to the average adatom density to the power  $i^*+1$  [16]. Activation energies of 0.13 eV [18] and 0.47 eV [13] have been reported for the diffusion of Ge on SiO<sub>2</sub> and Si on SiO<sub>2</sub>, respectively, so the adatoms are expected to diffuse rapidly on the surface. The critical cluster size and diffusion energy are not reported for Si on Si<sub>3</sub>N<sub>4</sub>, however, they are likely to be similar in magnitude to those reported for Si on SiO<sub>2</sub>.

Baron *et al.* measured the total accumulation of Si into nanoparticles and referred to the accumulation rate as a nucleation-growth rate; they reasoned nucleation contributes most to the growth rate [12]. They report nucleation-growth activation energies of 3.84 eV and 2.83 eV on SiO<sub>2</sub> and Si<sub>3</sub>N<sub>4</sub>, respectively [12]. Miyazaki *et al.* reported that the activation energy for Si nanoparticle growth on thermally-grown SiO<sub>2</sub> decreases from 4.8 eV to 1.75 eV by fully hydroxylating the surface through an HF etch and associated the lowered energy with a more reactive surface [4]. Leach *et al.* observed higher densities and attainment of these densities faster, or at lower temperatures, over Si<sub>3</sub>N<sub>4</sub> versus SiO<sub>2</sub> and associated this to a more reactive Si<sub>3</sub>N<sub>4</sub> surface toward activation of the Si<sub>2</sub>H<sub>6</sub> precursor and with the complete retention of any Si adatoms on Si<sub>3</sub>N<sub>4</sub> [10]. Even if the diffusion rates for Si on SiO<sub>2</sub> and Si<sub>3</sub>N<sub>4</sub> are similar in magnitude, the diffusion is likely slower on Si<sub>3</sub>N<sub>4</sub> and this would also contribute to a higher nucleation rate and density on Si<sub>3</sub>N<sub>4</sub>. Growth rates on SiO<sub>2</sub> and Si<sub>3</sub>N<sub>4</sub> from hydride sources then appear to be controlled by the activation of the hydrides and their transformation into adatoms.

This chapter reports the influence of adatom concentration on nanoparticle nucleation and growth within the confined regions. Due to the limited area particles may occupy and the limited surface area on which Si adatoms can accumulate, the balance between adatom accumulation and Si loss through etching at the SiO<sub>2</sub> sidewalls is extremely sensitive to precursor flux and temperature. This balance affects formation of multiple particles growing within the pores and the fraction of pores with particles. CVD and HWCVD are employed to deliver either Si<sub>2</sub>H<sub>6</sub> or SiH<sub>x</sub> radicals to the surface.

## 5.2 EXPERIMENTAL PROCEDURE

Freescale Inc. provided the 15 nm plasma enhanced CVD SiO<sub>2</sub>/30 nm plasma enhanced CVD Si<sub>3</sub>N<sub>4</sub> grown stack structures 8-in p-doped Si(100) wafers. After dicing into smaller pieces, 3.2 × 3.2 cm sized portions were cleaned with an acetone/ethanol/deionized (DI) water rinse then dried with compressed nitrogen. Patterning with a self-assembled diblock copolymer followed published schemes [19,20]. The exposed silica surface was initially pretreated with an  $\alpha$ -hydroxy functionalized random copolymer (60% styrene and 40% methyl methacrylate,  $M_n=8,900$  from Polymer Source Inc.) diluted 1% in toluene by spin coating at 1000 rpm for 30 s. The samples were annealed at 180°C for 48 h allowing the –OH terminated end groups to react with the silica surface. Loose polymer strands were removed from the treated surface with a gentle toluene rinse followed by drying with compressed nitrogen. Poly(styrene-*b*-methyl methacrylate),  $M_n=46,100$  and 21,000 of styrene and methyl methacrylate species, respectively, (Polymer Source Inc.) was diluted 1.1% in anisole and was spin coated onto the treated surface under conditions that produce a  $37 \pm 4$  nm thick film that is critical for cylinder self-assembly normal to the substrate. This polymer formulation generates 20 nm diameter cylinders. Further annealing at 180°C for 4 h caused the immiscible polymers to self-assemble. The minority methyl methacrylate cylinder phase was then selectively removed using a 5 min glacial acetic acid bath and a DI water rinse.

Pattern transfer through the 15 nm SiO<sub>2</sub> film used a CHF<sub>3</sub>/O<sub>2</sub> reactive ion etch (RIE) at 200 W and 15 mTorr at room temperature. Silicon nitride is etched at less than half the rate of silicon dioxide under these conditions [21]. The time necessary to etch the SiO<sub>2</sub> was determined using a liftoff technique [19] in which incomplete Pd/Au films were sputtered on the RIE-etched samples before dipping in 1% HF to remove all

remaining SiO<sub>2</sub>. SiO<sub>2</sub> etches at a significantly higher rate in HF than silicon nitride, therefore, some sputtered metal remains behind after the HF etch when the Si<sub>3</sub>N<sub>4</sub> surface is reached during the RIE. As a check, the N 1s X-ray photoelectron spectroscopy (XPS) peak centered at 398 eV for silicon nitride was monitored in *ex situ* studies and it increases significantly as the nitride surface is exposed, signaling etch completion. The fully etched samples were then subjected to a 2 s 1% HF etch to remove any residual SiO<sub>2</sub> from the bottom of the features. The final exposed silicon nitride pore diameter after processing was  $17 \pm 3.2$  nm with a pore density of  $6 \times 10^{10}$  cm<sup>-2</sup>.

The etched samples were further diced into  $1.6 \times 1.6$  cm squares then loaded into the ultra-high-vacuum (UHV) CVD system described in Chapter 2 [10] and annealed for 15 min at 1075 K to degas the surface and remove any potential SiO<sub>x</sub>N<sub>y</sub> native oxides [22] from the Si<sub>3</sub>N<sub>4</sub> surface. This annealing step was necessary because Si etches the native oxide and this prevents Si adatom accumulation and Si nanoparticle nucleation during the early stages of a HWCVD experiment. *In situ* XPS confirmed removal of native surface oxides. Trace amounts of carbon were observed with XPS on the samples after annealing. The temperature was lowered to 975 K before Si<sub>2</sub>H<sub>6</sub> (diluted 4% in He, from Voltaix Inc.) with a partial pressure of  $2.0 \times 10^{-8}$  Torr was admitted to the deposition chamber. The sample was placed ~3 cm from a tungsten cracking filament supplied with 4 amps current (>1500°C) resulting in a flux of 0.3 monolayer/min (1 ML =  $6.8 \times 10^{14}$  atoms/cm<sup>2</sup>). HWCVD occurs when Si<sub>2</sub>H<sub>6</sub> molecules decompose on the hot filament with radicals desorbing and depositing on the heated sample surface. Fluxes were calibrated on thermally grown SiO<sub>2</sub> at room temperature by depositing an amorphous Si film [23]. XPS peak attenuation for the Si 2p peak of the oxide at 103.5 eV was used to establish the Si film thickness.

HWCVD studies explored total exposures equivalent to 1-15 ML, fluxes ranging from 0.1 to 0.9 ML/min, and temperatures ranging from 900-1025 K. CVD was conducted over a temperature range of 900-975 K while holding the disilane partial pressure at  $1 \times 10^{-4}$  Torr. Si deposition was confirmed *in situ* with XPS using Al  $K_{\alpha}$  radiation. The Si 2p, O 1s, and N 1s peak binding energies were adjusted for charging using the C 1s peak (from trace contaminants) at 285 eV. The high temperature process causes the silica hard mask to buckle locally in approximately 20% of the patterned samples, destroying small ( $\sim 1,000 \text{ nm}^2$  area) regions. One sample was given the 1075 K anneal without any silicon deposition and the buckling occurred revealing the initial anneal as the damage source. The buckled regions are not included within the particle statistics in this paper.

Upon removal from the system, the samples were coated with  $\sim 10 \text{ nm}$  of Pd/Au to prevent surface charging under analysis in a Hitachi S-4500 field emission scanning electron microscope (SEM). Sputter coating onto blanket wafers was confirmed not to create features that could be interpreted as nanoparticles. Particle size and particle densities are determined by counting particles after digitally magnifying the SEM images. Nanoparticles less than  $\sim 5 \text{ nm}$  in diameter are difficult to resolve. The particles were categorized with three designations according to diameter: small (5-8 nm), medium (9-11 nm), and large (13 nm and greater). When the entire pore is filled, a fourth category, film with a diameter of 17 nm, is used. For a given growth condition (sample), approximately 400 particles and never fewer than 300 particles were counted. The particle counts in each category are averaged to give an overall nanoparticle diameter. Particle crystallinity was not determined.

### 5.3 RESULTS

It is possible to deposit Si selectively on  $\text{Si}_3\text{N}_4$  and not on  $\text{SiO}_2$  provided the etching rate of  $\text{SiO}_2$  by adsorbed Si exceeds the rate of Si adatom generation. The  $\text{SiO}_2$  etching reaction has an onset in TPD studies near 825 K and a peak maximum near 900 K [10]; therefore, the majority of the experiments reported herein were done at 975 K to ensure a rapid etching reaction under a continuous incidence of the silicon precursor. In addition, Si nanoparticles were not observed in SEM images on the  $\text{SiO}_2$  surface for any samples.

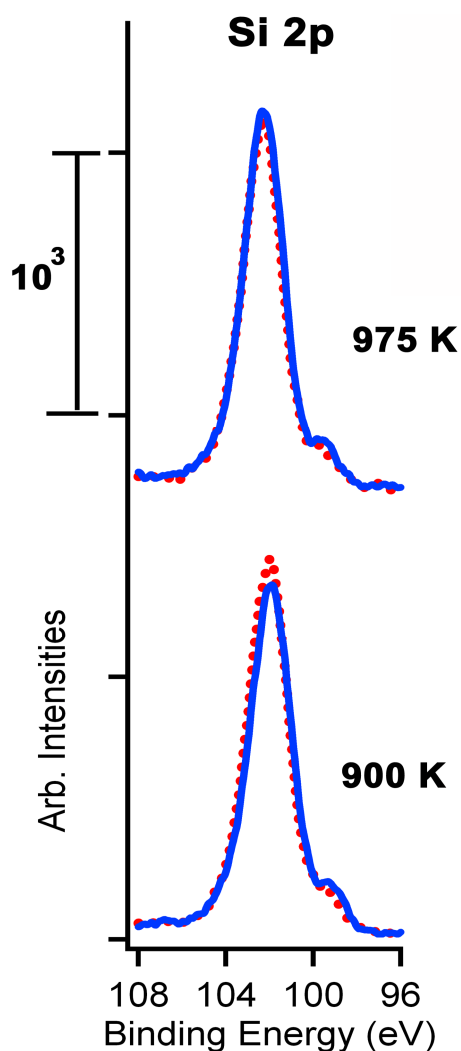


Figure 5.1 XPS showing Si 2p signals for thermal CVD at 900 and 975 K. The  $2.0 \times 10^{-8}$  Torr  $\text{Si}_2\text{H}_6$  partial pressure is equivalent to the background pressure used during the 0.3 ML/min HWCVD flux depositions. CVD exposure lasted 50 min or the equivalent amount of time required for a 15 ML HWCVD exposure originating at the tungsten filament generating radicals. (The dashed lines represent the signals before deposition.)

Control experiments were performed to determine if thermal CVD was possible on  $\text{Si}_3\text{N}_4$  from  $\text{Si}_2\text{H}_6$  at the HWCVD pressure of  $2.0 \times 10^{-8}$  Torr and with the cracking filament turned off. Figure 5.1 presents the Si 2p peaks before and after exposure of

extended  $\text{Si}_3\text{N}_4$  to  $2.0 \times 10^{-8}$  Torr  $\text{Si}_2\text{H}_6$  for 50 min with the cracking filament off. This particular pressure and time produces a 0.3 ML/min flux and 15 ML total deposition when the cracking filament is on. Slight variations in repositioning of the samples for XPS analysis makes comparison of absolute peak intensities an unreliable measure of changes in coverage when the peak differences are on the order of 10%, as reflected in the 102 eV feature for both 900 and 975 K. The ratio of the Si 2p XPS feature for metallic Si (99 eV) to the Si in  $\text{Si}_3\text{N}_4$  (102 eV) should increase after CVD exposure when compared to the ratio before CVD exposure if Si is depositing on the  $\text{Si}_3\text{N}_4$ . This ratio increased from 0.099 before exposure to 0.123 after exposure at 900 K, an increase of 23 %. The ratio increase was 29 % at 975 K and 31 % at 1025 K indicating that more Si was deposited at the higher temperatures. The SEM images (not shown) were featureless and this would result if any particles formed and were less than 3 nm in diameter. Therefore we conclude the  $\text{Si}_3\text{N}_4$  surface is reactive enough that some level of Si adatom accumulation is possible from the uncracked  $\text{Si}_2\text{H}_6$  that will also be present during the HWCVD experiments.

Studies have shown that defects can increase the nucleation density of Si nanoparticles on  $\text{SiO}_2$  surfaces [24,25], so control experiments were performed to determine if the  $\text{CHF}_3/\text{O}_2$  pattern transfer RIE process altered the reactivity of the  $\text{Si}_3\text{N}_4$  at the bottom of the features. Figure 5.2 presents SEM images for unpatterned, extended  $\text{Si}_3\text{N}_4$  surfaces that had the  $\text{SiO}_2$  layer removed by HF wet etching versus removed by the RIE process, followed by the brief (2 s) 1% HF etch. These surfaces were subjected to Si CVD ( $1 \times 10^{-4}$  Torr  $\text{Si}_2\text{H}_6$ ) at 925 K for 4 min. The RIE-exposed sample reveals 5-25 nm Si nanoparticles with a density of  $1 \times 10^{11} \text{ cm}^{-2}$ , while the HF-exposed sample had significantly less growth with 5-10 nm particles and a  $2 \times 10^{10} \text{ cm}^{-2}$  density. Therefore the results for Si grown on patterned  $\text{Si}_3\text{N}_4$  regions in this study may not be directly

correlated against those on as-grown  $\text{Si}_3\text{N}_4$  extended surfaces because of the RIE process-induced damage. The nature of the defects and the cause for the increased nucleation were beyond the scope of this study.

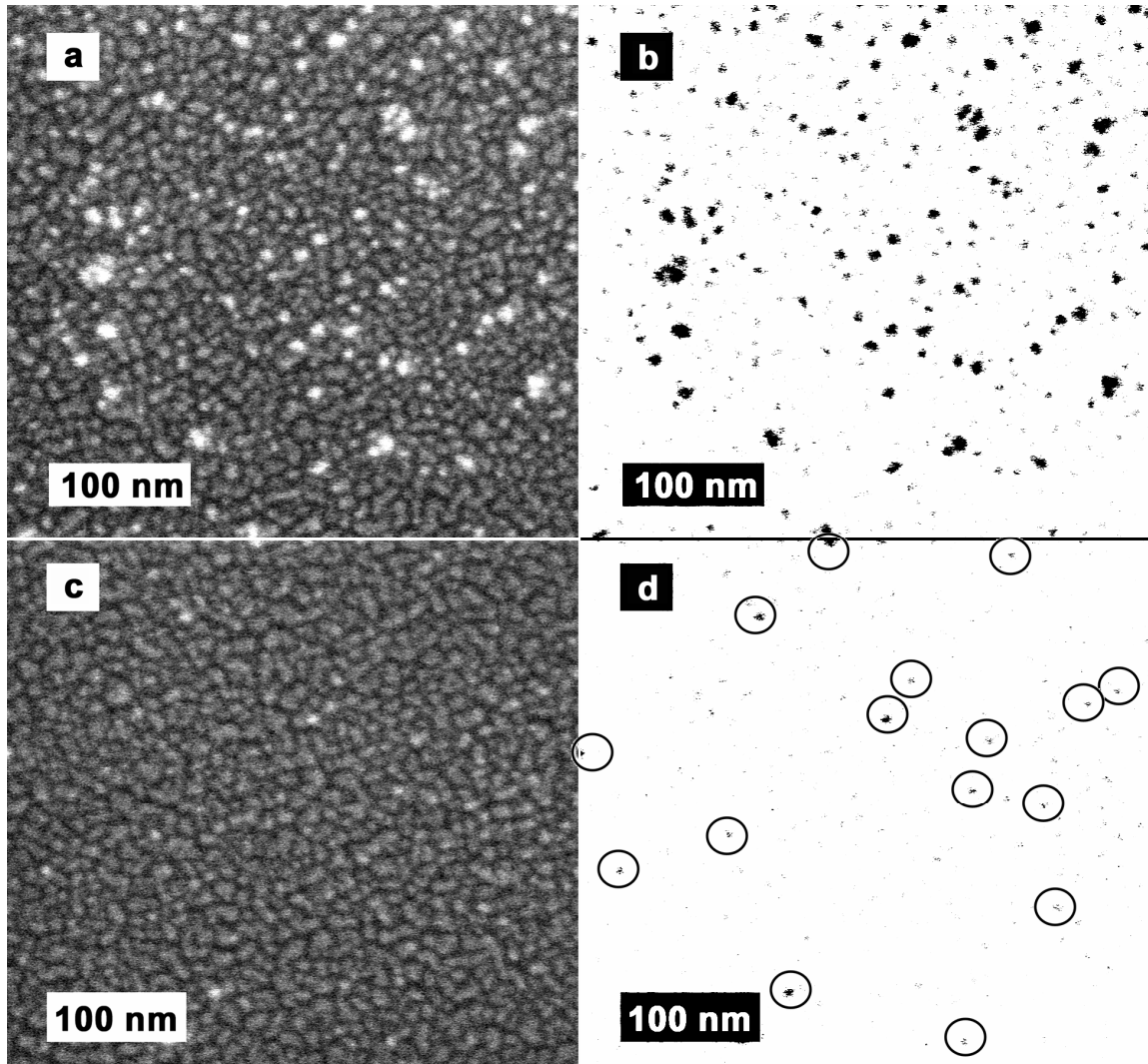


Figure 5.2 SEM images of 4 min thermal CVD on extended  $\text{Si}_3\text{N}_4$  at 975 K and a disilane pressure of  $1 \times 10^{-4}$  Torr. a) The  $\text{SiO}_2$  hard mask was removed using HF and the underlying  $\text{Si}_3\text{N}_4$  had a 20 s exposure to the 200 W  $\text{CHF}_3/\text{O}_2$  RIE chemistry used in processing patterned samples. The particle density is  $1 \times 10^{11} \text{ cm}^{-2}$  and particles range in diameter from 5-25 nm. b) The negative image of Part a where the particles are easily observed as black spots. c) The  $\text{SiO}_2$  hard mask was removed using HF without any further steps and given the same thermal CVD as Part a. The particle density is  $2 \times 10^{10} \text{ cm}^{-2}$  and particles range in diameter from 5-10 nm. d) The negative image of Part c with circles around the 16 black spots that correspond to particles greater than 5 nm in diameter.

Growth was observed in ~100% of the pores following 3 min of thermal CVD (18,000 Langmuir  $\text{Si}_2\text{H}_6$ ) at all temperatures in the 900-975 K range. Silicon growth characteristics varied significantly with temperature. At 900 K, Si films that completely filled the pores, formed and appeared to grow out of the pores and over portions of the  $\text{SiO}_2$  mask since the Si 2p XPS feature associated with  $\text{SiO}_2$  (103.5 eV) was attenuated. The fraction of pores that were filled by a complete film decreased with increasing temperature as illustrated in Figure 5.3. As the temperature increased, the average diameter of the Si deposited decreased, reaching 11 nm at 975 K. Counting a continuous film as one particle, the density increased from the pore density value of  $6.0 \times 10^{10} \text{ cm}^{-2}$  at 900 K to  $6.1 \times 10^{10}$  and  $6.7 \times 10^{10} \text{ cm}^{-2}$  at 950 and 975 K, respectively. The changes in size and in density with temperature suggest less coalescence of particles is occurring because less growth is taking place. Two factors can contribute to a lower growth rate with increasing temperature, an increase in Si loss through etching of  $\text{SiO}_2$  at the pore perimeter and a decreasing sticking probability for the hydride precursor [26,27].

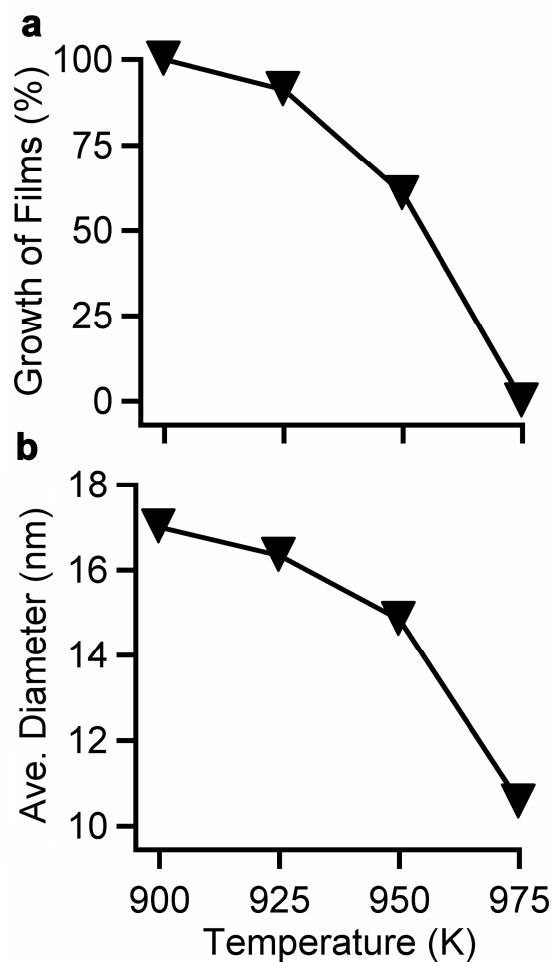


Figure 5.3 a) Fraction of pores that contain Si films versus temperature after 3 min (18,000 L) thermal CVD. Note all pores contained Si in the form of nanoparticles or a continuous film. b) Average particle diameter that considers a film to be a 17 nm particle.

HWCVD can circumvent the decreasing sticking coefficient in that  $\text{SiH}_x$  radicals formed on the heated filament are directed toward the surface and can circumvent the etching reaction by increasing the incident flux of the reactive radicals. HWCVD results on patterned  $\text{Si}_3\text{N}_4$  samples are presented in Figures 5.4-7. Figures 5.4 and 5.6 explore the effect of exposure at a constant flux of 0.3 ML/min and the effect of flux at a constant

exposure of 6 ML, respectively, for growths at 975 K. Figure 5.7 explores the effect of temperature at a constant flux of 0.3 ML/min and exposure of 6 ML.

With exposure the total particle density increases and goes through a maximum that exceeds the total pore density of  $6 \times 10^{10} \text{ cm}^{-2}$  (Figure 5.4a) because some pores contain more than one nanoparticle (Figure 5.4b). Figure 5.5 presents a SEM image of a HWCVD sample for 6 ML total exposure at 975 K. The following characteristics to note are the irregular particle shapes and the position of particles within the pores, which suggest that nucleation occurs randomly within a pore and that coalescence is significant during growth. At the lowest exposures, only  $\sim 30\%$  of the pores have any particles and ultimately all the pores contain at least one particle for 15 ML total exposure (Figure 5.4c). The increasing percentage (Figure 5.4c) would be expected if nucleation occurs at different times (or in this case exposures) as opposed to occurring at the outset in all pores. At all exposure levels, the greatest fraction of filled pores contains one nanoparticle. The curves for multiple particles (Figure 5.4b) increase at the lower exposures because multiple nucleation events are occurring in the pores; the single pore curve, which reflects the balance of the filled pores, must decrease. Ultimately, the multiple particles in a pore begin coalescing into fewer particles, and eventually form one particle.

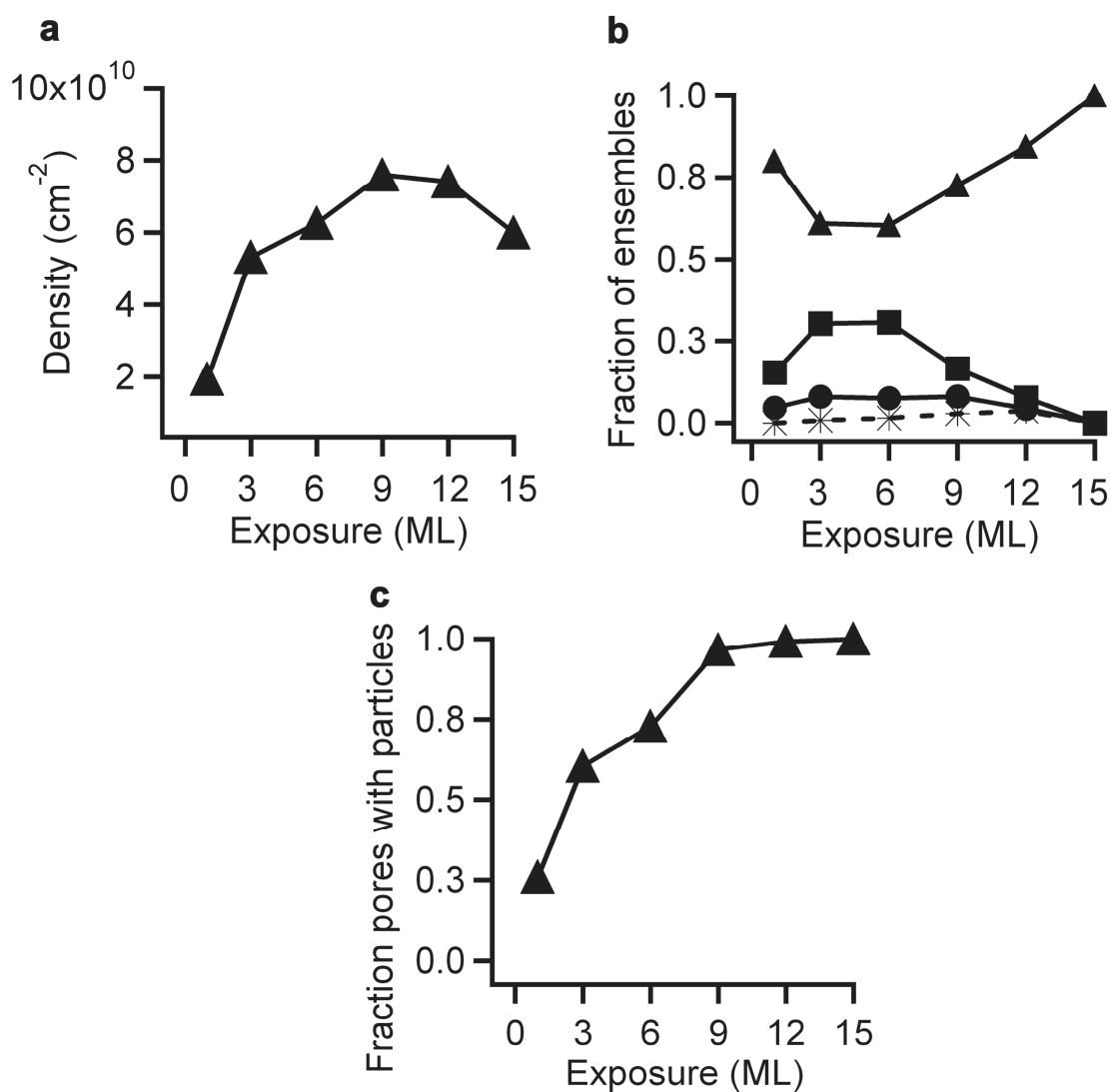


Figure 5.4 Curves showing the effects of changing exposure during HWCVD at 975 K for a flux of 0.3 ML/min; a) Si nanoparticle particle density, b) fraction of filled pores containing ensembles consisting of a single Si particle ( $\blacktriangle$ ), two Si particles ( $\blacksquare$ ), three Si particles ( $\bullet$ ), four Si particles ( $*$ ), and c) fraction of all available pores showing any type of particle ensemble.

Trends in the relative proportions of filled pores with one, two, three and four particle ensembles with exposure indicate that nanoparticles are nucleating at different times (exposures) and then growing to an observable size at yet longer exposures.

Ultimately the multiple particles coalesce into one particle. The 3 and 6 ML HWCVD exposures at 975 K offer insight into the question of simultaneous versus sequential particle nucleation. Pores with two particles each have equisized particles in 77% of the pores for both exposures; a 100% value would be expected for simultaneous nucleation. Pores having three particles each display equisized particles in 74% of the pores for 3 ML exposure and in 42% of the pores for 6 ML exposure.

Incidence flux rate data are clustered into two regions, the low flux region at 0.09–0.4 ML/min and the high flux regions found at greater than 0.4 ML/min (Figure 5.6). In the low flux regime, the fraction of filled pores remains constant at ~ 70% and the average particle diameter decreases as the flux is increased since increasing numbers of pores contain more than one particle. The amount of silicon deposited is constant in the 0.09-0.4 ML/min flux range at  $\sim 0.7 \text{ ng/cm}^{-2}$  assuming particles are lens shaped [28]. At a 0.9 ML/min flux rate, the particles completely cover the  $\text{Si}_3\text{N}_4$  surface in 100 % of the pores and grow onto the adjacent  $\text{SiO}_2$  hard mask. This is caused by adatom accumulation overwhelming the loss processes at the perimeters of the  $\text{Si}_3\text{N}_4$  features at the highest flux.

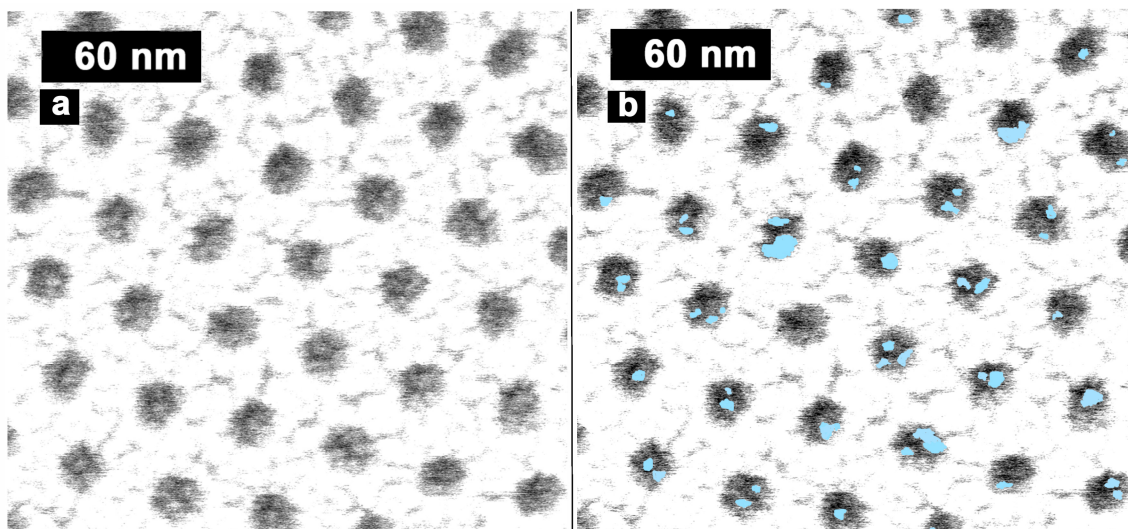


Figure 5.5 a) SEM image of a patterned  $\text{Si}_3\text{N}_4$  HWCVD sample grown at 975 K, 0.4 ML/min flux, and 6 ML total exposure. The dark circles are the bottoms of the  $\text{Si}_3\text{N}_4$  pores and the irregular, faint white objects in the circles are the Si nanoparticles. The continuous bright white surface surrounding the  $\text{Si}_3\text{N}_4$  pores is the  $\text{SiO}_2$  hard mask. b) The image was digitally enhanced with light blue representing the nanoparticles on the dark  $\text{Si}_3\text{N}_4$ .

The fraction of filled pores and the average particle diameter decrease with increasing temperature (Figure 5.7). Essentially films form in every pore at the lowest temperature, 900 K, under the flux (0.3 ML/min) and exposure (6 ML) conditions employed. The particle density goes through a maximum with temperature. The density increase to a value greater than the pore density is related to the appearance of multiple particle ensembles in the pores. The density eventually decays with increasing temperatures because etching reactions are depleting adatoms from the growth region and particles fail to nucleate or grow to an observable size during the exposure time.

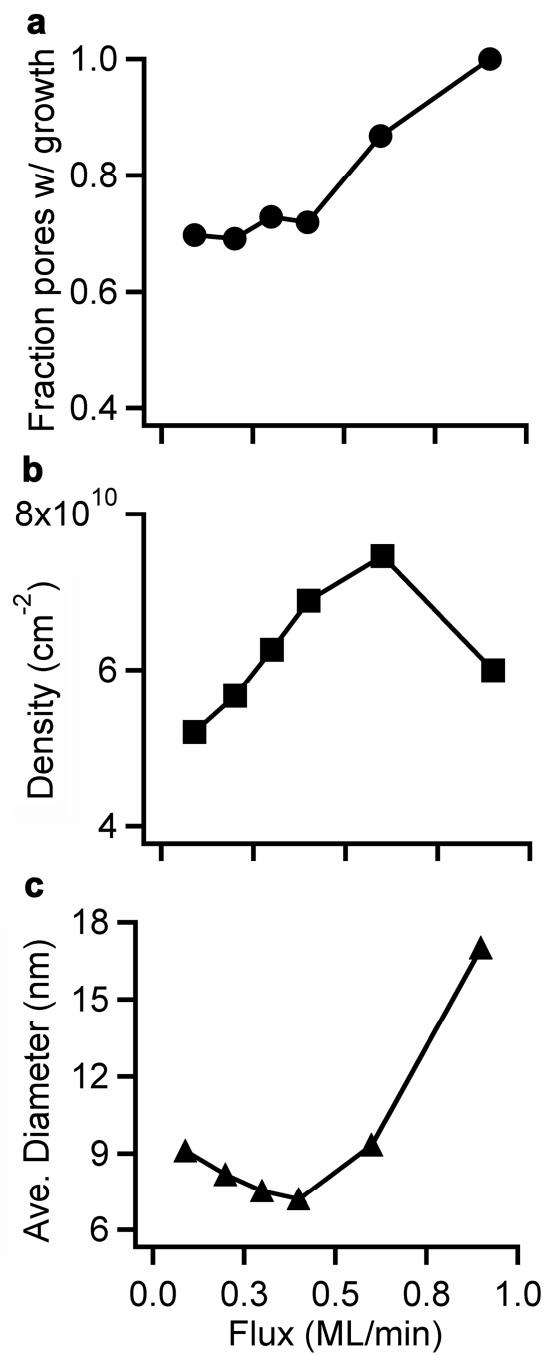


Figure 5.6 Curves showing the effects of changing the flux during HWCVD at 975 K for a constant exposure of 6 ML; a) fraction of all pores showing any particle ensemble combination, b) overall Si nanoparticle density, and c) average nanoparticle diameter.

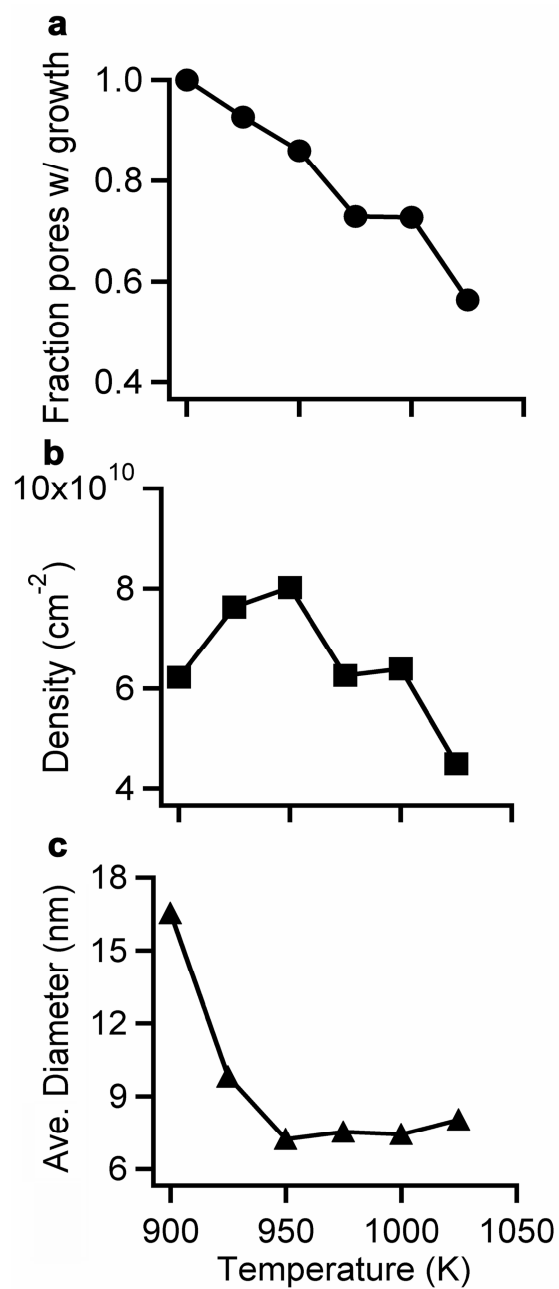


Figure 5.7 Curves showing the effects of changing the temperature during HWCVD at a fixed flux of 0.3 ML/min and total exposure of 6 ML; a) fraction of all pores showing any particle ensemble combination, b) overall Si nanoparticle density, and c) average nanoparticle diameter.

## 5.4 DISCUSSION

Selective growth of Si on arrays of  $\text{Si}_3\text{N}_4$  surfaces defined through a sacrificial  $\text{SiO}_2$  hard mask is qualitatively similar to the selective growth of Ge on  $\text{HfO}_2$  defined through a sacrificial  $\text{SiO}_2$  mask [7]. In both cases the inability of Si or Ge to accumulate on  $\text{SiO}_2$ , yet accumulate on the growth surface, enables selective deposition at the bottom of the features defined through the  $\text{SiO}_2$  mask. The need to work above 900 K to realize facile etching of  $\text{SiO}_2$  by Si leads to very rapid CVD reactions on  $\text{Si}_3\text{N}_4$  and this reduces the flexibility one may have in optimizing the process through changes in temperature and  $\text{Si}_2\text{H}_6$  partial pressure. While both CVD and HWCVD can be used to grow nanoparticles selectively as shown above, HWCVD may be the preferred method. HWCVD permits seeding of the nanoparticles to better control the process [7] and it permits a wide range of radical fluxes to be explored to optimize the process [23].

Selective nanoparticle deposition relies on balancing the generation and accumulation processes for the adatoms on the growth surface against the adatom loss processes. Once formed, a Si adatom can be expected to experience five possible fates in the system under consideration [15,29]: 1) diffusion on the  $\text{SiO}_2$  or  $\text{Si}_3\text{N}_4$  surface until it encounters and attaches to a subcritical cluster (size  $< i^*$ ), which can lead to the adatom reentering the adatom population; 2) diffusion on the  $\text{SiO}_2$  or  $\text{Si}_3\text{N}_4$  surface until it encounters and attaches to a critical cluster (size  $= i^*$ ) or a stable nanoparticle (size  $> i^*+1$ ), which removes the adatom from the adatom population; 3) loss from the  $\text{SiO}_2$  surface through etching reactions that produce  $\text{SiO}$ ; 4) diffusion on the  $\text{Si}_3\text{N}_4$  regions until the adatom encounters and reacts with the  $\text{SiO}_2$  at the pore wall perimeter and is lost through etching reactions; and 5) diffusion on the  $\text{SiO}_2$  regions until it spills over into the pores and becomes adsorbed on the  $\text{Si}_3\text{N}_4$  regions.

These processes are activated and while the absolute rates are not known, some activation energies are available permitting one to consider the relative rates and how rates change with processing conditions. The etching of SiO<sub>2</sub> by Si is well documented [10,30] and was expected to be sufficiently fast at 975 K that adatoms would not accumulate on the SiO<sub>2</sub> in CVD and HWCVD. The absence of Si nanoparticles on the SiO<sub>2</sub> mask seems to bear this out. Etching has an activation energy of either 0.84 [30] or 2.7 eV [10]. The activation energy of Si diffusion on Si<sub>3</sub>N<sub>4</sub> may be similar in magnitude to the activation energy of Si on SiO<sub>2</sub> (0.47 eV) [13], which would mean that the etching reaction will increase faster than diffusion as the temperature increases. Silicon adatoms can diffuse over the relevant surface dimensions (17 nm within a pore and 23 nm between pore openings on the SiO<sub>2</sub> mask) very rapidly. Using the prefactor of 0.1 cm<sup>2</sup>/s and the activation energy of 0.47 eV for Si on SiO<sub>2</sub> [13] to estimate a diffusion coefficient of Si on Si<sub>3</sub>N<sub>4</sub>, a Si adatom will have a mean squared displacement of 314 nm<sup>2</sup> (*i.e.*, the area of a 20 nm pore) in ~2.2 ns. Further, given the rapid diffusion and the short distances over which the Si needs to diffuse on the SiO<sub>2</sub> mask, we cannot discount the possibility that some of the Si adatoms originating on the SiO<sub>2</sub> surface diffuse to and attach to the Si<sub>3</sub>N<sub>4</sub> surfaces. Such a possibility could be tested with molecular beam epitaxy where the incident flux Si atoms is known versus in HWCVD where a mixture of radicals and stable molecules are incident on the surfaces.

In its simplest form, our model for selective growth has incident hydride radicals (on the SiO<sub>2</sub>) leading to adatoms that do not accumulate and etch the SiO<sub>2</sub> surface, and incident hydride radicals (on the Si<sub>3</sub>N<sub>4</sub>) leading to adatoms that are contained on the Si<sub>3</sub>N<sub>4</sub> surfaces at the pore bottoms until they either nucleate and/or add to a nanoparticle, or react with the SiO<sub>2</sub> walls and are removed by etching. Studies on amorphous surfaces have indicated that  $i^*$  is either 0 or 1 for nanoparticle growth [11,13]. Extrapolating these

findings to Si on Si<sub>3</sub>N<sub>4</sub>, particles nucleate when an adatom diffuses on the surface until it is positioned over a site that serves as a nanoparticle anchor ( $i^* = 0$ ) or encounters an adatom that is already at a suitable site ( $i^* = 1$ ). The rate of nucleation has a power-law dependence on the average adatom density of  $i^*+1$  [16]. Nucleation, as manifested in multiple nanoparticles per pore and the total percentage of filled pores, increases with flux at constant temperature (Figures 5.6a and 5.6b), and decreases with increasing temperature at constant flux (Figure 5.7). Nucleation increases when process conditions favor a higher adatom concentration. It is not possible to estimate the steady-state coverage of adatoms on the Si<sub>3</sub>N<sub>4</sub>, within a pore. Given the short distances on the confined Si<sub>3</sub>N<sub>4</sub> surfaces over which a Si adatom diffuses before nanoparticle nucleation and growth, and the low power-law order dependence (1 or 2) for the nucleation rate on the adatom concentration, it seems the selective growth process is dominated by etching and the concentration of adatoms within individual pores must be quite low. Beyond the nucleation step, adatoms are required for particle growth to an observable size. The majority of silicon precursor delivered to the surface is removed through etching with SiO<sub>2</sub> and the low particle growth rate reflects the loss. Using HWCVD requires 15 ML silicon exposure at 975 K at a 0.3 ML/min flux to grow large enough particles within the pores to cover the exposed nitride surface. By comparison to an unpatterned nitride surface at the equivalent flux, a 2 ML exposure results in a continuous film. We conclude that the adatom removal from the nitride surface (at the pore perimeter) under the selective growth conditions is extremely quick and is the limiting factor in nucleation and particle growth.

## 5.5 SUMMARY

We demonstrate the versatility of selective nanoparticle growth within ~17 nm pores by extending it from the Ge on HfO<sub>2</sub> system to the Si on Si<sub>3</sub>N<sub>4</sub> system. Growth is

directly on the  $\text{Si}_3\text{N}_4$  (or  $\text{HfO}_2$ ) dielectric surface, possibly simplifying future incorporation of this method into device fabrication. The silica hard mask regulates nanoparticle nucleation and growth through adatoms etching the silica and evolving as gaseous  $\text{SiO}$ . The silicon deposition rate is dependent upon the balance of the adatom removal mechanism and nanoparticle nucleation and growth reactions. Maintaining a sufficient Si flux to exceed the etching rate is key to nanoparticle growth. Nanoparticle growth decreases with increasing temperature and increases with increasing incident flux of  $\text{SiH}_x$  radicals in HWCVD.

## REFERENCES

- [1] S. Tiwari, F. Rana, H. Hanafi, A. Hartstein, E. F. Crabbe, and K. Chan, Appl. Phys. Lett. 68 (1996) 1377.
- [2] I. Crupi, D. Corso, S. Lombardo, C. Gerardi, G. Ammendola, G. Nicotra, C. Spinella, E. Rimini, and M. Melanotte, Mater. Sci. Eng. C 23 (2003) 33.
- [3] International Technology Roadmap for Semiconductors, 2005.
- [4] S. Miyazaki, Y. Hamamoto, E. Yoshida, M. Ikeda, and M. Hirose, Thin Solid Films 369 (2000) 55.
- [5] F. Mazen, T. Baron, A. M. Papon, R. Truche, and J. M. Hartmann, Appl. Surf. Sci. 214 (2003) 359.
- [6] C. Basa and E. A. Irene, J. Vac. Sci. Technol. A 17 (1999) 817.

- [7] S.S. Coffee, Stanley S.K., and J.G. Ekerdt, J. Vac. Sci. Technol. B 24 (2006) 1913.
- [8] S.K. Stanley, S.V. Joshi, S.K. Banerjee, and J.G. Ekerdt, J. Vac. Sci. Technol. A 24 (2006) 78.
- [9] S. K. Stanley, S. V. Joshi, S. K. Banerjee, and J. G. Ekerdt, Surf. Sci. 600 (2006) L54.
- [10] W. T. Leach, J. H. Zhu, and J. G. Ekerdt, J. Cryst. Growth. 243 (2002) 30.
- [11] Q. M. Li, J.L. Krauss, S. Hersee, and S. M. Han, J. Phys. Chem. C 111 (2006) 779.
- [12] T. Baron, F. Martin, P. Mur, C. Wyon, and M. Dupuy, J. Cryst. Growth 209 (2000) 1004.
- [13] M. S. Mason, J. K. Holt, and H. A. Atwater, Thin Solid Films 458 (2004) 67.
- [14] J. A. Venables, Phys. Rev. B 36 (1987) 4153.
- [15] J. A. Venables, G. D. T. Spiller, and M. Hanbucken, Rep. Prog. Phys. 47 (1984) 399.
- [16] D. Kandel, Phys. Rev. Lett. 78 (1997) 499.
- [17] J. A. Venables, Surf. Sci. 300 (1994) 798.

- [18] Q. M. Li, B. Pattada, S. R. J. Brueck, S. Hersee, and S. M. Han, *J. Appl. Phys.* 98 (2005) 073507.
- [19] K. W. Guarini, C. T. Black, K. R. Milkove, and R. L. Sandstrom, *J. Vac. Sci. Technol. B* 19 (2001) 2784.
- [20] K. W. Guarini, C. T. Black, Y. Zhang, H. Kim, E. M. Sikorski, and I. V. Babich, *J. Vac. Sci. Technol. B* 20 (2002) 2788.
- [21] S. K. Ray, C. K. Maiti, and N. B. Chakraborti, *Semicond. Sci. Technol.* 8 (1993) 599.
- [22] T. Baron, F. Mazen, J. M. Hartmann, P. Mur, R. A. Puglisi, S. Lombardo, G. Ammendola, and C. Gerardi, *Solid-State Electron.* 48 (2004) 1503.
- [23] W. T. Leach, J. H. Zhu, and J. G. Ekerdt, *J. Cryst. Growth* 240 (2002) 415.
- [24] C. Basa, Y. Z. Hu, M. Tinani, and E. A. Irene, *J. Vac. Sci. Technol. A* 16 (1998) 3223.
- [25] F. Mazen, L. Mollard, T. Baron, S. Decossas, and J. M. Hartmann, *Microelectron. Engr.* 73-74 (2004) 632.
- [26] B. A. Ferguson, C. T. Reeves, D. J. Safarik, and C. B. Mullins, *J. Chem. Phys.* 113 (2000) 2470.
- [27] S. M. Gates, *Surf. Sci.* 195 (1988) 307.

- [28] J. H. Zhu, W. T. Leach, S. K. Stanley, J. G. Ekerdt, and X. M. Yan, J. Appl. Phys. 92 (2002) 4695.
- [29] H. Brune, Surf. Sci. Rep. 31 (1998) 121.
- [30] D. C. Streit and F. G. Allen, J. Appl. Phys. 61 (1987) 2894.

## Chapter 6 – Graphoepitaxy Development

### 6.1 INTRODUCTION

The incorporation of diblock copolymers into useful patterning masks requires control over both phase morphology and the phase orientation with respect to the substrate. Removing one phase selectively, typically the minority phase, leaves the continuous majority phase as a soft mask. The cylindrical morphology is practical in patterning nanometer scale features for nanoparticles; the individually isolated features are most easily achieved after pattern transfer. Spherical features require more exact etching techniques and more dedicated etching equipment than are available at the University of Texas. Figure 6.1 presents a cross section diagram and scanning electron microscopy (SEM) image of the template created with the poly(styrene-*b*-methyl methacrylate) [30 % methyl methacrylate, 70 % styrene,  $M_n = 67,000$ ] cylindrical phase thin films [1,2] used in our patterning process. Cylinders are oriented in a perpendicular

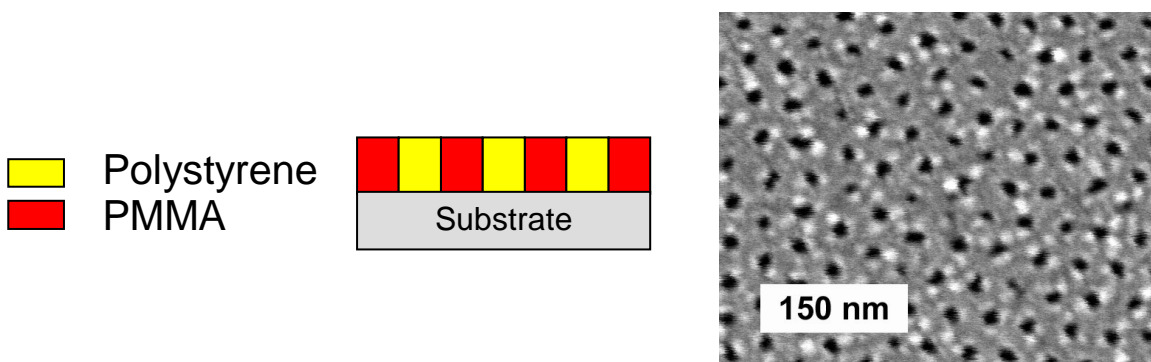


Figure 6.1 Left: cross section diagram of a cylindrical phase thin film on a lateral plane having the cylinders oriented perpendicular with the substrate. Right: SEM image of self-assembled poly(styrene-*b*-methyl methacrylate) diblock copolymer thin film (30 % methyl methacrylate, 70 % styrene,  $M_n = 67,000$ ) after the cylinders were selectively removed using glacial acetic acid. The voids are seen as dark circles.

fashion using a combination of surface energy neutrality [3] and vertical confinement [4,5]. The surface energy neutrality is achieved by chemically attaching a random copolymer (40 % methyl methacrylate, 60 % styrene) monolayer to the substrate surface. Vertical confinement is achieved by controlling the diblock copolymer film thickness during the spin coating step. The film thickness is determined by properties dependent upon the copolymer molecular weight, in our case  $M_n = 67,000$  [6]. The two properties are the 20 nm cylinder diameter and the 40 nm center-to-center distance,  $d$ , between cylinders resulting in a  $6 \times 10^{10} \text{ cm}^{-2}$  cylinder density. The  $d$  value scales with the degree of polymerization,  $N$ , (the number of monomer units) as  $d \propto N^\gamma$ , where  $\gamma$  is the scaling exponent or a measurement of incompatibility between copolymer blocks and  $\gamma$  is equal to 0.58 for our system [4]. For proper vertical confinement in our experiments, which causes the cylinders to self-assemble perpendicular with the substrate, the film thickness must be on the order of  $d$ ; successful self-assembly is realized when the copolymer film is  $37 \pm 4$  nm thick.

The size of the self-assembled minority phase can be controlled by changing the diblock copolymer molecular weight with a minimum feature size limit [7]. The  $N$  value in our system is  $\sim 690$  having a number average molecular weight ( $M_n$ ) of 67,000. Larger 30 nm diameter poly(methyl methacrylate) [PMMA] cylinders are created when  $M_n$  is doubled to 132,000 or  $N \sim 1360$  [4]. Increase the molecular weight more, and even larger cylinders would be formed. It is estimated that this molecular weight polymer has a  $\chi N$  factor of  $\sim 11.0$  [4] when  $M_n = 67,000$ , where  $\chi$  is the Flory-Huggins  $\chi$  parameter. The minimum required  $\chi N$  factor for complete phase separation is 10.5 [8], therefore, the 20 nm diameter cylinders approach the minimum intrinsic feature size limit the poly(styrene-*b*-methyl methacrylate) system can achieve.

After annealing to segregate the spin-cast films into regions of PMMA and polystyrene, the diblock copolymer films are polycrystalline. Figure 6.2 is a SEM image of the polycrystalline order found with the poly(styrene-*b*-methyl methacrylate) cylindrical morphology described in the previous paragraph. Within each polymer crystal, the minority phases also have crystal-like order.

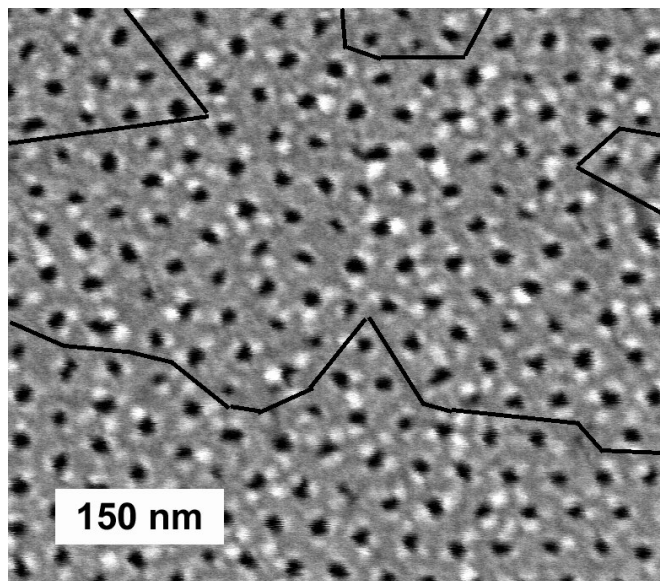


Figure 6.2 SEM image of self-assembled poly(styrene-*b*-methyl methacrylate) diblock copolymer thin film (30 % methyl methacrylate, 70 % styrene,  $M_n = 67,000$ ) after the cylinders were selectively removed using glacial acetic acid and the voids are seen as dark circles. The majority of the surface has hexagonal closed pack void order interrupted by crystal grain boundaries. The solid black lines are drawn to guide the eye to possible grain boundaries between the crystalline domains.

For example, the minority phase in Figure 6.2 forms hexagonal closed packed order. However, the entire polymer film does not retain the crystalline order and is divided into domains (regions) of order.

The lack of long-range order can be overcome by restricting crystalline film portions to macroscopic features such as trenches or mesas of the proper size. Physically

confining the polymer crystal is known as graphoepitaxy [9,10]. Figure 6.3 is a cross section diagram of a cylindrical morphology diblock copolymer thin film being confined by the vertical substrate wall. Graphoepitaxy with the cylindrical phase

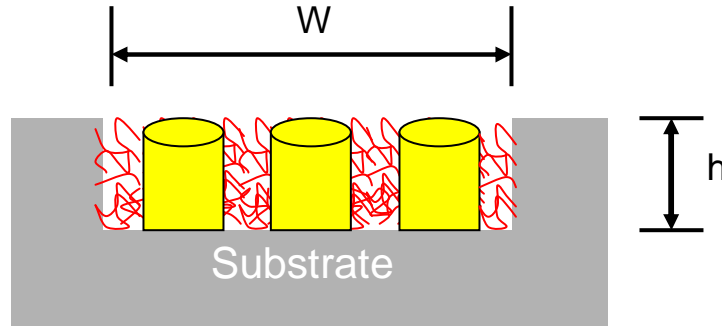


Figure 6.3 Cross section diagram of a patterned trench and cylindrical morphology diblock copolymer thin film being confined by the topography after self-assembly [11]. The yellow represents the minority phase PMMA cylinders and the red lines represent the majority phase polystyrene. The vital dimensions of step height “ $h$ ” and the trench depth and “ $W$ ” are shown.

poly(styrene-*b*-methyl methacrylate) in patterned trenches has been reported [12]. Several factors [13] are vital for proper self-assembly within the trenches: 1) the topography (“ $h$ ” in Figure 6.3) must be at minimum the thickness of the polymer film; 2) long anneals are required to have crystal imperfections diffuse to the film edges; 3) the confinement walls must be extremely close to atomically smooth; and 4) the trench width (“ $W$ ” in Figure 6.3) must be the proper value so the cylinder self-assembly is complete without partial cylinders at the wall edge [12]. The center-to-center cylinder distance ( $d$ ) decreases to 35 nm when confined in trenches compared to the 40 nm  $d$  found on flat lateral surfaces [12]. The 35 nm periodicity is the measurement of one cylinder row width when graphoepitaxy is done in trenches. Thus, if five rows of complete cylinders are desired, the trench width is:  $W = 7 \times 35 \text{ nm} = 245 \text{ nm}$ . Figure 6.4 is an SEM image of

seven PMMA cylinder rows in a  $\sim 250$  nm wide trench after poly(styrene-*b*-methyl methacrylate) graphoepitaxy [12].

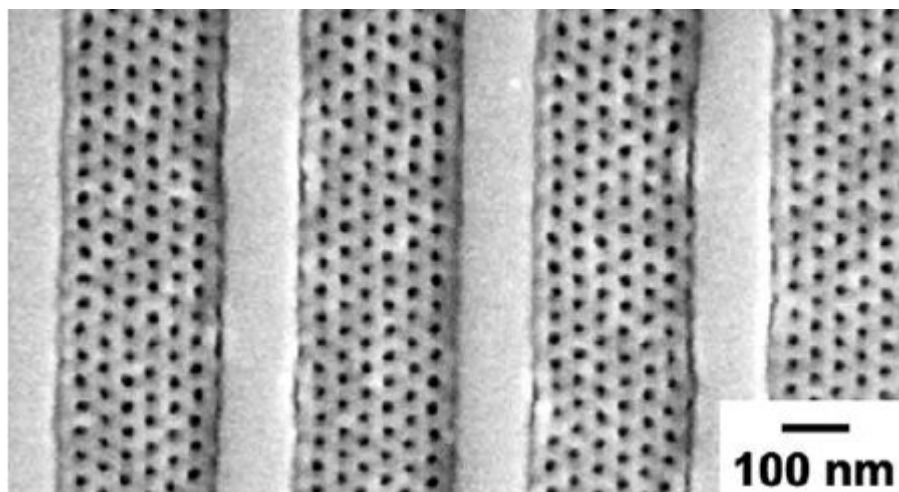


Figure 6.4 SEM image of seven cylinder rows in a  $\sim 250$  nm wide trench after graphoepitaxy using the poly(styrene-*b*-methyl methacrylate) diblock copolymer [12].

## 6.2 – EXPERIMENTAL METHODS

In the initial experiments, Davood Shahjerdi of the Banerjee group provided 54 nm PECVD  $\text{SiO}_2$  on 4-in p-doped Si(100) wafers. After dicing wafers into smaller pieces, the  $1.6 \times 1.6$  cm sized samples began the patterning process with an acetone/ethanol rinse followed with a 5 min sonication in an ethanol bath. After drying with compressed nitrogen, a hexamethyldisilazane adhesion layer was spin coated onto the silica surface and annealed on a hot plate for 3 min at  $90^\circ\text{C}$ . Poly(methyl methacrylate) ( $M_n=960,000$ ) diluted 3% in anisole was then spin coated onto the treated silica surface under conditions that produce a  $\sim 75$  nm thick film. Samples were annealed at  $150^\circ\text{C}$  for 1 h to assure the smoothness of the polymer film and adhesion to the silica.

Individual samples were loaded into a Raith 50 Electron Beam Lithography (EBL) system where the pattern was transferred into the polymer film with an electron beam exposure of  $220 \mu\text{C}/\text{cm}^2$ . The degraded, exposed film was then selectively removed using a 1 min bath in 1:3 methyl isobutyl ketone/isopropyl alcohol developer. Patterned features were lines and squares with 200, 400, 600, 800, and 1000 nm wide dimensions.

The second experimental set again used Davood Shahjerdi sourced 54 nm PECVD  $\text{SiO}_2$  on 4-in p-doped Si(100) wafers. The EBL was performed by Aaron Gin working for the Center for Integrated Nanotechnologies (CINT) at Sandia National Laboratories. The patterned PMMA film had a 200 nm thickness. Features patterned into the PMMA were lines, squares, and parallelograms. The features had the critical widths of 175, 245, 450, and 525 nm to self-assemble 5, 7, 13, and 15 cylinder rows during graphoepitaxy, respectively. Two sets of samples were generated. In the second set, the features were spaced further apart to improve feature filling during spin-coating. Figures 6.5 to 6.9 illustrate the layouts for the CINT-generated features.

## Wafer Layout

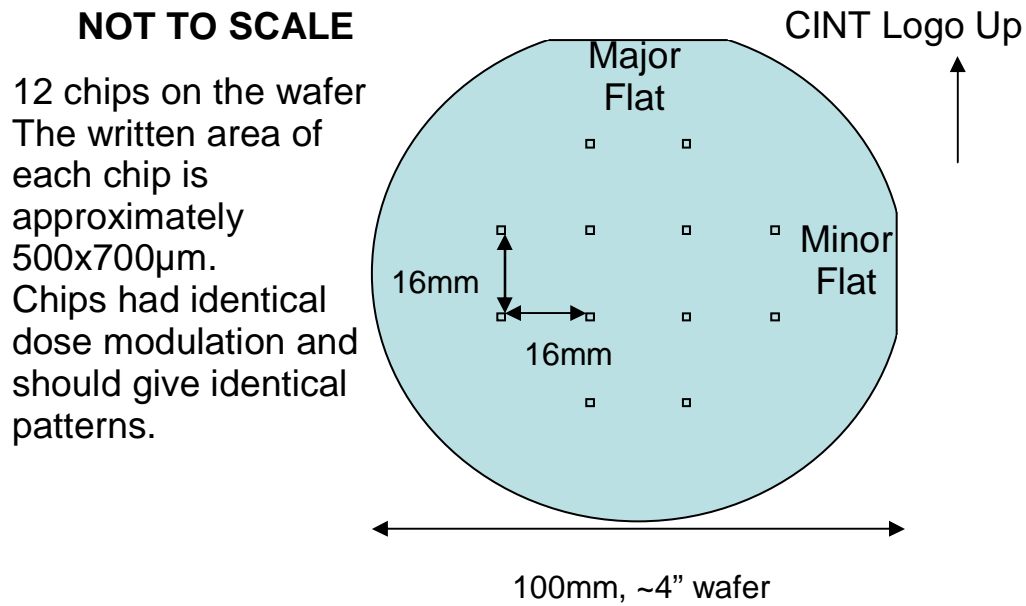


Figure 6.5 Diagram showing the position of EBL patterns on a 4-inch wafer done by Aaron Gin, CINT-SNL. Each square on the wafer represents one full pattern with squares, lines, and parallelograms of all four sizes.

## Individual EBL die

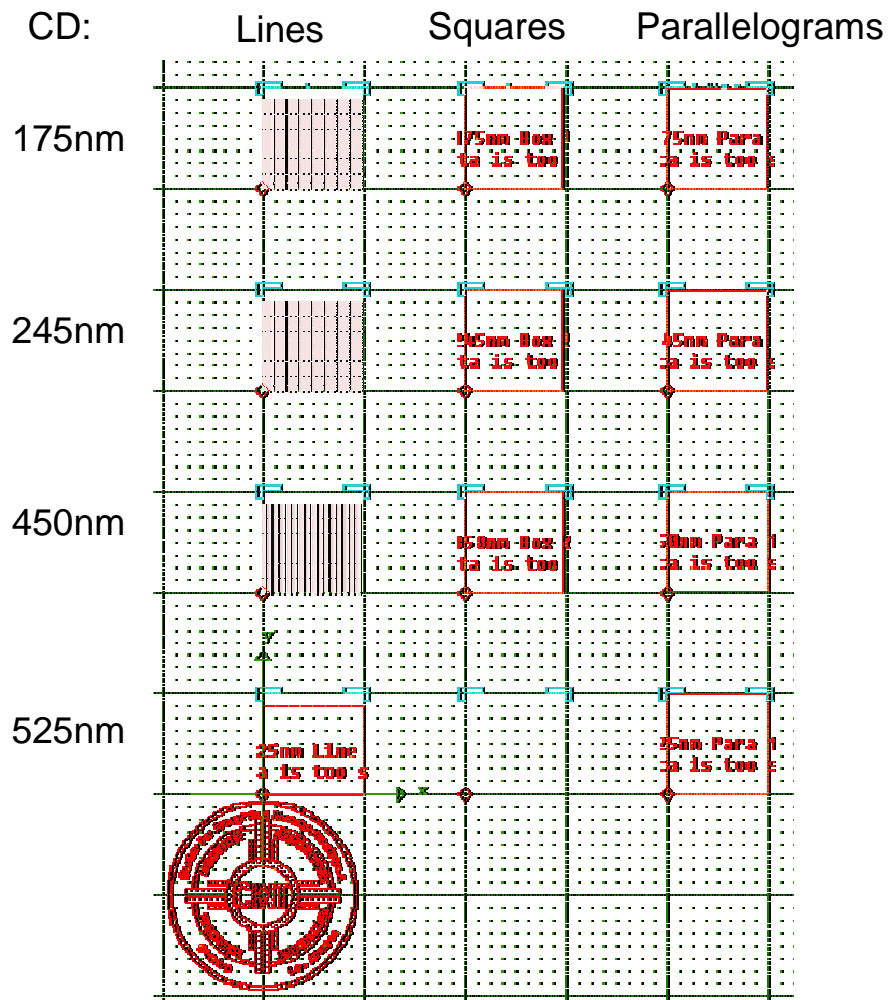
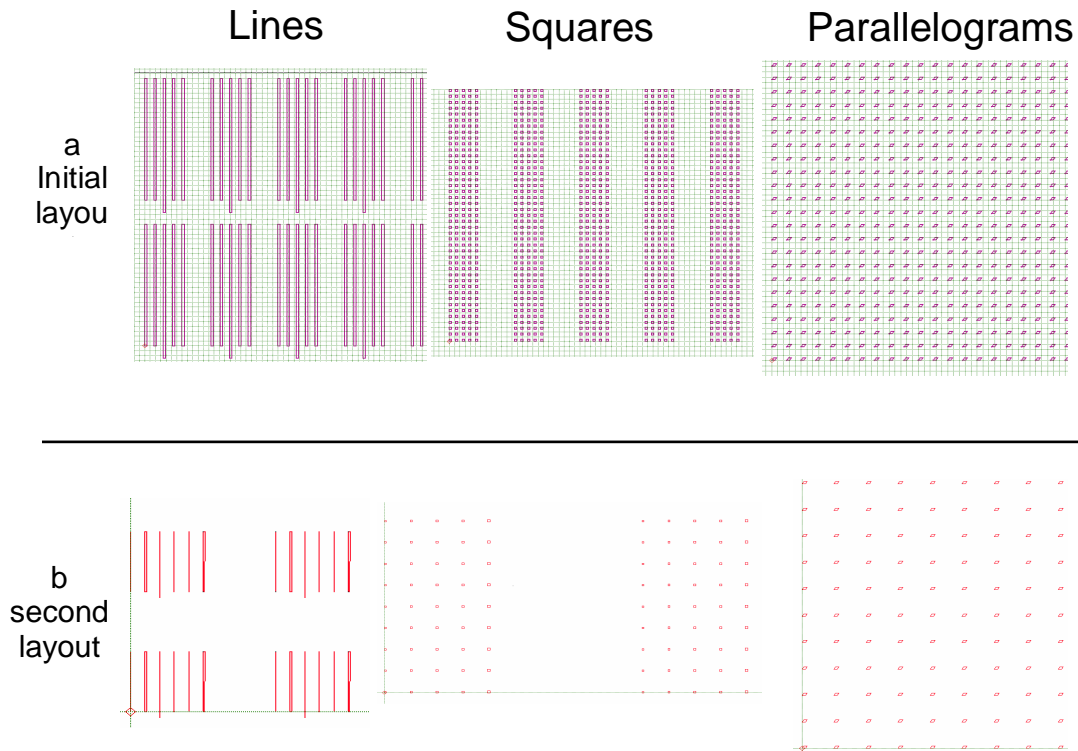


Figure 6.6 Computer aided draft image showing how individual EBL patterns showing how the lines, square, and parallelograms are oriented with respect to each other within one patterning die. (Courtesy Aaron Gin, CINT-SNL)

## Chip Layout Details, 175 nm Feature Size



Center (longer) lines and squares in each column are exactly 175nm in CAD. Lines and squares vary by 10nm in CD as you move to the left (smaller) and right (larger) from center. Minimum spacing between features has increased to **2 microns** for better etch and diblock assembly performance.

Figure 6.7 Computer aided draft image showing how 175 nm features are presented in EBL patterns. The lines, square, and parallelograms are closely oriented with respect to each other. a) The initial pattern. b) The second revised pattern taking in consideration the movement of polymer. (Courtesy Aaron Gin, CINT-SNL)

## Chip Layout details, 175 nm

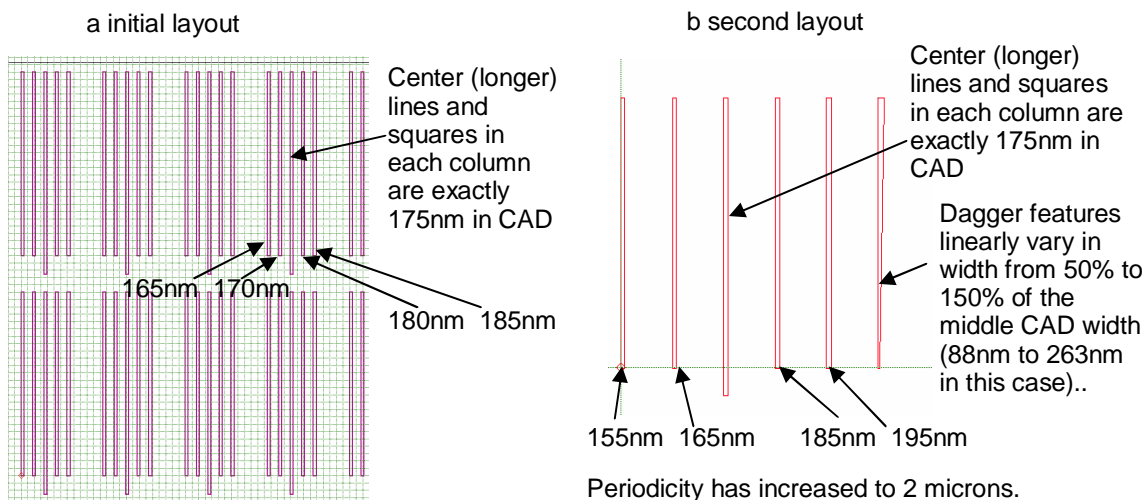


Figure 6.8 Computer aided draft image showing how 175 nm line features are presented in EBL patterns. Lines that are arranged in clusters parallel with each other have various widths. a) The initial pattern. b) The second revised pattern taking in consideration the movement of polymer. (Courtesy Aaron Gin, CINT-SNL)

Reactive ion etch (RIE) using a  $\text{CHF}_3/\text{O}_2$  chemistry at 200 W and 15 or 30 mTorr transferred the pattern into and through the silica layer to the Si wafer giving a trench depth of ~54 nm. Removing the soft polymer mask was performed using a 5 min  $\text{O}_2$  ash at 40 W.

The patterned pieces were cleaned with an acetone/ethanol/deionized (DI) water rinse then dried with compressed nitrogen. The self-assembled diblock copolymer thin film deposition followed published schemes [19,20]. The exposed silica surface was initially pretreated with an  $\alpha$ -hydroxy functionalized random copolymer (60% styrene and 40% methyl methacrylate,  $M_n=8,900$  from Polymer Source Inc.) diluted 1% in toluene by spin coating at 1000 rpm for 30 s. The samples were annealed at 180°C for 48 h allowing the  $-\text{OH}$  terminated end groups to react with the silica surface. Loose polymer strands were removed from the treated surface with a gentle toluene rinse

followed by drying with compressed nitrogen. Poly(styrene-*b*-methyl methacrylate),  $M_n=46,100$  and 21,000 of styrene and methyl methacrylate species, respectively, (Polymer Source Inc.) was diluted 1.0% in toluene and was spin coated onto the treated surface under conditions that produce a  $37 \pm 4$  nm thick film within features that is critical for cylinder self-assembly normal to the substrate. The film thickness measured using flat lateral substrates measured within the range of 30-36 nm to produced proper self-assembly order within different feature sizes from polymer movement across the substrate surface. Further annealing at 180°C for 30 h caused the immiscible polymers to self-assemble and form crystalline sections within the trench features. The minority methyl methacrylate cylinder phase was then selectively removed using a 5 min glacial acetic acid bath and a DI water rinse.

Upon completion of graphoepitaxy, the samples were coated with ~10 nm of Pd/Au to prevent surface charging under analysis in a Hitachi S-4500 field emission scanning electron microscope (SEM).

### **6.3 – RESULTS AND DISCUSSION**

The initial attempt at graphoepitaxy using the Raith 50 EBL system on campus had several processing flaws producing poor self-assembly within the trench features. One serious flaw was the roughness of the trench sidewalls after etching. Figure 6.9 is a SEM image of the poorly ordered diblock copolymer at the edges of two separate trenches. First, the PMMA patterning mask was only 75 nm thick.

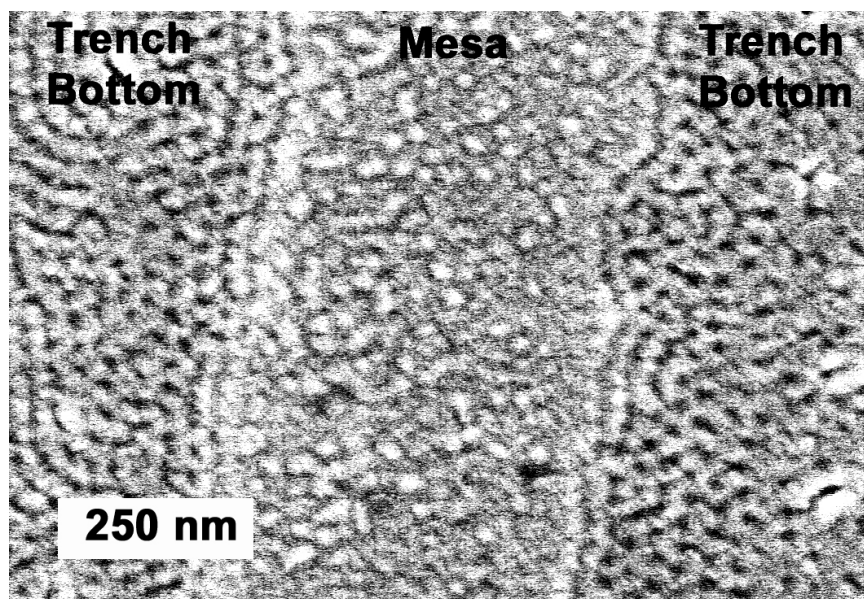


Figure 6.9 SEM image of two ~800 nm wide trenches filled with poly(styrene-*b*-methyl methacrylate). The center of the image is the elevated topography, while the left and right portions filled with dark shapes are two separate trench bottoms. Note: the rough sidewalls and poor diblock copolymer self-assembly.

The low mechanical strength of the thin resist edges enables the film to move easily during the development in the solution, lifting up the polymer film edges. Slight exposure inconsistencies during EBL have significant patterning consequences when such a small volume of polymer is present on a charging insulator surface. The PMMA also has poor plasma resistance, and the edges can be removed during the RIE to transfer the pattern. Errors introduced in the EBL writing step because the films were too thin or the unintended PMMA removal during RIE is transferred into the silica. Second, the  $\text{CHF}_3/\text{O}_2$  RIE chemistry used to make this pattern had a very low gas flow rate at 20 and 1 sccm for  $\text{CHF}_3$  and  $\text{O}_2$ , respectively, and a 15 mTorr total pressure. The combination of low flow rate and low pressure produced poor plasma uniformity within the RIE resulting in etched silica with rough surfaces.

The initial graphoepitaxy problems were overcome by altering the patterning process. These changes were recommended through collaboration with Aaron Gin. First, the PMMA film thickness was increased to 200 nm. Second, the EBL was done by Aaron Gin using CINT facilities. Third, the RIE process flow gases was increased to 36 and 4 sccm for  $\text{CHF}_3$  and  $\text{O}_2$ , respectively, along with increasing the pressure to 30 mTorr resulting in a more uniform plasma. The change in process parameters resulted in smooth silica sidewalls as seen in Figure 6.10.

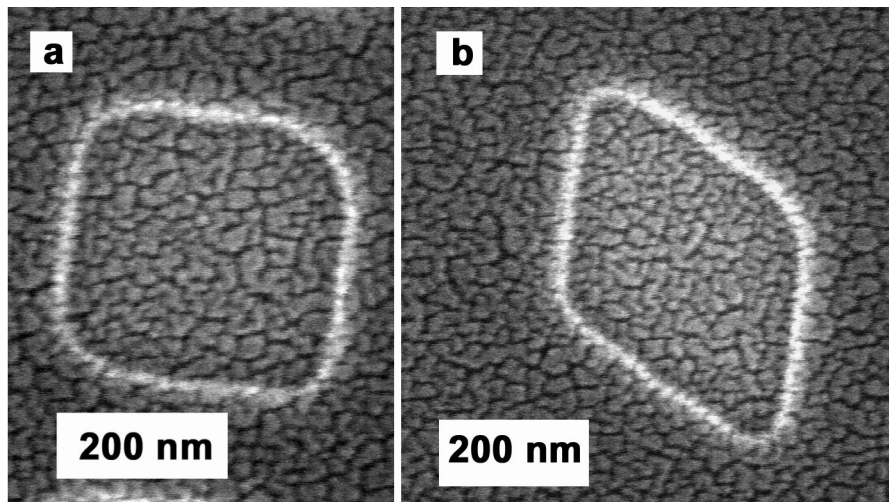


Figure 6.10 SEM features of etched silica features ~60 nm deep using the second, more successful patterning process. a) Etched square ~300 nm in width. b) Etched parallelogram with side lengths of ~300 nm. Note: The pattern used in the EBL was for 245 nm sized features and proximity effects made the final features larger than intended.

One unwanted side effect from the new process is the features were ~50 nm wider than the programmed pattern. Charge proximity effects are a problem at the extremely small dimensions in EBL. The diblock copolymer process was then applied to a silica patterned piece from the same wafer and graphoepitaxy was observed in limited number of features as seen in Figure 6.11.

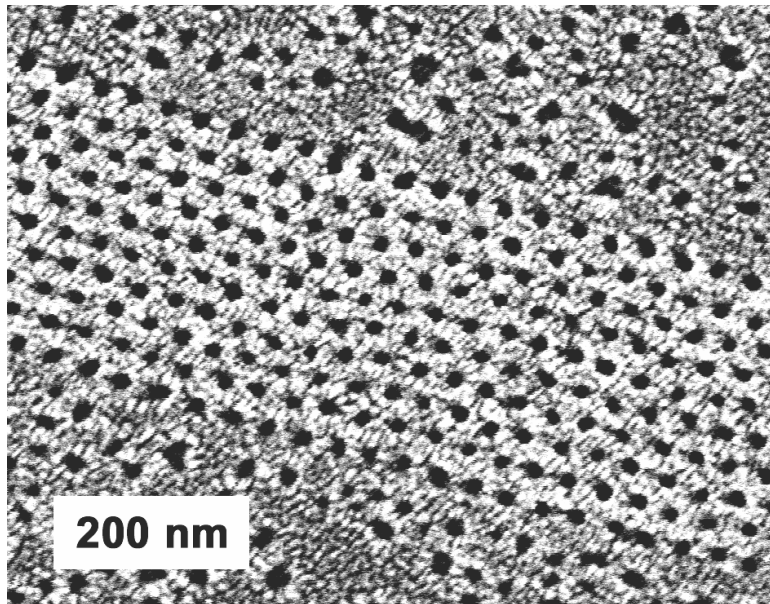


Figure 6.11 Graphoepitaxy of cylindrical poly(styrene-*b*-methyl methacrylate) within a ~350 nm wide line the step height is ~60 nm. Dark circles represent the voids left after the PMMA cylinders were removed. The hexagonal closed pack order is achieved using the smooth sidewalls obtained from the new patterning process.

One factor contributing to good order is the step height between the trench bottom and silica feature top is ~60 nm. The 60 nm sidewall assures that confinement is sufficient within the trench and isolates the polymer at the trench bottom from the surrounding polymer film on the silica mesas. Graphoepitaxy within features is dependent on the film thickness [12]. The capillary forces during annealing can change the film thickness within a trench if the polymer moves to make a more flat, planar shape. Such polymer movement would result in varying thickness across the trench bottoms. For example, polymer films spin coated to a 31 nm thick film on a flat surface only properly self-assembled in 250 nm wide boxes, whereas a 35 nm thick polymer film only properly self-assembled in 350 nm wide boxes.

The uniformity of self-assembly across various features was also poor due to improper filling during spin coating or polymer movement during annealing. Figure 6.12 represents three neighboring lines with different levels of desired diblock copolymer order in their trenches. The perpendicular cylinders appear as black dots and cylinders that are parallel to the substrate appear as black lines. Proper filling is critically important and has been discussed in recent publications [12].

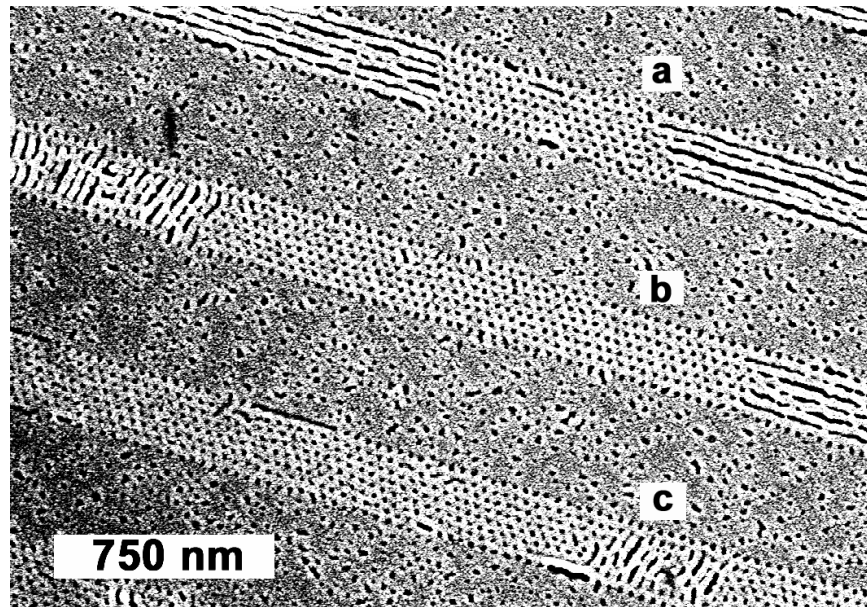


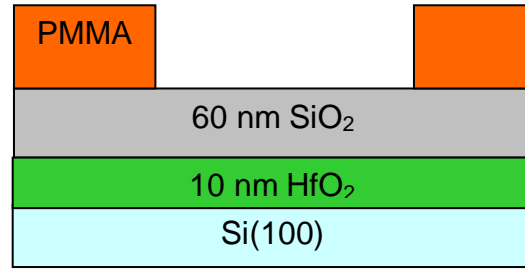
Figure 6.12 SEM image of three 350 nm wide line features having a 60 nm step height. Poly(styrene-*b*-methyl methacrylate) has varying percentage of proper order where cylinders are separated and perpendicular with the substrate within the observed field of view: a) 30 % good order b) 60 % good order c) 75 % good order

The second CINT created EBL pattern was written to reduce pattern density in an attempt to improve feature filling. Experiments to test this solution are on-going.

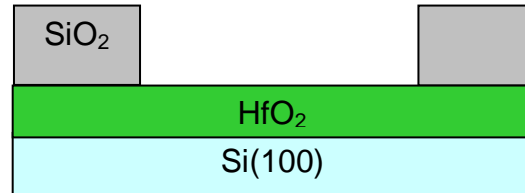
Actual use of diblock copolymer graphoepitaxy to pattern Si or Ge nanoparticles was not realized due to time constraints, but the incorporation of graphoepitaxy into a nanoparticle deposition technique would use a variation of the processes described in

previous chapters. These experiments will be done by a different student. Using the same insulator stack structures as those used in Chapters 3-5 except, but with a thicker SiO<sub>2</sub> hard mask would allow the top-down process incorporating graphoepitaxy into the process. As an example, the experiment would use a 60 nm CVD SiO<sub>2</sub>/10 nm atomic layer deposition HfO<sub>2</sub> grown stack structure on 8-in p-doped Si(100) wafer. First, EBL serves as a soft mask on the thick SiO<sub>2</sub> hard mask and the RIE etches 50 nm deep exposing the HfO<sub>2</sub> underneath. Second, a thin 3-5 nm thick PVD or CVD silica film would be deposited that conforms to surface topography. Third, graphoepitaxy would be performed following the procedure outlined in this Chapter within the patterned silica features. RIE then transfers the diblock copolymer pattern into the remaining 3-5 nm of SiO<sub>2</sub> at trench bottom with a 40 W O<sub>2</sub> ash removing the copolymer afterwards. Finally, Ge nanoparticles would be deposited using room temperature seeding followed by a 25 ML hot wire chemical vapor deposition (HWCVD) exposure at 800 K. Figure 6.13 on the following page is a proposed process diagram for dual-level patterning Ge nanoparticles onto a HfO<sub>2</sub> substrate surface.

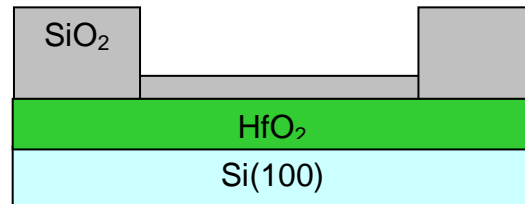
Step 1: Perform EBL on Si/HfO<sub>2</sub>/SiO<sub>2</sub> stack



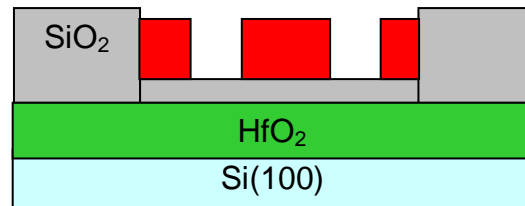
Step 2: RIE SiO<sub>2</sub> until HfO<sub>2</sub> is exposed, remove PMMA mask with O<sub>2</sub> ash



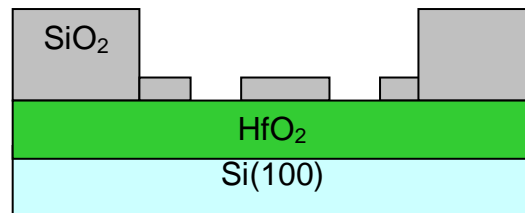
Step 3: Deposit thin 3-5 nm SiO<sub>2</sub> film



Step 4: Graphoepitaxy diblock copolymer



Step 5: RIE SiO<sub>2</sub> until HfO<sub>2</sub> is exposed, remove diblock mask with O<sub>2</sub> ash



Step 6: HWCVD Ge into pores onto exposed HfO<sub>2</sub>

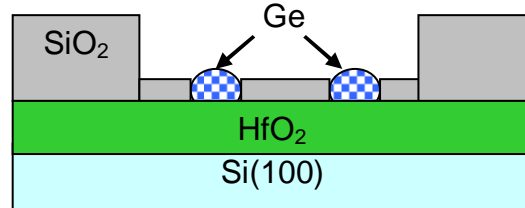


Figure 6.13 Process diagram of the process incorporating graphoepitaxy into the precise nanoparticle placement scheme using the Ge/HfO<sub>2</sub> material system. The scheme would accomplish dual-level patterning of HWCVD nanoparticles.

## REFERENCES

- [1] K. W. Guarini, C. T. Black, Y. Zhang, H. Kim, E. M. Sikorski, and I. V. Babich, *J. Vac. Sci. Tech. B* **20**, 2788 (2002).
- [2] C. T. Black, K. W. Guarini, K. R. Milkove, S. M. Baker, T. P. Russell, and M. T. Tuominen, *Appl. Phys. Lett.* **79**, 409 (2001).
- [3] P. Mansky, Y. Liu, E. Huang, T. P. Russell, and C. Hawker, *Science* **275**, 1458 (1997).
- [4] K. W. Guarini, C. T. Black, and S. H. I. Yeung, *Adv. Mater.* **14**, 1290 (2002).
- [5] P. Mansky, C. K. Harrison, P. M. Chaikin, R. A. Register, and N. Yao, *Appl. Phys. Lett.* **68**, 2586 (1996).
- [6] K. W. Guarini, C. T. Black, K. R. Milkove, and R. L. Sandstrom, *J. Vac. Sci. Tech. B* **19**, 2784 (2001).
- [7] T. Xu, H. C. Kim, J. DeRouchey, C. Seney, C. Levesque, P. Martin, C. M. Stafford, and T. P. Russell, *Polymer* **42**, 9091 (2001).
- [8] I.W. Harnley, *The Physics of Block Copolymers*. (Oxford University Press, Oxford, UK, 1998).
- [9] J. Y. Cheng, C. A. Ross, E. L. Thomas, H. I. Smith, and G. J. Vancso, *Appl. Phys. Lett.* **81**, 3657 (2002).

- [10] R. A. Segalman, A. Hexemer, R. C. Hayward, and E. J. Kramer, *Macromolecules* **36**, 3272 (2003).
- [11] R. A. Segalman, K. E. Schaefer, G. H. Fredrickson, E. J. Kramer, and S. Magonov, *Macromolecules* **36**, 4498 (2003).
- [12] C.T. Black and O. Bezencenet, *IEEE Trans. Nanotech.* **3**, 412 (2004).
- [13] R. Ruiz (Personal Communication, 2006).

## Chapter 7 – Summary and Future Work

This dissertation examines Si and Ge CVD upon the amorphous, dielectric substrates of  $\text{Si}_3\text{N}_4$  and  $\text{HfO}_2$ , respectively. First, deposition kinetics were investigated for the Ge/ $\text{HfO}_2$  material system on unpatterned (extended) surfaces. Second, Ge deposition was performed while restricting the available  $\text{HfO}_2$  surface area to micrometer and nanometer scale regions using a  $\text{SiO}_2$  hard mask and the confinement effects on nanoparticle deposition was investigated. This Ge/ $\text{HfO}_2$  study established the concepts and demonstrated the processes for nanoparticle positioning. Finally, the versatility of the patterning process was demonstrated using the Si/ $\text{Si}_3\text{N}_4$  material system.

Using mean-field nucleation theory, the critical cluster size,  $i^*$ , is estimated as zero for the Ge/ $\text{HfO}_2$  material system. Nucleation occurs when  $i^*+1$  sized clusters are reached, thus, only one adatom is required for formation of a stable nuclei. Nanoparticle density is not a function of adatom concentration adjusted through the incident deposition flux. When deposition time is on the order of hours, the long thermal exposure the  $\text{HfO}_2$  substrate receives reduces the particle density through desorption reactions involving Ge and  $\text{HfO}_2$ . Using temperature as a variable, the critical cluster formation activation energy was estimated as  $0.6 \pm 0.3$  eV and  $0.4 \pm 0.2$  eV for Limits I and II, respectively. Limit I assumes that adatom addition to existing particles is instantaneous while Limit II assumes an energy barrier exists for the addition of adatoms to existing particles.

Confining the  $\text{HfO}_2$  exposed surface area using a  $\text{SiO}_2$  hard mask enabled us to investigate how restricted surface area influences nanoparticle growth within a feature size range of 20 nm to 100  $\mu\text{m}$ . The confinement does not change particle density at deposition fluxes greater than 0.1 ML/min when the features widths are greater than 200

nm as predicted by mean-field nucleation theory since  $i^*=0$ , or density is flux insensitive. Decreasing the flux to 0.1 ML/min, reduces the HfO<sub>2</sub> adatom concentration allowing other surface based reactions such as desorption with the SiO<sub>2</sub> mask to influence confined nanoparticle density. Therefore, the nucleation kinetics are likely unchanged as the HfO<sub>2</sub> is confined by SiO<sub>2</sub>. The results on both the extended and confined surfaces suggest the activation energies for nucleation, surface diffusion, and Ge loss from SiO<sub>2</sub> surfaces are close in value, and the value for Ge loss from SiO<sub>2</sub> has been reported as 0.42 eV.

Using the self-assembling diblock copolymer poly(styrene-*b*-methyl methacrylate) thin films, 20 nm features having a  $6 \times 10^{10} \text{ cm}^{-2}$  density were patterned into a SiO<sub>2</sub> thin film upon a HfO<sub>2</sub> surface. The 20 nm diameter pores restrict the HfO<sub>2</sub> surface to the point of suppressing nucleation where a maximum of 67% of pores grew particles during HWCVD. Nucleation is randomly placed within the pore bottom with respect to the pore SiO<sub>2</sub> walls. The Ge particles grow up to 15 nm in diameter. Unity filling of pores is achieved by room temperature Ge seeding before deposition. The nanoparticle shape and size is controlled by varying the temperature which changes the rate at which Ge is removed from the exposed HfO<sub>2</sub> surface at the pore bottom.

The selective deposition process versatility is demonstrated by extending the 20 nm diameter diblock copolymer pores patterning SiO<sub>2</sub> on a Si<sub>3</sub>N<sub>4</sub> surface. Silicon nanoparticles were then selectively grown on the Si<sub>3</sub>N<sub>4</sub> pore bottoms. High nucleation rates led to multiple particles per pore, up to 4, that are visible in SEM. The particles are irregularly shaped and randomly placed on the nitride surface. Nanoparticle growth is an inverse function of temperature and a linear function of flux. The Si<sub>3</sub>N<sub>4</sub> also has a high reactivity toward Si<sub>2</sub>H<sub>6</sub> leading to thermal CVD grown particles without the aid of the radical flux found in HWCVD that was necessary for Ge deposition on HfO<sub>2</sub> in 20 nm diameter features.

## 7.1 CONTINUED KINETICS STUDY

The kinetics study in Chapter 3 studied the Ge/HfO<sub>2</sub> material system. The  $i^*$  and  $E^*$  values were estimated using mean-field nucleation theory. Two important activation energies used in the mean-field nucleation mathematical framework were not explored. These energies are the adatom diffusion activation energy,  $E_d$ , and the adatom addition barrier,  $E_b$ . The latter activation energy would also determine which energetic Limit is relevant to the system. If  $E_b \rightarrow 0$ , Limit I conditions are applied to the system and if  $E_b$  has a significant value, Limit II applies [1]. Investigation of the unknown activation energies using HWVCD and modeling would be done in a similar manner as Mason *et al.* [2].

Future kinetics studies could also explore other Volmer-Weber mode material systems. Potential material systems using the method outlined in this dissertation could deposit Si or Ge on the Al<sub>2</sub>O<sub>3</sub>, Si<sub>3</sub>N<sub>4</sub>, ZnO<sub>2</sub>, or ZrO insulator surfaces. The Si/Si<sub>3</sub>N<sub>4</sub> system was not used in the kinetic studies for several undesirable physical processes during HWCVD. First, the background exposure to the Si<sub>2</sub>H<sub>6</sub> precursor had significant secondary thermal CVD occurring simultaneously with material obtained from the radical flux. The exact Si exposure Si<sub>3</sub>N<sub>4</sub> surfaces received during HWCVD is unknown. One solution reducing the background exposure problem would be using SiH<sub>4</sub> as an alternative precursor since it has 1/4 the sticking probability of Si<sub>2</sub>H<sub>6</sub> [3]. Second, the HWCVD Si particle density on Si<sub>3</sub>N<sub>4</sub> is on the order of 10<sup>12</sup> cm<sup>-2</sup> with significant coalescence by the stage of particle growth (~5 nm) when particles are observable in SEM and AFM. Using mean-field nucleation theory would be difficult, since particle density requires analysis before significant coalescence occurs during deposition. The appearance of the two deposition issues would be material system dependent.

## 7.2 CONTINUED CONFINED DEPOSITION STUDY

The Ge HWCVD performed on the micrometer scale confined  $\text{HfO}_2$  surfaces did not have particle densities change with flux at higher deposition flux. The insensitive nature of the Ge/ $\text{HfO}_2$  material system is predicted by mean-field nucleation theory from our extended surface studies having a critical cluster size,  $i^*$ , of zero. The next logical experimental step would use micrometer scale confinement on a Volmer-Weber mode material system where the  $i^*$  value is one or greater. Higher  $i^*$  means a greater number of adatoms are required for stable cluster formation. The nucleation rate is therefore more sensitive to adatom concentration at higher  $i^*$  values. The lower adatom concentration from confinement would be amplified as  $i^*$  increases in the form of a greater particle density decrease when compared to an equivalent extended surface deposition. When the decrease in adatom concentration becomes relevant would depend on the feature size specific to the deposition conditions and material system. When  $i^*$  is greater than zero, we believe a transition size (with a relevant drop in adatom concentration) exists when larger features deposit nanoparticles like extended surfaces and smaller features have confinement effects decreasing nanoparticle density.

The diblock copolymer used in this dissertation work patterns 20 nm pores at a pore density of  $6 \times 10^{10} \text{ cm}^{-2}$ . The 15 nm diameter nanoparticles obtained through the selective deposition process are too large for most nanotechnology applications. The nanoparticle density is also less than typically desired in most cases. We attempted to decrease feature size using the same poly(styrene-*b*-methyl methacrylate) cylindrical morphology with a lower molecular weight,  $M_n = 35,500$ . The lower molecular weight copolymer did not completely self-assemble into separate phases. Knowing this we can estimate the  $\chi$  for the poly(styrene-*b*-methyl methacrylate) system since the minimal

requirement for complete separation requires  $\chi N > 10.5$ . The degree of polymerization,  $N$ , is the total number of individual polymer monomer units and is 367 and 690 for the molecular weights of 35,500 and 67,100, respectively. The greater molecular weight polymer self-assembles while the lower weight does not, therefore, the  $\chi N$  equaling 10.5 would occur between these two  $N$  values allowing us to approximate  $\chi$  at  $\sim 0.02$  during the 160 °C self-assembly anneal as reported [4].

Several other diblock copolymer self-assembly methods besides our system have been demonstrated that pattern smaller features at a higher density. One method uses spherical morphology instead of the cylindrical morphology utilized in this dissertation. The spherical morphology is obtained by changing the relative ratio of poly(styrene) to poly(methyl methacrylate) from 70% to 30% found in the cylindrical morphology to 80% to 20% creating spheres, while keeping the molecular weight similar at  $M_n = 78,000$ . Figure 7.1 is a SEM of a polystyrene template left after a monolayer of poly(methyl methacrylate) spheres were selectively removed using glacial acetic acid leaving  $\sim 13$  nm pores at a  $1.2 \times 10^{11} \text{ cm}^{-2}$  density. The image was obtained from a partially completed monolayer leaving the sphere exposed on top of the polystyrene template. When a fully formed monolayer was deposited, the  $\text{O}_2$  RIE removing the spheres lacked nanometer scale uniformity and etch rate control needed to avoid damaging the polystyrene template used as a soft mask. Development of a proper  $\text{O}_2$  etch is the factor preventing the use of the higher density poly(styrene-*b*-methyl methacrylate) spherical morphology in our current research. Another diblock copolymer based alternative is utilizing another diblock copolymer system such as poly(styrene-*b*-butadiene) having a higher Flory-Huggins interaction parameter,  $\chi$ , or poorer solubility between polymer species capable of self-assembling into minority phases down to 10 nm in size [5].

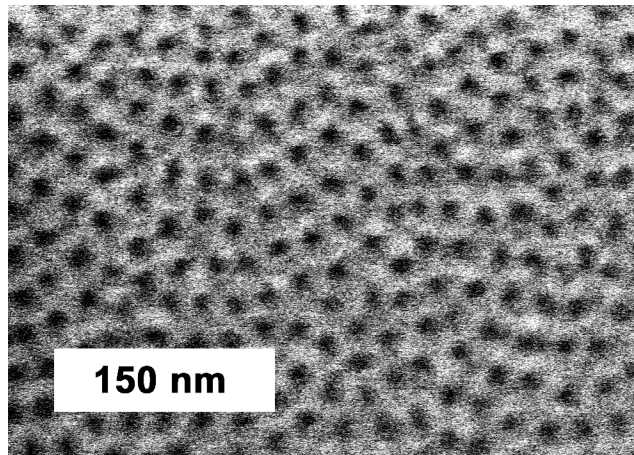


Figure 7.1 SEM image of thin film polystyrene template obtained from poly(styrene-*b*-methyl methacrylate) [80% styrene, 20% methyl methacrylate,  $M_n = 78,000$ ] deposited on  $\text{SiO}_2$  surface. The monolayer was partially formed allowing access to the minority spherical methyl methacrylate with acetic acid removing the spheres selectively. The dark spots are pores having  $\sim 13$  nm diameters and a  $1.2 \times 10^{11} \text{ cm}^{-2}$  density.

The nanoparticles deposited within the 20 nm pores were all characterized in SEM with the  $\text{SiO}_2$  hard mask still present. Using nanoparticles in working devices would require the removal of the patterning hard mask accessing the particles. The HF acid bath is one method to selectively etch  $\text{SiO}_2$  without etching either Ge or Si. For wet chemistry hard mask removal in the Ge/HfO<sub>2</sub> material system, HF is also selective to  $\text{SiO}_2$  over HfO<sub>2</sub> by a ratio of 13 to 1. The problem with using an HF bath with the Ge/HfO<sub>2</sub> material system is the interfacial GeO<sub>x</sub> created between the HfO<sub>2</sub> and Ge particle is etched by the HF. The Ge nanoparticles are then lifted off the HfO<sub>2</sub> surface during the wet etch. For the  $\text{SiO}_2$  patterned Si/Si<sub>3</sub>N<sub>4</sub> system, HF does not etch the Si particles, but it does etch the Si<sub>3</sub>N<sub>4</sub> surface at approximately 1/2 the rate of  $\text{SiO}_2$  leading to fabrication inconsistency. Removing the  $\text{SiO}_2$  hard mask for either material system requires developing a dry etch since most wet etches designated for  $\text{SiO}_2$  are HF based

[6]. Using a dry etch to remove the  $\text{SiO}_2$  may require an intermediate particle coating material protecting nanoparticles from stray reactive ions.

### **7.3 GRAPHOEPI TAXY**

The graphoeptaxy development within this dissertation uses the thin film cylindrical phase poly(styrene-*b*-methyl methacrylate) technology described in Chapter 2. Even though good order was achieved in square and parallelogram features with widths up to  $\sim 0.5 \mu\text{m}$ , the desired order was not achieved in all the patterned features across the sample. The main cause of inconsistent ordering in sunken  $\text{SiO}_2$  features is polymer diffusion from adjacent areas surrounding the feature [7]. The polymer is uncontrollably filling in the feature preventing the thickness dependent film from self-assembling with the desired order. Nonsymmetrical features such as lines, often have portions of the feature having the desired order with cylinders perpendicular to the substrate while other sections of the line have poor order because the film is too thin or thick locally. Placing features too close laterally often leads to features competing for the same polymer on the elevated  $\text{SiO}_2$  between the features, which results in poor order in both features. Spherical morphology thin films are more forgiving concerning film thickness and desired self-assembly, but similar problems arise if the copolymer is spin coated directly onto an uneven surface topography [8]. Development of a diblock copolymer system achieving consistent desired order, regardless of surface topography, is a necessity for future applications using graphoeptaxy obtained from films directly deposited upon samples.

## REFERENCES

- [1] D. Kandel, Phys. Rev. Lett. **78**, 499 (1997).
- [2] M. S. Mason, J. K. Holt, and H. A. Atwater, Thin Solid Films **458**, 67 (2004).
- [3] Y. Z. Hu, D. J. Diehl, C. Y. Zhao, C. L. Wang, Q. Liu, E. A. Irene, K. N. Christensen, D. Venable, and D. M. Maher, J. Vac. Sci. Tech. B **14**, 744 (1996).
- [4] K. W. Guarini, C. T. Black, and S. H. I. Yeung, Adv. Mater. **14**, 1290 (2002).
- [5] M. Park, C. Harrison, P. M. Chaikin, R. A. Register, and D. H. Adamson, Science **276**, 1401 (1997).
- [6] P. Walker and W.H. Tarn, *CRC Handbook of Metal Etchants*. (CRC Press, Boca Raton, FL, 1991).
- [7] C.T. Black and O. Bezencenet, IEEE Trans. Nanotech. **3**, 412 (2004).
- [8] R. A. Segalman, K. E. Schaefer, G. H. Fredrickson, E. J. Kramer, and S. Magonov, Macromolecules **36**, 4498 (2003).

## Appendix

### ACADEMIC HISTORY/PEDIGREE

William Henry McAdams (MS **1917** MIT, honorary Sc.D. **1945** University of Kentucky)

*Professor Chemical Engineering and Chair of Faculty MIT*

Thomas Kilgore Sherwood (Sc.D. **1929** MIT under W. H. McAdams)

*Chemical Engineering MIT*

Edwin Richard Gilliland (Sc.D. **1933** MIT under T. K. Sherwood)

*Professor of Chemical Engineering at MIT*

Raymond Frederick Baddour (Sc.D. **1951** MIT under E. R. Gilliland)

*Professor Emeritus at MIT*

Alexis T. Bell (Sc.D. **1967** MIT under R.F. Baddour)

*Professor of Chemical Engineering at UC Berkeley*

John Gilbert Ekerdt (Ph.D. **1979** UC Berkeley under A.T. Bell)

*Professor of Chemical Engineering at UT Austin*

Shawn Stephen Coffee (PhD **2007** UT Austin under J.G. Ekerdt)

## BIBLIOGRAPHY

- [1] A. P. Alivisatos, *Science* **271**, 933 (1996).
- [2] H. I. Hanafi, S. Tiwari, and I. Khan, *IEEE Trans. Electron Dev.* **43**, 1553 (1996).
- [3] S. Tiwari, F. Rana, H. Hanafi, A. Hartstein, E. F. Crabbe, and K. Chan, *Appl. Phys. Lett.* **68**, 1377 (1996).
- [4] P. M. Solomon, *Annual Rev. Mater. Sci.* **30**, 681 (2000).
- [5] International Technology Roadmap for Semiconductors; <http://www.itrs.net/>, 2005.
- [6] Y. Q. Wang, J. H. Chen, W. J. Yoo, Y. C. Yeo, S. J. Kim, R. Gupta, Z. Y. L. Tan, D. L. Kwong, A. Y. Du, and N. Balasubramanian, *Appl. Phys. Lett.* **84**, 5407 (2004).
- [7] H. G. Yang, Y. Shi, L. Pu, R. Zhang, B. Shen, P. Han, S. L. Gu, and Y. D. Zheng, *Appl. Surf. Sci.* **224**, 394 (2004).
- [8] M. Vulpio, C. Gerardi, S. Lombardo, G. Ammendola, I. Crupi, T. Rossetti, N. Nastasi, G. Mantarro, and G. Nicotra, in *Gettering and Defect Engineering in Semiconductor Technology* (2002), Vol. 82-84, pp. 663.
- [9] S. Tiwari, J. A. Wahl, H. Silva, F. Rana, and J. J. Welser, *Appl. Phys. A-Mater. Sci. Processing* **71**, 403 (2000).
- [10] I. Crupi, D. Corso, S. Lombardo, C. Gerardi, G. Ammendola, G. Nicotra, C. Spinella, E. Rimini, and M. Melanotte, *Mater. Sci. Eng. C* **23**, 33 (2003).
- [11] B.G. Streetman and S.K. Banerjee, in *Solid State Electronic Devices* (Prentice Hall, Upper Saddle River, NJ, 2000).
- [12] S. Tiwari, F. Rana, K. Chan, L. Shi, and H. Hanafi, *Appl. Phys. Lett.* **69**, 1232 (1996).
- [13] L. Perniola, B. D. Salvo, G. Ghibaudo, A. F. Para, G. Pananakakis, T. Baron, and S. Lombardo, *Solid-State Electron.* **47**, 1637 (2003).
- [14] D. W. Kim, T. Kim, and S. K. Banerjee, *IEEE Trans. Electron Dev.* **50**, 1823 (2003).

- [15] G. Ammendola, M. Vulpio, M. Bileci, N. Nastasi, C. Gerardi, G. Renna, I. Crupi, G. Nicotra, and S. Lombardo, *J. Vac. Sci. Tech. B* **20**, 2075 (2002).
- [16] S. Lombardo, B. De Salvo, C. Gerardi, and T. Baron, *Microelec. Eng.* **72**, 388 (2004).
- [17] T. H. Ng, V. Ho, L. W. Teo, M. S. Tay, B. H. Koh, W. K. Chim, W. K. Choi, A. Y. Du, and C. H. Tung, *Thin Solid Films* **462-63**, 46 (2004).
- [18] Y. Z. Hu, D. J. Diehl, C. Y. Zhao, C. L. Wang, Q. Liu, E. A. Irene, K. N. Christensen, D. Venable, and D. M. Maher, *J. Vac. Sci. Tech. B* **14**, 744 (1996).
- [19] B. Gong, S. Jo, G. Hess, P. Parkinson, and J. G. Ekerdt, *J. Vac. Sci. Tech. A* **16**, 1473 (1998).
- [20] J.N. Israelachvili, *Intermolecular and Surface Forces*. (Academic Press, San Diego, CA, 1992).
- [21] P. Van Der Voort E.F. Vansant, K.C. Vrancken, *Characterization and Chemical Modification of the Silica Surface*. (Elsevier, Amsterdam, 1995).
- [22] T. Baron, F. Mazen, C. Busseret, A. Souifi, P. Mur, F. Fournel, M. N. Semeria, H. Moriceau, B. Aspard, and P. Gentile, *Microelectron. Eng.* **61-2**, 511 (2002).
- [23] C. Basa, Y. Z. Hu, M. Tinani, and E. A. Irene, *J. Vac. Sci. Technol. A-Vac. Surf. Films* **16**, 3223 (1998).
- [24] F. Mazen, L. Mollard, T. Baron, S. Decossas, and J. M. Hartmann, *Microelec. Eng.* **73-74**, 632 (2004).
- [25] S. Miyazaki, Y. Hamamoto, E. Yoshida, M. Ikeda, and M. Hirose, *Thin Solid Films* **369**, 55 (2000).
- [26] L. Andersohn, T. Berke, U. Kohler, and B. Voigtlander, *J. Vac. Sci. Technol. A-Vac. Surf. Films* **14**, 312 (1996).
- [27] D. Kandel, *Phys. Rev. Lett.* **78**, 499 (1997).
- [28] J.A. Venables, *Phil. Mag.* **17**, 697 (1973).
- [29] H. Brune, *Surf. Sci. Rep.* **31**, 121 (1998).
- [30] J. A. Venables, *Surf. Sci.* **300**, 798 (1994).
- [31] J. A. Venables, G. D. T. Spiller, and M. Hanbucken, *Rep. Prog. Phys.* **47**, 399 (1984).

- [32] H. Rauscher, J. Braun, and R. J. Behm, Phys. Rev. Lett. **96**, 116101 (2006).
- [33] Q. M. Li, J.L. Krauss, S. Hersee, and S. M. Han, J. Phys. Chem. C **111**, 779 (2006).
- [34] J. H. Zhu, W. T. Leach, S. K. Stanley, J. G. Ekerdt, and X. M. Yan, J. Appl. Phys. **92**, 4695 (2002).
- [35] W. T. Leach, J. H. Zhu, and J. G. Ekerdt, J. Cryst. Growth **243**, 30 (2002).
- [36] S.K. Stanley, S.V. Joshi, S.K. Banerjee, and J.G. Ekerdt, J. Vac. Sci. Tech. A **24**, 78 (2006).
- [37] H. Matsumura, Jpn. J. Appl. Phys. pt. 1 **37**, 3175 (1998).
- [38] M. S. Mason, J. K. Holt, and H. A. Atwater, Thin Solid Films **458**, 67 (2004).
- [39] W. T. Leach, J. H. Zhu, and J. G. Ekerdt, J. Cryst. Growth **240**, 415 (2002).
- [40] D. C. Streit and F. G. Allen, J. Appl. Phys. **61**, 2894 (1987).
- [41] S.K. Stanley, S.S. Coffee, and J.G. Ekerdt, App. Surf. Sci. **252**, 878 (2005).
- [42] Y. Lin, A. Boker, J. B. He, K. Sill, H. Q. Xiang, C. Abetz, X. F. Li, J. Wang, T. Emrick, S. Long, Q. Wang, A. Balazs, and T. P. Russell, Nature **434**, 55 (2005).
- [43] J. Peng, Y. Xuan, H. F. Wang, Y. M. Yang, B. Y. Li, and Y. C. Han, J. Chem. Phys. **120**, 11163 (2004).
- [44] G. Kastle, H. G. Boyen, F. Weigl, G. Lengl, T. Herzog, P. Ziemann, S. Riethmuller, O. Mayer, C. Hartmann, J. P. Spatz, M. Moller, M. Ozawa, F. Banhart, M. G. Garnier, and P. Oelhafen, Adv. Funct. Mater. **13**, 853 (2003).
- [45] P. Mansky, C. K. Harrison, P. M. Chaikin, R. A. Register, and N. Yao, Appl. Phys. Lett. **68**, 2586 (1996).
- [46] C. Harrison, M. Park, P. M. Chaikin, R. A. Register, and D. H. Adamson, J. Vac. Sci. Tech. B **16**, 544 (1998).
- [47] C. L. Zhang, T. Xu, D. Butterfield, M. J. Misner, D. Y. Ryu, T. Emrick, and T. P. Russell, Nano Letters **5**, 357 (2005).
- [48] I.W. Harnley, *The Physics of Block Copolymers*. (Oxford University Press, Oxford, UK, 1998).

- [49] F.M.A Barton, *CRC handbook of Polymer-Liquid Interaction Parameters and Solubility Parameters*. (CRC Press, Boca Raton, FL, 1990).
- [50] M. Park, C. Harrison, P. M. Chaikin, R. A. Register, and D. H. Adamson, *Science* **276**, 1401 (1997).
- [51] K. Asakawa and T. Hiraoka, *Jpn. J. Appl. Phys.* pt 1 **41**, 6112 (2002).
- [52] K. W. Guarini, C. T. Black, Y. Zhang, H. Kim, E. M. Sikorski, and I. V. Babich, *J. Vac. Sci. Tech. B* **20**, 2788 (2002).
- [53] C. T. Black, K. W. Guarini, K. R. Milkove, S. M. Baker, T. P. Russell, and M. T. Tuominen, *Appl. Phys. Lett.* **79**, 409 (2001).
- [54] P. Mansky, Y. Liu, E. Huang, T. P. Russell, and C. Hawker, *Science* **275**, 1458 (1997).
- [55] K. W. Guarini, C. T. Black, and S. H. I. Yeuing, *Adv. Mater.* **14**, 1290 (2002).
- [56] J. Y. Cheng, C. A. Ross, E. L. Thomas, H. I. Smith, and G. J. Vancso, *Appl. Phys. Lett.* **81**, 3657 (2002).
- [57] R. A. Segalman, A. Hexemer, R. C. Hayward, and E. J. Kramer, *Macromolecules* **36**, 3272 (2003).
- [58] R. A. Segalman, K. E. Schaefer, G. H. Fredrickson, E. J. Kramer, and S. Magonov, *Macromolecules* **36**, 4498 (2003).
- [59] C.T. Black and O. Bezencenet, *IEEE Trans. Nanotech.* **3**, 412 (2004).
- [60] M. Shibata, Y. Nitta, K. Fujita, and M. Ichikawa, **61**, 7499 (2000).
- [61] M. Shibata, Y. Nitta, K. Fujita, and M. Ichikawa, *Appl. Phys. Lett.* **73**, 2179 (1998).
- [62] Y. Nitta, M. Shibata, K. Fujita, and M. Ichikawa, *Surf. Sci.* **496**, L7 (2002).
- [63] Y. Nitta, M. Shibata, K. Fujita, and M. Ichikawa, *Surf. Sci.* **462**, L587 (2000).
- [64] J. R. Heath, R. S. Williams, J. J. Shiang, S. J. Wind, J. Chu, C. Demic, W. Chen, C. L. Stanis, and J. J. Bucchignano, **100**, 3144 (1996).
- [65] J. D. Weil, X. Deng, and M. Krishnamurthy, *J. Appl. Phys.* **83**, 212 (1998).
- [66] D. Cha, M. Ogawa, C. Chen, S. Kim, J. Lee, K. L. Wang, J. Y. Wang, and T. P. Russell, *J. Cryst. Growth* **301**, 833 (2007).

- [67] P. Mansky, T. P. Russell, C. J. Hawker, M. Pitsikalis, and J. Mays, *Macromolecules* **30**, 6810 (1997).
- [68] M. Kanoun, A. Souifi, T. Baron, and F. Mazen, *Appl. Phys. Lett.* **84**, 5079 (2004).
- [69] S. Y. Wang, W. L. Liu, Q. Wan, J. Y. Dai, P. F. Lee, L. Suhua, Q. W. Shen, M. Zhang, Z. T. Song, and C. L. Lin, *Appl. Phys. Lett.* **86**, 113105 (2005).
- [70] J.D. Plummer, M.D. Deal, and P.B. Griffin, *Silicon VLSI Technology: Fundamentals, Practice, and Modeling*, 1 ed. (Prentice Hall, Upper Saddle River, NJ, 2000).
- [71] N. Sugiyama, T. Tezuka, and A. Kurobe, *J. Cryst. Growth* **192**, 395 (1998).
- [72] J. Chen, W. J. Yoo, Z. Tan, Y. Wang, and D. S. H. Chan, *J. Vac. Sci. Tech. A* **22**, 1552 (2004).
- [73] T. Baron, A. Fernandes, J. F. Damlencourt, B. De Salvo, F. Martin, F. Mazen, and S. Haukka, *Appl. Phys. Lett.* **82**, 4151 (2003).
- [74] T. I. Kamins and R. S. Williams, *Appl. Phys. Lett.* **71**, 1201 (1997).
- [75] A. Olzierski, A. G. Nassiopoulou, I. Raptis, and T. Stoica, *Nanotechnology* **15**, 1695 (2004).
- [76] T. Stoica, L. Vescan, and E. Sutter, *J. Appl. Phys.* **95**, 7707 (2004).
- [77] T. Kitajima, B. Liu, and S. R. Leone, *Appl. Phys. Lett.* **80**, 497 (2002).
- [78] K. Shiralagi, R. Zhang, and R. Tsui, *J. Cryst. Growth* **202**, 1209 (1999).
- [79] J. Bloem, *J. Cryst. Growth* **50**, 581 (1980).
- [80] C. Basa, M. Tinani, and E. A. Irene, *J. Vac. Sci. Tech. A* **16**, 2466 (1998).
- [81] T. Baron, B. Pelissier, L. Perniola, F. Mazen, J. M. Hartmann, and G. Rolland, *Appl. Phys. Lett.* **83**, 1444 (2003).
- [82] V. L. Dalal, *Curr. Opin. Solid State Mat. Sci.* **6**, 455 (2002).
- [83] R. Gupta, W. J. Yoo, Y. Q. Wang, Z. Tan, G. Samudra, S. Lee, D. S. H. Chan, K. P. Loh, L. K. Bera, N. Balasubramanian, and D. L. Kwong, *Appl. Phys. Lett.* **84**, 4331 (2004).
- [84] D. W. Kim, S. B. Hwang, T. F. Edgar, and S. Banerjee, *J. Electrochem. Soc.* **150**, G240 (2003).

- [85] Y.Q. Wang, J.H. Chen, W. J. Yoo, and Y. C. Yeo, Mater. Res. Soc. Symp. Proc. **830**, D6.3.1 (2005).
- [86] C. Park, J. Yoon, and E.L. Thomas, Polymer **44**, 6725 (2003).
- [87] R. A. Segalman, Mater. Sci. Eng. R Rep. **48**, 191 (2005).
- [88] S. Lastella, Y. J. Jung, H. C. Yang, R. Vajtai, P. M. Ajayan, C. Y. Ryu, D. A. Rider, and I. Manners, J. Mater. Chem. **14**, 1791 (2004).
- [89] C. Hinderling, Y. Keles, T. Stockli, H. E. Knapp, T. de los Arcos, P. Oelhafen, I. Korczagin, M. A. Hempenius, G. J. Vancso, R. L. Pugin, and H. Heinzelmann, Adv. Mater. **16**, 876 (2004).
- [90] X. M. Yang, S. G. Xiao, C. Liu, K. Pelhos, and K. Minor, J. Vac. Sci. Tech. B **22**, 3331 (2004).
- [91] K. W. Guarini, C. T. Black, K. R. Milkove, and R. L. Sandstrom, J. Vac. Sci. Technol. B **19**, 2784 (2001).
- [92] J. Chen, W. J. Yoo, Z. Tan, Y. Wang, and D. S. H. Chan, J. Vac. Sci. Tech. A **22**, 1552 (2004).
- [93] S.K. Stanley and J.G. Ekerdt, Mater. Res. Soc. Symp. Proc. **879E**, Z3.23 (2005).
- [94] various authors, in *"Standard Thermodynamic Properties of Chemical Substances" in CRC Handbook of Chemistry and Physics, Internet Version* (CRC Press, Boca Raton, FL, 2005), Vol. 85.
- [95] A. A. Shklyayev and M. Ichikawa, Surf. Sci. **514**, 19 (2002).
- [96] C. L. Wang, S. Unnikrishnan, B. Y. Kim, D. L. Kwong, and A. F. Tasch, J. Electrochem. Soc. **143**, 2387 (1996).
- [97] I. Crupi, D. Corso, S. Lombardo, C. Gerardi, G. Ammendola, G. Nicotra, C. Spinella, E. Rimini, and M. Melanotte, Mater. Sci. Eng. C **23** (2003) 33.
- [98] F. Mazen, T. Baron, A. M. Papon, R. Truche, and J. M. Hartmann, Appl. Surf. Sci. **214** (2003) 359.
- [99] C. Basa and E. A. Irene, J. Vac. Sci. Technol. A **17** (1999) 817.
- [100] S.S. Coffee, Stanley S.K., and J.G. Ekerdt, J. Vac. Sci. Technol. B **24** (2006) 1913.

- [101] S. K. Stanley, S. V. Joshi, S. K. Banerjee, and J. G. Ekerdt, *Surf. Sci.* 600 (2006) L54.
- [102] T. Baron, F. Martin, P. Mur, C. Wyon, and M. Dupuy, *J. Cryst. Growth* 209 (2000) 1004.
- [103] J. A. Venables, *Phys. Rev. B* 36 (1987) 4153.
- [104] Q. M. Li, B. Pattada, S. R. J. Brueck, S. Hersee, and S. M. Han, *J. Appl. Phys.* 98 (2005) 073507.
- [105] S. K. Ray, C. K. Maiti, and N. B. Chakraborti, *Semicond. Sci. Technol.* 8 (1993) 599.
- [106] T. Baron, F. Mazen, J. M. Hartmann, P. Mur, R. A. Puglisi, S. Lombardo, G. Ammendola, and C. Gerardi, *Solid-State Electron.* 48 (2004) 1503.
- [107] B. A. Ferguson, C. T. Reeves, D. J. Safarik, and C. B. Mullins, *J. Chem. Phys.* 113 (2000) 2470.
- [108] S. M. Gates, *Surf. Sci.* 195 (1988) 307.
- [109] T. Xu, H. C. Kim, J. DeRouchey, C. Seney, C. Levesque, P. Martin, C. M. Stafford, and T. P. Russell, *Polymer* **42**, 9091 (2001).
- [110] R. Ruiz (Personal Communication, 2006).
- [111] P. Walker and W.H. Tarn, *CRC Handbook of Metal Etchants*. (CRC Press, Boca Raton, FL, 1991).

## VITA

Shawn Stephen Coffee was the first (and only) child born on March 1, 1978 in rural, western Oregon near the city of Eugene to Paul and Ann Coffee. During childhood he moved, in chronological order, to the states of Colorado, Arizona, Washington, and Oregon where he finished high school at Reynolds High School in the Portland suburb of Troutdale, OR. Two scholarships helped Shawn attend college at New Mexico Institute of Mining and Technology (New Mexico Tech.) in Socorro, New Mexico where he earned a Bachelors of Science in Chemical Engineering with high honors in spring 2001. During the undergraduate years, Shawn served as an undergraduate chemistry and physics tutor and also worked in the New Mexico Tech Chemical Engineering department's undergraduate senior laboratory maintaining process control equipment for instruction purposes. In the summer of 2000, Shawn worked in Jeffrey C. Brinker's laboratory at the University of New Mexico in Albuquerque under a grant from the National Science Foundation Research Experience for Undergraduate program developing sol gel thin films. Upon finishing his Bachelors, Shawn worked for one year as a Process Engineer at Sandia National Laboratories in Albuquerque, New Mexico fabricating radio frequency microelectromechanical systems (MEMS). In fall 2002, Shawn entered into the University of Texas at Austin Chemical Engineering department graduate program. During his time in the graduate program, Shawn served as a teacher assistant twice and mentored both a high school and an undergraduate research assistant. He also earned a Masters of Science degree during his time in the graduate program. As

a legacy to the engineering college, Shawn helped develop a revolutionary Nanolab using technology from his graduate studies for instructing senior level undergraduates.

Permanent Address: PO Box 82712

Austin, TX 78708

This dissertation was typed by the author.